Physik Department

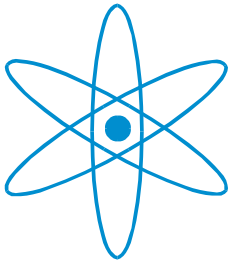

Exclusive analysis of the $\Lambda(1405)$ resonance in the charged $\Sigma\pi$ decay channels in proton proton reactions with HADES

Diplomarbeit
von

Johannes Stephan Siebenson

April 25, 2010

Technische Universität München
Excellence Cluster - 'Origin of the Universe'

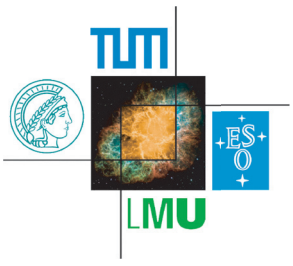

Zusammenfassung

Das HADES Experiment befindet sich an der Gesellschaft für Schwerionenforschung (GSI). Es wurde ursprünglich für die Messung der seltenen Zerfälle der Vektormesonen ρ, ω und ϕ in e^+e^--Paare bei Strahlenergien von 1-2 AGeV entwickelt. Zu diesem Zweck wurden bereits verschiedenen Experimente z.B. mit $C + C$, $Ar + KCl$ und $p + Nb$ Stoßsystemen erfolgreich durchgeführt, anhand derer die vermuteten Mediumeffekte bezüglich Modifikation von Masse und Breite der Vektormesonen untersucht werden können [Aga07]. Als eine Referenzmessung für das $p+Nb$ Stoßsystem (gemessen im September 2008) wurde im April 2007 eine $p + p$ Strahlzeit mit einer Strahlenergie von 3.5 GeV durchgeführt.
Neben der e^+e^--Paar Identifizierung ist es möglich mit HADES Hadronen zu detektieren [Sch08]. Die Daten der $p+p$ Strahlzeit, mit $1{,}2 \cdot 10^9$ detektierten Ereignissen, können somit zum Beispiel für die exklusive Analyse von Teilchen mit Strangeness Inhalt verwendet werden.
Diese Arbeit konzentriert sich hauptsächlich auf die Untersuchung des $\Lambda(1405)$ in seinem Zerfall in die $(\Sigma^{\pm}\pi^{\mp})$ Zustände. Das $\Lambda(1405)$ ist derzeit von hohem Interesse, da angenommen wird, dass es nicht nur ein Drei-Quark Baryon ist sondern vielmehr ein molekularer Zustand aus einem Meson und einem Baryon. Da der gebundene $\bar{K}N$ Zustand einen gewissen Anteil an dieser Resonanz haben sollte, ist die Untersuchung des $\Lambda(1405)$ in Bezug auf das tiefere Verständnis der Kaon-Nukleon Wechselwirkung interessant.
Um die Massenauflösung von Teilchen zu verbessern, die über die Invariante- oder Missing-Mass Technik rekonstruiert werden, wurde für die eklusive Analyse des $\Lambda(1405)$ ein kinematischer Refit entwickelt. In dieser Arbeit werden die mathematischen Details des kinematischen Refits sowie seine Auswirkungen beschrieben. Neben den Verbesserungen für die $\Lambda(1405)$ Analyse kann der Refit auch wichtig für die Untersuchung anderer Reaktionen, wie die Produktion von η und ω Mesonen, sein.
Ein entscheidender Schritt in der vorgestellten Analyse ist die genaue Beschreibung und das genaue Verständnis des Untergrunds im $\Lambda(1405)$ Signal. Speziell für diesen Zweck wurde eine ausgeklügelte Sideband Analyse entwickelt, die den Untergrund aufgrund von Fehlidentifizierung sehr gut beschreiben kann. Schließlich konnten alle Untergrundbeiträge identifiziert und abgezogen werden, wodurch ein reines $\Lambda(1405)$ mit ungefähr 330 Einträgen in jedem Zerfallskanal extrahiert wurde. Diese Arbeit zeigt somit die erste Messung des in $p + p$ Reaktionen produzierten $\Lambda(1405)$, welches über die geladenen Zerfallskanäle rekonstruiert wurde.
Des Weiteren wird die Analyse des $\Sigma(1385)^+$ vorgestellt. Untersuchungen dieser Resonanz können einen Anhaltspunkt bezüglich des Wirkungsquerschnitts des $\Sigma(1385)^0$, das eine wichtige Rolle für die $\Lambda(1405)$ Analyse spielt, geben. Die Polmasse und die Breite des erhaltenen $\Sigma(1385)^+$ Signals wurden bestimmt und mit den nominellen Werten aus der Literatur verglichen.

Abstract

The HADES experiment is located at the heavy ion research facility GSI. It was originally designed for the measurement of the rare decays of the vector mesons ρ, ω and ϕ into e^+e^--pairs at a beam energy of 1-2 AGeV. For this purpose different experiments with e.g. $C + C$, $Ar + KCl$ and $p + Nb$ colliding systems are already accomplished, where the predicted in-medium modifications of the mass and width of the vector mesons can be investigated [Aga07]. As a reference measurement for the $p + Nb$ reaction system (taken in September 2008) a $p + p$ beam time with a beam energy of 3.5 GeV was processed in April 2007.
Besides the feasibility of e^+e^--pair identification, it was shown that it is also possible to detect hadrons with HADES [Sch08]. Thus the data of the $p+p$ run, with $1.2 \cdot 10^9$ detected events, can for instance be used for the analysis of particles with strangeness content.
This thesis concentrates mainly on the investigation of the $\Lambda(1405)$ by its decay into the $(\Sigma^{\pm}\pi^{\mp})$ states. The $\Lambda(1405)$ is currently of high interest, since it is predicted to be not only a three-quark baryon but a molecular state of a meson and a baryon. As the $\bar{K}N$ bound state should have a certain contribution to this resonance, the investigation of the $\Lambda(1405)$ is interesting in terms of a deeper understanding of the kaon-nucleon interaction.
In order to improve the mass resolution of particles, reconstructed via invariant- or missing-mass technique, a kinematic refit was developed for the exclusive analysis of the $\Lambda(1405)$. The mathematical details about the kinematic refit and the effects of its application are described in this thesis. Besides the improvement of the $\Lambda(1405)$ analysis, the refit can also be important for the investigation for other reactions, like the production of η and ω mesons.
An essential step in the presented analysis is the exact modeling and understanding of the background below the $\Lambda(1405)$ signal. Especially for that purpose a sophisticated sideband analysis was developed, which can describe the background due to misidentification quite well. Finally all background contributions could be identified and subtracted and thus a pure $\Lambda(1405)$ was extracted with a total yield of about 330 entries in each decay channel. In this way the thesis presents the first measurement of the $\Lambda(1405)$, produced in $p + p$ reactions and reconstructed in the two charged decay channels.
Furthermore the analysis of the $\Sigma(1385)^+$ is shown. The investigation of this resonance can give a bench mark for the cross section of the $\Sigma(1385)^0$, which plays an important role in the $\Lambda(1405)$ analysis. The pole mass and width of the obtained $\Sigma(1385)^+$ signal were extracted and compared to the nominal values from literature.

Contents

1 Motivation

The $\Lambda(1405)$ is conventionally assumed to be a $I = 0$, strangeness $= -1$ and $J^P = \frac{1}{2}^-$ state, with a nominal mass of 1406.5 MeV/c^2 and a width of 50 MeV/c^2. It was seen for the first time in the ALSTON 61B experiment in 1961, where the reaction $K^- p \to \Sigma\pi\pi\pi$ at 1.15 GeV was investigated [Als61]. As the resonance lies roughly 30 MeV/c^2 below the $\bar{K}N$ threshold, it can only be observed directly in $(\Sigma\pi)^0$ decay channels. A further consequence of this is that chiral perturbation models are not sufficient to describe the structure of the $\Lambda(1405)$ theoretically. First calculations were carried out by Dalitz [Dal61], where the $K^- p$ scattering and reaction amplitude was investigated. Taking into account these scattering data [Ebe59] is necessary, since the $\Lambda(1405)$ emerges from the $\bar{K}N$ and $\Sigma\pi$ interaction. Experimental progress was done in the 60's and 70's, where the spectral shape of the $\Lambda(1405)$ was measured in $\pi^- p$ [Tho73] and $K^- p$ [Hem85] reactions. The obtained statistics were already sufficient to compare the measurements with theoretical calculations, as it is exemplified in figure 1.1 [Hyo08].

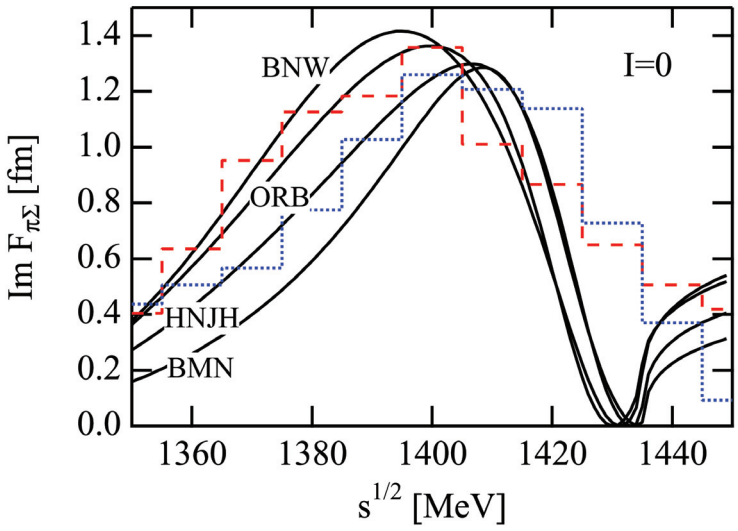

Figure 1.1: The red dashed histogram indicates data from [Tho73], where the invariant mass $(\pi^- \Sigma^+)$ was investigated. The blue dotted histogram indicates the data from [Hem85], where the summed spectra of the $\Sigma^+\pi^-$ and the $\Sigma^-\pi^+$ channels is shown. The solid black lines show different theoretical calculations for the imaginary part of the $\pi\Sigma$ $(I = 0)$ amplitude.

However the quality of the spectrum leaves room for diverse interpretations. As no new data were available in the subsequent years, no theoretical efforts were carried out until the end of the 90's.

The advent of γ induced reactions [Ahn03] triggered a renewed interest from the theory for the $\Lambda(1405)$. New calculations have been provided, where the $\Lambda(1405)$ is described in the context of the unitary extension of chiral perturbation theory [Ose98][Oll01] and chiral coupled channel theory [Lut05]. In the coupled-channel chiral unitary approach, some

resonances are generated dynamically from the interaction of the octet of pseudoscalar mesons with the octet of the $\frac{1}{2}^+$ baryons. By taking into account the underlying SU(3) Lagrangians, the combination of the two octets should result in the dynamical generation of one singlet ($I = 0$) and two octet ($I = 0$, $I = 1$) resonances. However the dynamics of this problem make the two octets degenerate in the case of exact SU(3) symmetry. The implementation of chiral symmetry breaking, giving the physical masses to the mesons and baryons, leads to the breaking of this degeneracy and two distinct octet poles appear. The procedure is illustrated in figure 1.2, where the position of the poles is shown in the complex plane. The trajectories of the poles are given as a function of a parameter x, which gradually breaks the SU(3) symmetry until the physical masses ($x = 1$) are reached.

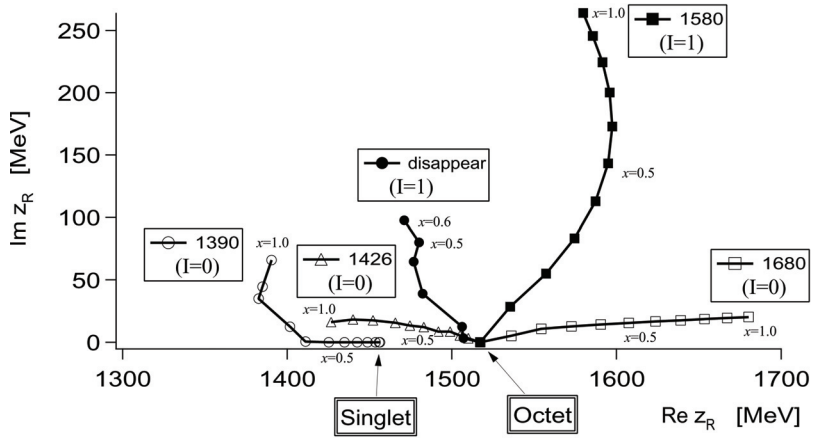

Figure 1.2: The poles in the scattering amplitudes change by changing the SU(3) breaking parameter x. The points illustrate a step size of $\delta x = 0.1$. The $\Lambda(1405)$ is a superposition of the singlet state and the $I = 0$ octet state with the lowest mass [Jid03].

As one can see in the case of $x = 1$, the singlet and one of the $I = 0$ octet poles appear quite close to each other and to the nominal mass of the $\Lambda(1405)$. It was shown in [Jid03] that the experimental observed $\Lambda(1405)$ is thus not just one resonance, but always a superposition of these two poles. The pole at lower masses has a large width and a stronger coupling to the $\Sigma\pi$ states, whereas the pole at higher masses is reduced in width and provides a dominant coupling to the $\bar{K}N$ states. In this approach one can thus imagine the $\Lambda(1405)$ as an interference of a K^-p bound state with a $\Sigma\pi$ resonance, out of which it finally decays into a $(\Sigma\pi)^0$ state. The observed spectral shape and the pole mass depends on the experiment, since the weights by which the two resonances are excited are different in different initial reactions. Furthermore it was predicted that the investigation of the different $(\Sigma\pi)^0$ decay channels could supply different line shapes of the $\Lambda(1405)$. The contribution of the $I = 1$ amplitude to the $\Lambda(1405)$ is not negligible and should influence the production cross section in the different $(\Sigma\pi)^0$ decay channels. The production of the $\Lambda(1405)$ in γ-induced reactions was studied by [Nac99]. The $(\Sigma\pi)^0$ states can be composed

in the following way:

$$\left|\Sigma^-\pi^+\right\rangle = -\frac{1}{\sqrt{6}}\left|2,0\right\rangle - \frac{1}{\sqrt{2}}\left|1,0\right\rangle - \frac{1}{\sqrt{3}}\left|0,0\right\rangle$$
$$\left|\Sigma^+\pi^-\right\rangle = -\frac{1}{\sqrt{6}}\left|2,0\right\rangle + \frac{1}{\sqrt{2}}\left|1,0\right\rangle - \frac{1}{\sqrt{3}}\left|0,0\right\rangle$$
$$\left|\Sigma^0\pi^0\right\rangle = -\sqrt{\frac{2}{3}}\left|2,0\right\rangle - \frac{1}{\sqrt{3}}\left|0,0\right\rangle$$

The $I = 2$ state can be neglected, but the different signs of the $I = 1$ state in the two charged channels leads through interference with the dominant $I = 0$ state to different cross sections and thus to different line shapes for these channels (see figure 1.3, panel (a)). Similar results were obtained in [Lut05].
In order to quantify the contribution of the $I = 1$ state, the line shapes corresponding to the three different decay channels must be investigated. Recently the CLAS collaboration presented high statistic results for the reaction $\gamma p \to \Lambda(1405)K^+$ [Mor10]. For an incident energy of the γ of 1.77 GeV $< E_\gamma <$ 1.99 GeV, the invariant mass $(\Sigma^+\pi^-)$,$(\Sigma^-\pi^+)$ and $(\Sigma^0\pi^0)$ was reconstructed. The obtained spectra are shown in figure 1.3 (panel (b)). Indeed the line shapes as well as the pole masses of the $\Lambda(1405)$ are different for the three different decay channels, like it is expected by theory. However a comparison to the theoretical calculations in [Nac99] (see panel (a)) provides some inconsistencies. The experiment shows a shift of the $\Sigma^+\pi^-$ spectrum to higher masses, whereas theory predicts the spectrum to appear at lower masses. The roles are inverted for the $\Sigma^-\pi^+$ channel. At the moment this interchange of the line shapes is under investigation.

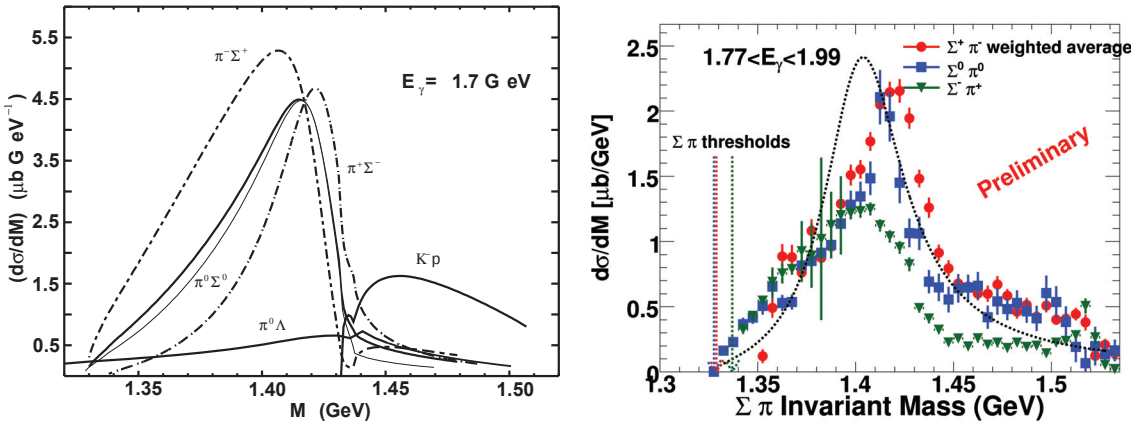

(a) (b)

Figure 1.3: Investigation of the reaction $\gamma p \to \Lambda(1405)K^+$. (a) Theoretical line shapes of the $\Lambda(1405)$, predicted in [Nac99] for a beam energy of $E_\gamma = 1.7$ GeV. (b) Invariant mass $(\Sigma\pi)$, showing the $\Lambda(1405)$ in the three different decay channels. The results are obtained for the energy range 1.77 GeV $< E_\gamma <$ 1.99 GeV [Mor10].

Concerning the effect of the different initial reactions, figure 1.4 shows the $\Lambda(1405)$ line shape for K^-p and π^-p reactions [Pra04][Tho73] together with theoretical calculations [Mag05][Hyo03].

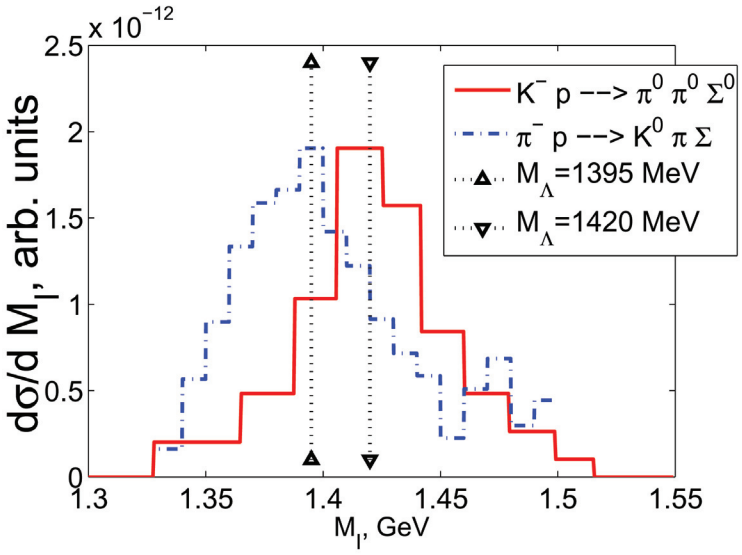

Figure 1.4: Line shape of the $\Lambda(1405)$ in different experiments and decay channels [Tho73][Pra04]. The vertical dashed lines indicate theoretical calculations for the expected pole masses.

As expected in the coupled channel approach, the pole masses are different for both reactions. This motivates further experiments with K^- and π^- beams to increase the available statistics and thus to allow a more precise comparison with the theoretical models.

A completely new interest in the $\Lambda(1405)$ was outed in connection with the prediction of deeply bound kaonic states starting from 2002 [Aka02]. Assuming that the $\Lambda(1405)$ is dominated by the K^-p bound state, it could act as a doorway for the production of a kaonic cluster. For example catching another proton, a ppK^- state could be produced, as it was recently investigated in [Mag09][Agn05]. However this phenomenological approach [Yam07] uses a simple potential model, not constrained by chiral SU(3), where the $\Lambda(1405)$ is assumed to have a one pole character. The pole emerges then only from the K^-p bound state, where its binding energy is set to 27 MeV, according to the PDG value of $m = 1405$ MeV/c^2 for the $\Lambda(1405)$ mass. In [Hyo08] the phenomenological ansatz was criticized, as it neglects the $\pi\Sigma \to \pi\Sigma$ coupling, appearing in the chiral dynamics approach. The inclusion of this additional coupling process leads to the two pole character of the $\Lambda(1405)$ (see above), where the $\bar{K}N$ quasibound state is located at $\sqrt{s} \approx 1420$ MeV/c^2. Consequently the binding energy is reduced to only 12 MeV, which makes the appearance of deeply bound kaonic clusters questionable.

Altogether the $\Lambda(1405)$ must be seen in the context of meson baryon interaction. Therefore it is possible to extract further important information about this particle from the investigation of old scattering experiments [Kit66][Eva83][Hum62] combined with recent results about kaonic atoms from the DEAR experiment [Car05]. The Deser-Trueman formula [Des54][Bor05] relates the K^-p scattering amplitude (a_{K^-p}) to the energy shift ΔE and

the width Γ of kaonic hydrogen:

$$\Delta E - \frac{i}{2}\Gamma = 2\alpha^3 \mu_c^2 a_{K^- p} \tag{1.1}$$

α is the fine-structure constant and μ_c is the reduced mass of the $K^- p$ system. In [Bor05] it was shown that chiral SU(3) effective theory can not describe satisfactorily the scattering data, if the constraints, set by the kaonic atoms measurement, are taken into account. This is illustrated in figure 1.5, where the scattering data for $K^- p \to \pi^- \Sigma^+$ (panel (a)) and $K^- p \to \pi^+ \Sigma^-$ (panel (b)) are fitted with different theoretical models.

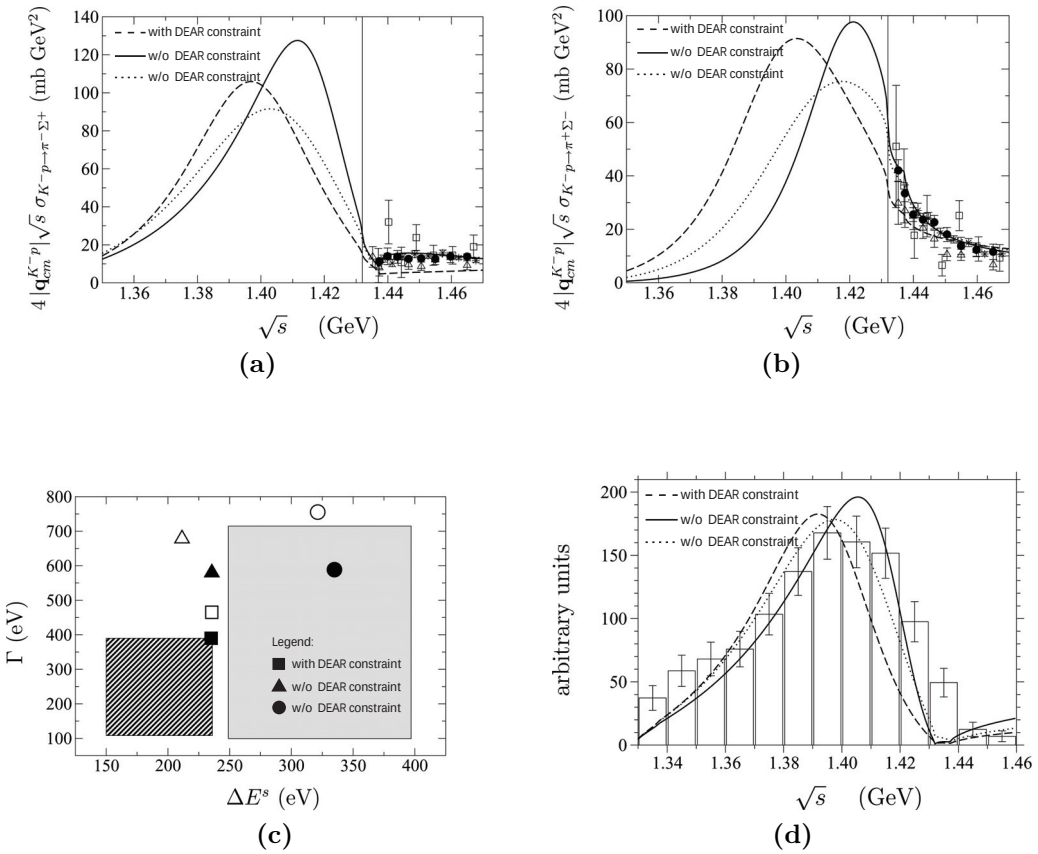

Figure 1.5: The upper panels show scattering data $K^- p \to \pi^- \Sigma^+$ (panel (a)) and $K^- p \to \pi^+ \Sigma^-$ (panel (b)), together with the different fit results. (c) the shaded box illustrates the DEAR data together with the experimental uncertainties. The black square, circle and triangle represent the different theoretical models and correspond to the dashed, solid and dotted lines in the other panels. (d) invariant mass ($\pi^- \Sigma^+$) spectrum from [Hem85], showing the $\Lambda(1405)$, together with the fits of the different theoretical models.

The dashed lines represent fits with a scattering amplitude $a_{K^- p}$, which is forced to supply values for ΔE and Γ within the DEAR uncertainties (shaded box in panel (c)). The values, obtained with a modification of equation (1.1), are shown as a black square in panel (c). As one can see, the fit underestimates the scattering data in both cases. The solid and dotted lines can describe the data much better, but calculating ΔE and Γ gives the black circle and black triangle in panel (c), which are not compatible with the DEAR experiment. By using the results of the scattering data, one can furthermore fit the $\Lambda(1405)$ line shape in panel (d) by taking into account (dashed line) or not taking into account (solid and dotted

line) the constraints, given by the DEAR experiment.
Summing up the presented results, theory is by now not able to deliver a totally consistent picture, concerning the meson baryon interaction in general and the $\bar{K}N$ interaction in particular. However, new measurements of $K^- + p$, $K^- + d$, $K^- + {}^3He$ and $K^- + {}^4He$ have been and will be carried out at DAϕNE, using the SIDDARTHA detector. New precision is expected from these results.
Recently the ANKE collaboration [Zyc08] investigated the decay $\Lambda(1405) \rightarrow \Sigma^0\pi^0$ in $p+p$ reactions at 2.83 GeV. The obtained line shape is in good agreement with previous data and was also compared to theoretical calculations [Ose07]. Unfortunately this measurement suffers from poor statistics, and was not able to improve the data base. Very recently the KLOE collaboration analyzed stopped K^- in ${}^4He$ atoms. The expected statistics will hopefully shed light on the K^-p interaction.
This work concentrates on the measurement of the $\Lambda(1405)$ with the HADES experiment. The presented analysis supplies the first data for the charged decay channels ($\Sigma^+\pi^-$,$\Sigma^-\pi^+$) in $p + p$ reactions. Besides the expansion of the data base, the results can act as a bench mark test for a possible ppK^- analysis with HADES.

2 The HADES Experiment

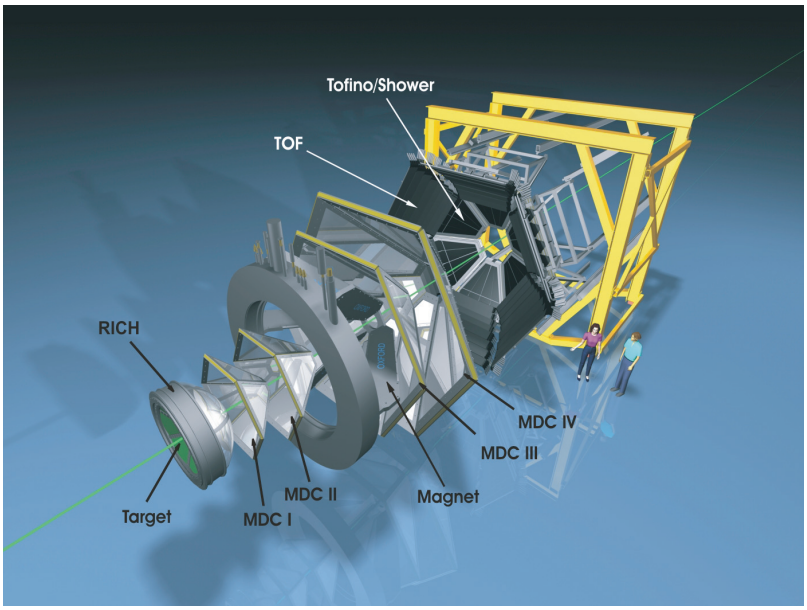

Figure 2.1: Exploded view of the HADES experiment. The beam is indicated by the green line.

The **H**igh **A**cceptance **Di**- **E**lectron **S**pectrometer (HADES) is located at the GSI Helmholtzzentrum für Schwerionenforschung in Darmstadt. Its heavy-ion program is focused on incident kinetic beam energies from 1 to 2 AGeV [Aga09c]. The detector system was especially designed to measure the in medium properties of the light vector mesons ρ, ω and ϕ [Lut92][Sha94] via its rare electromagnetic decay into $e^+ - e^-$ pairs. With lifetimes comparable to the duration of the compression phase of relativistic heavy ion collisions, these vector mesons can yield information about the quark-gluon condensate for a matter density of about $1-3\ \rho_0$ at a temperature of about $80-100$ MeV and the partial restoration of chiral symmetry breaking. Recently it was shown that the spectrometer also provides an ideal hadron identification, which opened the door for the investigation of strangeness physics [Sch08][Aga09b][Aga09a].
The HADES spectrometer is characterized by six identical sectors (see figure 2.1), defined by the superconducting coils, which produce the toroidal magnetic field geometry. It has an azimuthal acceptance of 85% and covers a polar angular range from $\theta = 18°$ to $\theta = 85°$. In this way the acceptance is optimized for the detection of di- leptons, coming from the decay of hadrons, produced at SIS 18 (Schwerionen Synchrotron) energies. In the following part the different components of the spectrometer, shown in figure 2.1 and 2.2 are described. The second part of this chapter focuses on the performance of particle identification.

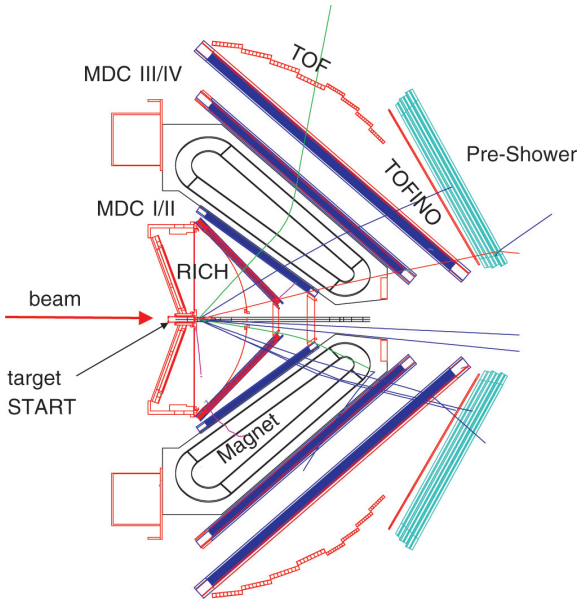

Figure 2.2: Cut side view of the HADES spectrometer, showing two of the six sectors.

2.1 Experimental setup

2.1.1 The reaction system

As a reference measurement for the reaction system $p + Nb$, measured in September 2008, a $p+p$ beam time was processed in April 2007. For both, the $p+Nb$ and the $p+p$ system, the beam energy was chosen to 3.5 GeV. The used liquid hydrogen (LH_2) target had a diameter of 25 mm and a length of 50 mm. For the beam time it was cooled down to 20 K at atmospheric pressure. The total interaction probability in the full target length is then about 0.7% for protons. In the $p + p$ run $1.2 \cdot 10^9$ LVL1 triggered events were collected. The LVL1 trigger condition was set to a minimum of three detected particles (M3 Trigger condition) in the **M**ultiplicity and **E**lectron **T**rigger **A**rray (META) (see subsection 2.1.6).

2.1.2 The RICH detector

In order to extract the rare decays of vector mesons in $e^+ - e^-$ pairs effectively, a special trigger detector is necessary (2nd level trigger). For that purpose the HADES experiment uses a Ring Imagining Cherenkov detector (RICH), shown in figure 2.3. It encloses the target region and covers in this way the full acceptance of the spectrometer [Fab03]. Cherenkov light appears, if charged particles traverse a medium with velocities above the characteristic velocity of light in the medium. The chosen radiator gas (C_4F_{10}) has a threshold value for Cherenkov radiation of $\gamma_{thr} = 18.3$, which at SIS energies is only reachable for electrons and positrons. The emitted Cherenkov cones traverse the radiator chambers, are reflected backwards by an aluminum coated carbon mirror and finally after passing a CaF_2 window of 5 mm thickness, the photons hit CsI photo cathodes. The subsequently knocked out photo electrons are accelerated and amplified by the six upstream Multi-Wire-Proportional Chambers (MWPC) (see blow-up picture in figure 2.3). The optical geometry is designed in a way that guarantees uniform Cherenkov rings across the whole detector plane.

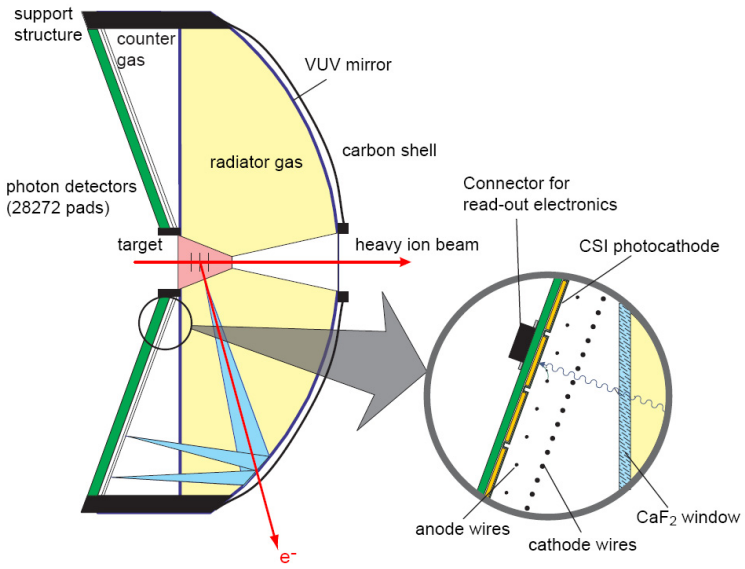

Figure 2.3: Cut side view of the Ring Imagining Cherenkov Detector (RICH). The blow-up picture shows the setup of the photo cathodes together with Multi-Wire-Proportional Chambers (MWPC). An traversing electron, which creates a Cherenkov light cone (blue colored cone), is indicated by the red line.

This allows an online identification of $e^+ - e^-$ pairs via an image processing unit (IPU). The RICH lepton identification combines with the PreShower and TOF or TOFino signal (see subsection 2.1.5 and 2.1.6)to the second level trigger (LVL2).
However, this work concentrates only on hadrons, thus the RICH detector is not used for the analysis.

2.1.3 The magnet

The determination of the momentum of particles with relativistic energies requires magnets with high field intensity. They make sure that the particle tracks, which are measured with the MDC chambers (see later), are bended. In the HADES experiment the superconducting magnet ILSE (**I**ron**L**ess **S**uperconducting **E**lectromagnet) is implemented between the 2nd and the 3rd layers of drift chambers (see figure 2.2 and 2.4, panel (a)). It consists of six coils surrounding the beam axis, which create an inhomogeneous toroidal magnetic field in the full azimuthal range. The design of the magnet foresees a very low field intensity in the region of the drift chambers ($B_{max} = 0.08$ T in MDC I, $B_{max} = 0.04$ T in MDC IV), of the RICH and of the TOF/TOFino detectors [Mar05]. In this way the measurement of the drift-times as well as the measurement of the time-of-flight is only slightly distorted. The $NbTi$ coils are cooled down with liquid helium at 4.6 K in order to stay below the critical temperature of $NbTi$ at about $10K$. The maximum current of 3460 A results in a magnetic field strength of 3.7 T inside the coil boxes and a strength of about 0.8 T in the midplane between the coils.

2.1.4 The MDC detectors

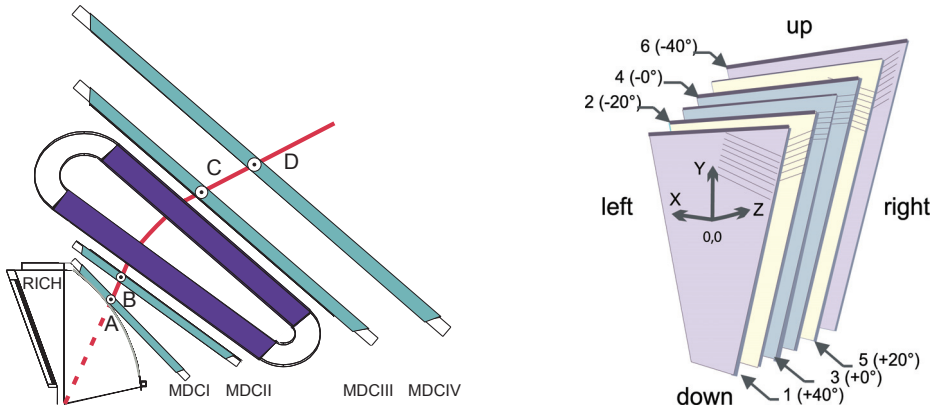

Figure 2.4: (a) Cut side view for one of the six identical sectors, which are used for the tracking procedure in HADES. The magnet coils are between MDC II and MDC III. The track determination is based on the measurement of penetration points in front of the magnetic field (A,B) and behind the magnetic field (C,B). (b) Schematic view of one of the 24 MDC modules, representing six stereo angles of the different layers.

The position information in the Multi Wire Drift Chambers (MDCs) together with the knowledge about the field strength, which is passed by the particle, are used for the tracking and momentum determination in the HADES experiment. The MDCs are arranged in six identical sectors, centered around the beam axis. Each sector consists of four drift chamber modules, two in front of the magnet, combining to MDC I and II, and two behind the magnet, combining to MDC III and IV. The setup for one of these sectors is illustrated in figure 2.4 (panel (a)). Each of the 24 modules consists itself of six wire planes, which exhibit altogether about 1200 signal wires. These planes are orientated in different stereo angles (see figure 2.4, panel (b)) in order to optimize the spatial resolution of the particle hit points. Special emphasis during the construction of the MDCs was put on the use of low-mass materials for the wires (aluminized Mylar) and for the counting gas (He : i-butane = 60 : 40), as this minimizes multiple scattering.
A charged particle ionizes the gas along its trajectory. The produced electrons drift in the electric field of the wires, are multiplied by avalanche effects and finally reach the wires, which induce an electronic signal. The cluster finder combines the position information of the different fired wires to calculate a penetration point of the particle in the MDCs with a spacial resolution of about 2 mm. Additionally the measured drift times t_i of the electrons define a cylinder with radius $r(t_i)$ around each wire. In general the particle track lies on the surface of all cylinders. This information is taken into account in the tracking algorithm, where the penetration point is recalculated with an improved space resolution of about 100 μm [Sch08][Mar05]. Besides the position determination, the MDC readout electronics (TDC chips) provide the possibility to measure the Time over Threshold (ToT) of the drift electrons. The signal width (ToT) is the time range, within the measured signal is above the adjusted threshold, and has a non-linear connection to the energy loss (dE/dx) of the particle in the MDCs. This energy loss measurement is an important feature for the particle identification, as will be shown later.
The momentum determination is done via the deflection of charged particles in the magnetic

field. The particle track is bended between MDC layer II and MDC layer III, as shown in figure 2.4 (panel (a)). The Runge-Kutta algorithm uses the information of the inner and outer track segments, obtained via the penetration points in the MDCs and in the META detectors, as start parameters. With this, the equation of motion of the particles under the influence of the magnetic field is solved numerically. This leads to a precise description of the particle track from the target to the META detector and thus to the appropriate momentum information. The momentum resolution with HADES was determined to about 4% in elastic $p+p$ reactions. A more detailed description of the tracking procedure can be found in [Aga09c].

2.1.5 The time-of-flight detectors TOF and TOFino

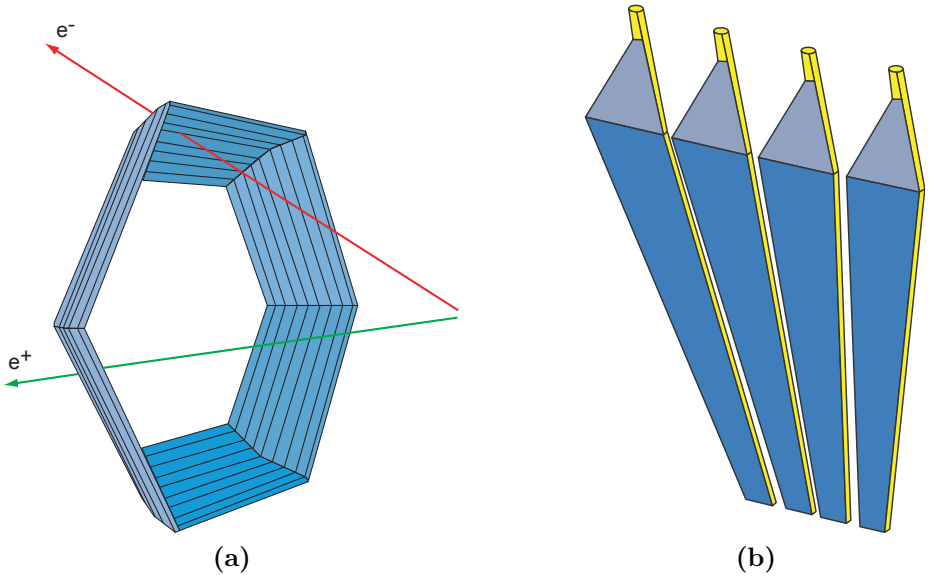

Figure 2.5: (a) The time-of-flight detector TOF is composed of six sectors, each with 8×8 scintillator strips. It covers a polar range from 44° to 88°. (b) The TOFino detector is also subdivided into six identical sectors, each consisting of four large scintillator strips. Its angular acceptance is from 18° to 45°.

The time-of-flight detector of HADES is split up in the TOFino detector, which covers the polar angle range from $\theta = 18°$ to $\theta = 45°$ and the TOF detector, covering the area from $\theta = 44°$ to $\theta = 88°$. Both detectors are shown in figure 2.5. The plastic scintillator strips of TOF and TOFino emit light, if a charged particle traverses them. The light signal is then read out by **P**hoto-**M**ultiplier-**T**ubes (PMTs), where besides the signal time also the signal hight is measured. Thus the measurement delivers the arrival time of the particles and the additional information about their energy loss in the detectors. This is used for the particle identification, as will be shown later.
The TOF detector consists of eight modules per sector, each with eight scintillator strips (see figure 2.5, panel (a)). The so obtained granularity guarantees a probability for double hits below 20% in central $Au+Au$ collisions. The strips of TOF are read out by PMTs on both sides, which allows a position resolution of the particle hit point in the order of cm [Sch08]. Altogether the TOF delivers a quite good time resolution of about 150 ps.
The TOFino detector, however, consists of only four strips per sector and is read out by only one PMT (see figure 2.5, panel (b)). This results in a rather poor time resolution of about

400 ps. The basic properties of the two time-of-flight detectors are summarized in table 2.1.

Detector	*TOF*	*TOFino*
polar angle coverage	$15° - 45°$	$44° - 88°$
granularity	8 modules of 8 strips	4 paddles
strip width	$20 - 30$ mm	10 mm
time resolution	≈ 150 ps	≈ 400 ps
spacial resolution	$25 - 27$ mm	-

Table 2.1: Properties of the two time-of-flight detectors TOF and TOFino.

Since 2009 the TOFino detector is replaced by Resistive Plate Chamber (RPC) Detectors, which cover the same polar and azimuthal angle range as TOFino. However their time resolution reaches values below 100 ps, which will improve the future particle identification with HADES essentially [Gil07].

2.1.6 The PreSHOWER detector

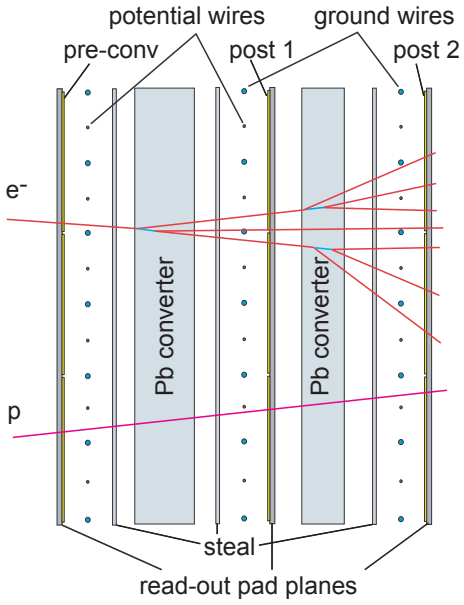

Figure 2.6: The PreSHOWER detector is located behind TOFino and consists of two layers of *Pb* converters, embedded between three wire chambers.

The PreSHOWER detector is located directly behind the TOFino detector (see figure 2.2) and provides a further possibility for the identification of leptons. It exploits the fact that fast leptons, unlike hadrons, cause an electromagnetic shower, which is due to Bremsstrahlung and pair production in the *Pb* converter planes (see figure 2.6). Altogether three wire chambers, filled with an counter gas mixture of Argon/i-Butan/Heptan, are located in front, between and behind the *Pb* converters. The signal of the particle shower is collected at the cathode of the chambers, which is divided into 942 read out pads. The

used pad size is optimized in order to push the double hit probability in $Au + Au$ collisions below 5%. In this way the poor position resolution of TOFino is compensated and double hits can be disentangled. The time-of-flight resolution of TOFino can only be reached with the improved position resolution due to the PreSHOWER detector. It is worth to mention that also hadrons deliver a shower in the detector, but their intensities are lower. In this way, leptons can be separated from hadrons.

The TOF and TOFino build together with the PreSHOWER detector the **M**ultiplicity and **E**lectron **T**rigger **A**rray (META). Besides the time-of-flight measurement (TOF and TOFino) and the electron/positron identification (PreSHOWER), this array is used to determine the particle multiplicity in each event and serves in this way as a 1st-Level-Trigger (LVL 1).

2.1.7 The Forward Wall

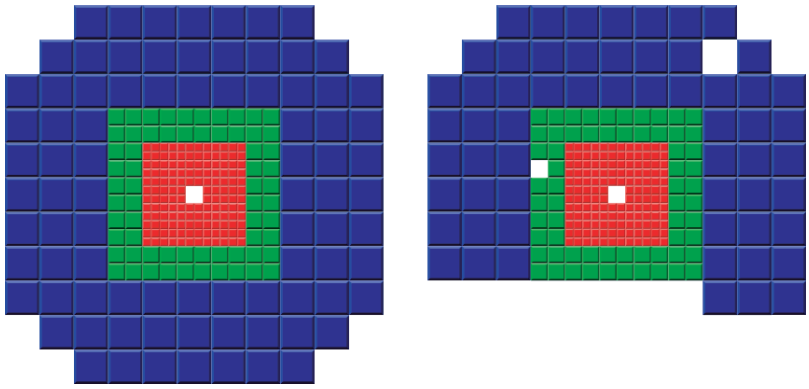

Figure 2.7: Left: Forward Wall with ideal geometry. The dimension of the cells increases with increasing polar angles (40×40 mm^2 $\rightarrow$ 80×80 mm^2 $\rightarrow$ 160×160 mm^2). Right: Scheme of the active cells during the $p + p$ measurement at 3.5 GeV.

During the $p + p$ beam time HADES was for the first time upgraded with a Forward Wall (FW) scintillator hodoscope. It consists of about 300 scintillating cells, each with a thickness of 2.54 cm. The chosen arrangement provides small cells in the middle of the FW, whereas the size increases for the outer cells (see figure 2.7). Altogether the FW allows the measurement of the hit position, of the arrival time with a time resolution of about 700 ps and also the energy loss of an incoming charged particle. The FW was placed 7 m downstream the target and covered in this way a polar angular range from 0.33° to 7.17° with full azimuthal acceptance [Lap09]. Consequently the momentum of the particle, hitting the FW, can not be determined, since the MDCs do not cover this low-angle range. Actually the FW was included for the $d + p$ beam time at 1.25 GeV in May 2007, where its function was to detect the spectator proton. The $p + p$ beam time was thus exploited for calibrations and for finding the correct settings. However, not all cells were active in this run, as can be seen in figure 2.7 (right picture). The data in the FW are not used for the analysis presented in this thesis, but it is possible to include them, as will be shown in the outlook.

2.2 Particle identification with the HADES spectrometer

The HADES spectrometer is especially designed for di- electron analysis and provides with the RICH detector ideal preconditions for the identification of leptons. However, for this thesis and in general for the investigation of strangeness physics, the identification of hadrons is important, which can be realized in different ways.

2.2.1 Identification of hadrons via their energy loss

When a charged particle flies through a medium, it ionizes the atoms in this medium. Consequently a part of its kinetic energy is transfered to the shell electrons. The theoretical energy loss dE of a particle, covering a distance dx, is expressed in the well known Bethe-Bloch formula, which reads as follows [Bet53]:

$$-\left\langle \frac{dE}{dx} \right\rangle = 4\pi N_A r_e^2 m_e c^2 z^2 \frac{Z}{A}\frac{1}{\beta^2}\left[\frac{1}{2} ln\left(\frac{2m_e c^2 \beta^2 \gamma^2 T_{max}}{I^2}\right) - \beta^2 - \frac{\delta}{2}\right] \tag{2.1}$$

with:

z : charge of the incident particle

Z,A : atomic- and mass number of the traversed medium

m_e : rest mass of the electron

r_e : Bohr electron radius

N_A : Avogadro number

I : mean excitation potential of the material

δ : density correction

The kinetic energy T_{max}, which can be transfered, is limited:

$$T_{max} = \frac{2m_e c^2 \beta^2 \gamma^2}{1 + 2\gamma m_e/M + (m_e/M)^2} \tag{2.2}$$

with:

M : mass of the incident particle

Equation (2.1) is valid for particles with rest masses much larger than the electron rest mass. In this case, the energy loss depends only on the velocity β and the particle charge $z \cdot e$. For a fixed value of the momentum p, which depends on β and on the mass m (see equation (2.3)), the dE/dx vs. momentum distribution must be different for different particle species. This can be exploited for particle identification.
As it was shown in the last section, the MDCs as well as the TOF and TOFino detector supply the additional information about the energy loss of a detected particle. Together with the momentum, obtained in the tracking procedure, the dE/dx vs. momentum distribution can be investigated. This is exemplary shown for the MDCs in figure 2.8. Distributions due to pions and protons are visible and are clearly separated up to about 600 MeV/c. This allows at least an identification of pions and protons with low momenta via 2- dimensional graphical cuts. However, the same procedure can be applied for the kaon identification, although kaons are not visible in figure 2.8.

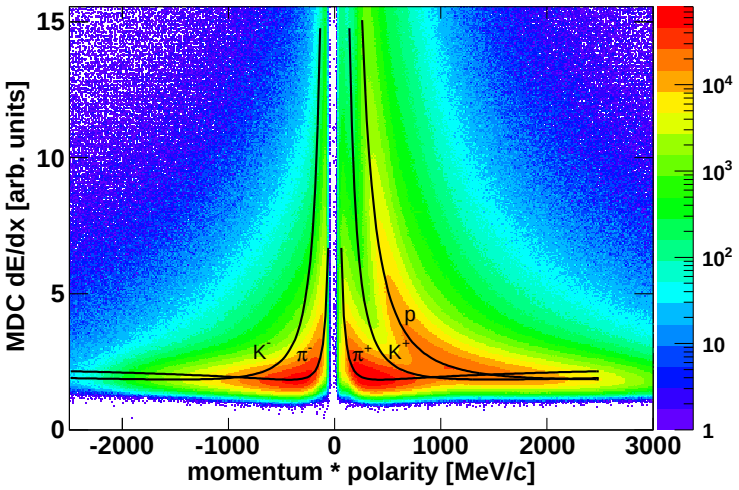

Figure 2.8: dE/dx vs. momentum distribution of charged particles in the MDC detectors. Modified Bethe-Bloch curves (black lines) mark the areas, where pions, protons and kaons are expected.

The realization of the presented method will be explained in detail using the example of the $\Lambda(1405)$ analysis in chapter 4.

2.2.2 Time-of-flight reconstruction

The HADES spectrometer provides in principle the possibility to measure the time-of-flight of particles. As the tracking algorithm delivers besides the momentum p also the complete particle track and thus also its path length, the velocity $\beta = v/c$ can be determined. This allows the calculation of the particle mass m:

$$p = mc\frac{\beta}{\sqrt{1-\beta^2}} \tag{2.3}$$

With this information, one can additionally and independently identify particles to be of a special kind (e.g. a proton), by requiring the calculated mass to be within an appropriate range around the nominal mass of the particle.
Unfortunately the $p+p$ experiment, which is discussed here, was not equipped with a start detector. Thus the taken data can provide a stop time for each particle that had a META hit, but a time-of-flight is not directly accessible. It is, however, possible to reconstruct a start time for each event. The method, with which this is done, was especially developed for the analysis of the $\Lambda(1405)$ but can also be applied to other reactions.
In a first step of iteration particles can be identified via their energy loss in the MDCs and in the TOF or TOFino detectors, as it is described above. In this way they are set to the appropriate nominal mass of protons or pions etc. If the particle has also a META hit and is thus tagged with an arrival time in the time-of-flight detectors, a specific start time $t_{0,i}$ can be reconstructed, according to equation (2.3). $t_{0,i}$ is calculated separately for each particle i of one event. In order to obtain a common start time for the event, a weighted

mean value $\bar{t}_0$ is determined with the following formula:

$$\bar{t}_0 = \frac{\sum_{i=1}^{n} w_i t_{0,i}}{\sum_{i=1}^{n} w_i} \tag{2.4}$$

The particle index i runs from 1 to n, where n is the number of used particles in the event. w_i are weighting factors, which take into account, if the particle had a hit in the TOF detector ($w_i = 2.5$) or in the TOFino detector ($w_i = 1.0$). The choice of the weighting factors is motivated by the fact that the time resolution of the TOF is about 2.5 times better than the one of TOFino (see table 2.1). Thus a measured stop time in the TOFino is less confidential and should have a lower weighting for the start time reconstruction. To further increase the accuracy of the calculation, a start time $t_{0,i}$, which deviates from the calculated mean value $\bar{t}_0$ by more than a maximum value Δt_{max}, is excluded from the reconstruction (truncated mean). This is done in order to suppress outliers in the measurement. For the analysis in chapter 4, Δt_{max} is chosen to 400 ps, according to the TOFino time resolution. After the rejection of this track, $\bar{t}_0$ is recalculated and the procedure is eventually repeated until at least two tracks remain.
With the so obtained $\bar{t}_0$, the mass of each particle in the event can be determined by using equation (2.3). The different weighting factors w_i for the TOF and the TOFino as well as the truncated mean calculation are applied in order to optimizes the resolution of the reconstructed start time and consequently also to optimize the mass resolution. This is essential for a reliable particle identification.
In contradiction to the statements at the beginning of this subsection, the obtained mass does not supply a completely independent possibility for the particle identification. Since the start time is reconstructed with help of the nominal masses of the particles, which are itself determined via the energy loss measurement, the presented time-of-flight reconstruction is biased by the first identification method. This can be problematic, if a particle j is initially misidentified, since this would result in a wrong start time $t_{0,j}$ and thus also in an incorrect common event start time $\bar{t}_0$. Therefore it is advisable to exclude kaon candidates from the start time reconstruction, since their misidentification rate is rather high. Nevertheless the other particles of the event can be used to obtain a $\bar{t}_0$ value and with this it is also possible to recalculate the mass of the kaon candidates. They can then be purified by cuts on appropriate mass areas, as it will be discussed in detail in chapter 4.

The efficiency and purity of the K^+ identification, done with the two presented methods, was investigated with help of simulations in [Epp09]. It was shown that in the exclusive analysis of the $\Lambda(1405)$, a common start time $\bar{t}_0$ could be reconstructed in almost all events (100% efficiency for time-of-flight reconstruction). However, a fair identification of kaons requires the additional application of optimized dE/dx- cuts and cuts on the calculated mass distribution (see chapter 4). In this way, the efficiency of the K^+ identification is reduced, whereas the purity of the obtained kaon sample is increased. Depending on the strictness of these cuts, the K^+ purity was determined to be about $2-4\%$ with an efficiency of $50-20\%$. Although the method for the start time reconstruction and the dE/dx-cuts, investigated in [Epp09], are slightly different to what is presented in this thesis, the quantities for the kaon purity and efficiency should be comparable.

2.2.3 Invariant and missing mass technique

In some reactions particles with short lifetimes are produced. They decay before they reach the detectors and can thus not be measured directly. Nevertheless it is possible to reconstruct these particles.
If all decay particles of the mother particle are detected and identified, one can apply the invariant mass technique. Here the energy E_i and the three momentum $\vec{p}_i$ of all daughter particles i are added up in order to obtain the appropriate values E and $\vec{p}$ for the mother particle. With these quantities it is then possible to calculate the invariant mass of the mother particle:

$$m_{inv} = \frac{1}{c^2}\sqrt{E^2 - (\vec{p})^2\, c^2} = \frac{1}{c^2}\sqrt{\left(\sum_{i=1}^{n} E_i\right)^2 - \left(\sum_{i=1}^{n} \vec{p}_i\right)^2 c^2} \tag{2.5}$$

where n is the number of the daughter products.
In elementary reactions another method for the particle reconstruction can be applied, the missing mass technique. It is also based on the idea to calculate the mass of a particle by exploiting energy and momentum conservation. Assumed that a particle is produced together with n other particles i, which are all detected, the missing energy E and the missing momentum $\vec{p}$ can be determined. The missing mass of the particle reads as follows:

$$\begin{aligned} m_{miss} =& \frac{1}{c^2}\sqrt{E^2 - (\vec{p})^2\, c^2} = \\ =& \frac{1}{c^2}\sqrt{\left(E_b + E_t - \sum_{i=1}^{n} E_i\right)^2 - \left(\vec{p}_b + \vec{p}_t - \sum_{i=1}^{n} \vec{p}_i\right)^2 c^2} \end{aligned} \tag{2.6}$$

(E_b,$\vec{p}_b$) and (E_t,$\vec{p}_t$) are the four momenta of the beam and the target particle, respectively. In the following chapters, the two presented methods are exemplified with several examples.

3 The Kinematic Refit

The kinematic refit is a well known tool in the exclusive analysis of elementary particle reactions [Rus06] [Nii08]. The main result of applying the refit is an improvement in the mass resolution of particles, reconstructed via invariant- or missing mass technique. Since a new and exact measurement of the $\Lambda(1405)$ line shape is the main goal of this work, an improved mass resolution could be essential. This chapter describes the kinematic refit in detail. A theoretical description is given and the application on simulated, as well as on experimental data is discussed. The first part of this chapter gives a motivation for the refit and introduces the mathematical background. The mathematical procedure is described in more detail in the write-ups by Paul Avery [Ave98]. The application on simulated data is presented in the second part. The third part focuses on the quality criteria of the refit, mainly determined by two parameters: the χ^2-distribution and the so called Pull−distributions. These quantities will be illustrated with help of simulations. The final tests of the refit procedure are carried out, using experimental data, and the relevance of the refit on the $\Lambda(1405)$ analysis is pointed out.

3.1 Motivation and mathematical background

Today most detector systems provide the possibility to get the full kinematic information of each measured particle. These informations can be for example the momentum p, the polar angle ϑ and the azimuthal angle φ. If one furthermore determines the particle identity, one can calculate the energy for a complete description. With these track parameters $(E_i,p_i,\vartheta_i,\varphi_i)$ or equivalently $(E_i,p_{x,i},p_{y,i},p_{z,i})$ of all measured particles i in one event, the properties (especially the mass) of intermediate particles can be reconstructed. This is explained with the following example (equation(3.1)):

$$\begin{aligned} p + p \rightarrow X + p + p \\ \hookrightarrow \pi^- + \pi^+ \end{aligned} \tag{3.1}$$

Assumed that all the charged tracks are detected (two protons and two pions), one can determine the mass of the intermediate particle X (e.g. this could be a η or ω) either via the invariant mass of the two pions or the missing mass of the two protons (see chapter 2). It is clear, however, that the measured parameters are imprecise due to the finite resolution of the tracking system. As a consequence, also the reconstructed parameters of intermediate particles will only be known within an error, which furthermore results in a finite mass resolution.
One can now go further and require that in these elementary reactions the detected particles should fulfill physical constraints. With the uncertainties in the tracking procedure, this will in general not exactly be the case for the measured parameters. If we consider again the example (3.1), there are the following options:

- If in one event the four charged particles are measured, the physical constraint is obviously that momentum and energy has to be conserved.
- If only three of these particles are detected, a physical constraint is that the missing mass of the three measured particles should give the mass of the remaining undetected particle.

The main goal of the kinematic refit is now to improve the mass resolution of particles, reconstructed via the invariant- or missing mass technique, by taking into account the physical constraint conditions. The kinematic refit is performed for each event and calculates new parameters for all particles, which then fulfill the physical constraint conditions. At the same time the refit makes sure that the new parameters stay as close as possible to the measured parameter set by taking into account the uncertainties of the measurement. Doing this, one can expect that the new parameters are in general closer to the true parameters. However, this is only valid, if also the true track parameters really fulfill the constraints, which is not always the case (e.g. if background is present). Mathematically the calculation is done by minimizing the following equation with respect to $\vec{\alpha}$ and $\vec{\lambda}$ [Rus06]:

$$L = (\vec{\alpha} - \vec{\alpha}_0)^T \mathbf{V}_{\vec{\alpha}_0}^{-1} (\vec{\alpha} - \vec{\alpha}_0) + 2\vec{\lambda}^T \vec{H}(\vec{\alpha}) \tag{3.2}$$

Here $\vec{\alpha}_0$ is the $(3n)$- dimensional vector of measured parameters
(e.g. $\vec{\alpha}_0 = (p_{x,1}, p_{y,1}, p_{z,1}, p_{x,2}, ..., p_{z,n})$ with n particles). $\vec{\alpha}$ is the vector, which contains the parameters, calculated by the refit. The $(3n \times 3n)-$matrix $\mathbf{V}_{\vec{\alpha}_0}^{-1}$ is the inverse of the covariance matrix with the uncertainties of the parameters $\vec{\alpha}_0$ as an input. $\vec{H}(\vec{\alpha})$ is the $(r)-$dimensional vector of constraint conditions and $\vec{\lambda}$ is a $(r)-$dimensional Lagrange vector. The factor 2 in this equation is only included to simplify further calculation. At this point one should mention that the refit requires the errors of the detected tracks to be statistical, meaning Gaussian distributed. Only if this is the case, the refit can work mathematically correctly. The effect of systematic errors in the measurement will be discussed in section 3.3. Furthermore the knowledge of these uncertainties is a requirement for the refit. But even if this information is not accessible directly in the tracking procedure, it can partially be extracted from the Pull−distributions (see section 3.3).
The first summand in equation (3.2) delivers a mean square$-\chi^2-$value and guarantees that $\vec{\alpha}$ stays close to the measurement $\vec{\alpha}_0$. The second summand forces the calculated parameters $\vec{\alpha}$ to fulfill the constraints.
Figure 3.1 provides a visualization of how the kinematic refit works. Here the $(3n)-$ dimensional parameter room is reduced to 2 dimensions ($\vec{\alpha}^T = (\alpha_1, \alpha_2)$). The physical constraint conditions are indicated by the solid line, which is a hyper plane in the parameter space. The perfect parameters $\vec{\alpha}_i$ lie on this plane. The measurement delivers the parameters $\vec{\alpha}_0$, which in general do not fulfill the constraints. The error band, within $\vec{\alpha}_0$ is known, is indicated by the green ellipsoid. Applying the refit procedure leads to the point $\vec{\alpha}$, which is, by taking into account the error band of $\vec{\alpha}_0$, the nearest point on the solid line. One can furthermore see that $\vec{\alpha}$ is closer to $\vec{\alpha}_i$ than $\vec{\alpha}_0$, and therefore will describe the reaction better. Nevertheless one can easily imagine a case, where $\vec{\alpha}$ lies on the line of constraints, but is slightly more distant to $\vec{\alpha}_i$ as $\vec{\alpha}_0$. Indeed, applying the refit does not guarantee a result, which is closer to the real values with respect to the measured ones, but since the physical constraints are fulfilled, the probability for this is high.

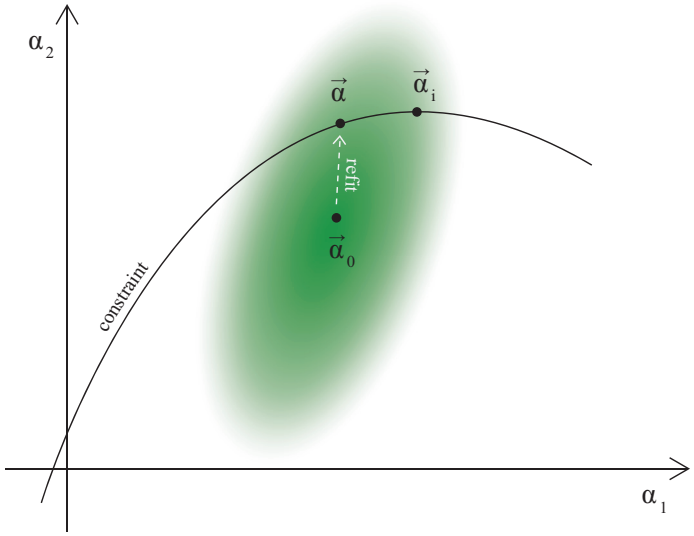

Figure 3.1: The refitted point $\vec{\alpha}$ lies on the constraint plane (solid line) and simultaneously takes into account the error band (transparent ellipsoid), within the measurement $\vec{\alpha}_0$ is known. The improved closeness to the true point $\vec{\alpha}_i$ compared with $\vec{\alpha}_0$ is visible, but is not a necessary consequence of the kinematic refit.

Going back to equation (3.2), one can write the r functions of constraints as:

$$\vec{H}\left(\vec{\alpha}\right) \equiv \vec{0} \tag{3.3}$$

These functions are in general not linear in the parameters $\vec{\alpha}$ and hence the minimization of equation (3.2) must be applied iteratively. Therefore one defines first a convenient point $\vec{\alpha}_A$ (e.g. $\vec{\alpha}_0$) and expands $\vec{H}\left(\vec{\alpha}\right)$ around this point.

$$\vec{0} = \vec{H}\left(\vec{\alpha}\right) \approx \left[\partial\vec{H}\left(\vec{\alpha}_A\right)/\partial\vec{\alpha}\right]\left(\vec{\alpha} - \vec{\alpha}_A\right) + \vec{H}\left(\vec{\alpha}_A\right) = \mathbf{D}\delta\vec{\alpha} + \vec{d} \tag{3.4}$$

where $\delta\vec{\alpha} = \vec{\alpha} - \vec{\alpha}_A$. The matrix $\mathbf{D}$ and the vector $\vec{d}$ are

$$\mathbf{D} = \begin{pmatrix} \frac{\partial H_1}{\partial \alpha_1} & \frac{\partial H_1}{\partial \alpha_2} & \cdots & \frac{\partial H_1}{\partial \alpha_{3n}} \\ \frac{\partial H_2}{\partial \alpha_1} & \frac{\partial H_2}{\partial \alpha_2} & \cdots & \frac{\partial H_2}{\partial \alpha_{3n}} \\ \vdots & \vdots & \ddots & \vdots \\ \frac{\partial H_r}{\partial \alpha_1} & \frac{\partial H_r}{\partial \alpha_2} & \cdots & \frac{\partial H_r}{\partial \alpha_{3n}} \end{pmatrix} \qquad \vec{d} = \begin{pmatrix} H_1\left(\vec{\alpha}_A\right) \\ H_2\left(\vec{\alpha}_A\right) \\ \vdots \\ H_r\left(\vec{\alpha}_A\right) \end{pmatrix} \tag{3.5}$$

The linearized Lagrange equation

$$L = \left(\vec{\alpha} - \vec{\alpha}_0\right)^T \mathbf{V}_{\vec{\alpha}_0}^{-1} \left(\vec{\alpha} - \vec{\alpha}_0\right) + 2\vec{\lambda}^T \left(\mathbf{D}\delta\vec{\alpha} + \vec{d}\right) \tag{3.6}$$

can be minimized analytically with respect to $\vec{\alpha}$ and $\vec{\lambda}$ and yields two vector equations:

$$\mathbf{V}_{\vec{\alpha}_0}^{-1}\left(\vec{\alpha} - \vec{\alpha}_0\right) + \mathbf{D}^T\vec{\lambda} = \vec{0} \tag{3.7}$$

$$\mathbf{D}\delta\vec{\alpha} + \vec{d} = \vec{0} \tag{3.8}$$

Equation (3.8) clearly shows that the solution will fulfill the linearized constraint conditions. Solving (3.7) and (3.8) with respect to $\vec{\alpha}$ and $\vec{\lambda}$ leads to the following results:

$$\vec{\lambda} = \mathbf{V}_D \left(\mathbf{D}\delta\vec{\alpha}_0 + \vec{d} \right) \tag{3.9}$$

$$\vec{\alpha} = \vec{\alpha}_0 - \mathbf{V}_{\vec{\alpha}_0}\mathbf{D}^T\vec{\lambda} = \vec{\alpha}_0 - \mathbf{V}_{\vec{\alpha}_0}\mathbf{D}^T\mathbf{V}_D \left(\mathbf{D}\delta\vec{\alpha}_0 + \vec{d} \right) \tag{3.10}$$

$$\mathbf{V}_D = \left(\mathbf{D}\mathbf{V}_{\vec{\alpha}_0}\mathbf{D}^T \right)^{-1} \tag{3.11}$$

It is interesting to see that only a single matrix has to be inverted for the calculations, the $(r \times r)-$matrix $\mathbf{V}_D$. The covariant matrix $\mathbf{V}_{\vec{\alpha}}$, associated to the parameters $\vec{\alpha}$, reads:

$$\Delta\vec{\alpha} = \frac{\partial\vec{\alpha}}{\partial\vec{\alpha}_0}\Delta\vec{\alpha}_0 = \Delta\vec{\alpha}_0 - \mathbf{V}_{\vec{\alpha}_0}\mathbf{D}^T\mathbf{V}_D\mathbf{D}\Delta\vec{\alpha}_0 \tag{3.12}$$

$$\begin{aligned} \mathbf{V}_{\vec{\alpha}} &= \Delta\vec{\alpha}\Delta\vec{\alpha}^T \overset{3.12}{=} \ldots = \\ &= \mathbf{V}_{\vec{\alpha}_0} - \mathbf{V}_{\vec{\alpha}_0}\left(\mathbf{D}^T\mathbf{V}_D\mathbf{D} \right)\mathbf{V}_{\vec{\alpha}_0} \end{aligned} \tag{3.13}$$

The result (3.13) can be extracted from the general Gaussian error propagation. One can also show that the diagonal elements of $\mathbf{V}_{\vec{\alpha}}$ are always reduced compared to the ones of $\mathbf{V}_{\vec{\alpha}_0}$. This will be important, when the quality criteria of the kinematic refit are discussed (see section 3.3).
By now only the first step of iteration was done, with $\vec{\alpha}_A = \vec{\alpha}_0$. The calculated parameters $\vec{\alpha}$ can be used as input for the second step ($\vec{\alpha}_A = \vec{\alpha}$) and equation (3.6) can again be solved in the way described above. This procedure is repeated several times (usually 5 to 10 steps of iteration are sufficient). Finally the constraints $\vec{H}\left(\vec{\alpha}\right)$ are exactly satisfied in most cases (see section 3.2).

3.2 Application of the kinematic refit to simulations

Two different parameterizations of the measured particles can be used in the developed refit (${\vec{\alpha}_0}^T = (1/p_1,\vartheta_1,\varphi_1,\ldots)$ or ${\vec{\alpha}_0}^T = (p_{x,1},p_{y,1},p_{z,1},\ldots)$). Furthermore one can choose between using one or two constraints. The first parameter set is the preferred one in the analysis of real data. Since the tracking algorithm of HADES determines the momentum via the curvature of the tracks, and this curvature is proportional to $1/p$ [Sch09][Rus06], the uncertainty of this quantity is Gaussian distributed, as required by the refit.
The refit procedure was tested using simulations, in which all physical constraints are sharply fulfilled. Since the kinematic refit was developed to investigate the $\Lambda(1405)$ resonance, the following reaction was simulated with $1 \cdot 10^5$ events:

$$\begin{aligned} p + p \xrightarrow{3.5GeV} & \Lambda(1405) + p_1 + K^+ \\ & \hookrightarrow \Sigma^+ + \pi^- \\ & \hookrightarrow p_2 + \pi^0 \end{aligned} \tag{3.14}$$

The line shape of the simulated $\Lambda(1405)$ follows a relativistic Breit-Wigner function with a pole mass of 1405 MeV/c^2 and a width of 50 MeV/c^2. The Σ^+ however has a quite long lifetime ($c\tau \approx 2cm$), and is therefore simulated as having exactly a mass of 1198 MeV/c^2

with almost no width. The detectable tracks in reaction (3.14) are the two protons, the K^+ and the π^-. To simulate the finite detector resolution of the HADES spectrometer, the momentum of each particle was Gaussian smeared by 2.5%, ϑ and φ were smeared within an interval of 0.05°. This choice is consistent with the resolution of HADES [Aga09c]. One gets the following properties for equation (3.2) or equation (3.6) according to the particle set (p_1,K^+,π^-,p_2) :

$$\vec{\alpha} = \begin{pmatrix} 1/p_{p_1} \\ \vartheta_{p_1} \\ \varphi_{p_1} \\ 1/p_{K^+} \\ \vdots \end{pmatrix} \qquad \mathbf{V}_{\vec{\alpha}_0} = \begin{pmatrix} \sigma^2(1/p_{p_1}) & 0 & 0 & 0 & \dots \\ 0 & \sigma^2(\vartheta_{p_1}) & 0 & 0 & \dots \\ 0 & 0 & \sigma^2(\varphi_{p_1}) & 0 & \dots \\ 0 & 0 & 0 & \sigma^2(1/p_{K^+}) & \dots \\ \vdots & \vdots & \vdots & \vdots & \ddots \end{pmatrix}$$

$\vec{\alpha}_0$ is a 12−dimensional vector and $\mathbf{V}_{\vec{\alpha}_0}$ is a (12×12)−matrix. In the real tracking procedure, the momentum resolution depends on the strength of the magnetic field, experienced by the particle [Aga09c]. The field strength itself depends on the polar angle ϑ and also on φ. This leads to a correlation between the momentum p and ϑ or p and φ and thus also to outer diagonal elements in $\mathbf{V}_{\vec{\alpha}_0}$. For simplicity these kind of correlations were not implemented in the simulations.
The constraint conditions, which can be used in reaction (3.14), are first of all the missing mass of all charged particles being the mass of the π^0. Furthermore, it is possible to use the intermediate Σ^+ for a second constraint. The two constraints H_1 and H_2 read as follows:

$$H_1 = MM(p_1,K^+,p_2,\pi^-) - M(\pi^0) = 0 \tag{3.15}$$

$$H_2 = MM(p_1,K^+,\pi^-) - M(\Sigma^+) = 0 \tag{3.16}$$

Figure 3.2 shows the missing mass (p_1,K^+,p_2,π^-) before and after the refit using one or two constraints. The black distributions show the π^0 mass before the refit. They have a large width, which is of course due to the artificial smearing of the track parameters, but still they are centered around the nominal π^0 mass of 134.9 MeV/c^2. After applying the one constraint refit (figure 3.2, top panel), the red histogram is obtained, which is close to a delta function, fixed on the correct mass. This behavior is exactly what is expected, since the π^0 mass was a direct input into the refit. Also in the case of using both constraints (figure 3.2, bottom panel, blue histogram) the π^0 constraint is fulfilled.
However, there are still some refitted events, which do not deliver the nominal π^0 mass. They correspond to the left tail in the red and blue distributions. A possible explanation could be that there are sometimes local minima, in which $\vec{\alpha}$ is trapped. The slopes do not even vanish, when the number of iterations is increased. Thus it is not a problem of accuracy. Nevertheless, only about 0.06 % of the refitted events differ from the nominal π^0 mass more than 6 MeV/c^2.

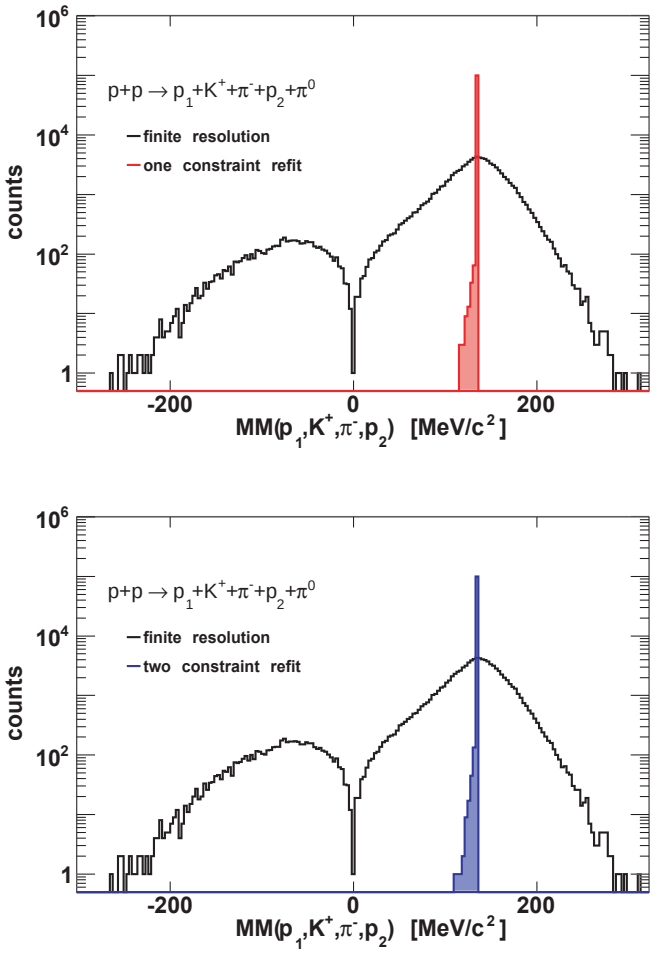

Figure 3.2: Missing mass of all charged particles, showing the π^0, before and after the kinematic refit with one constraint condition (top) and with two constraint conditions (bottom).

A further interesting point is that the tail of the refitted data only appears on the left side of the π^0 mass. This behavior can be understood in a simplified picture (figure 3.3). Assuming that all parameters but one (e.g $1/p_{K^+}$) of the four charged particles are measured without any uncertainty, the problem is reduced from 12 to 1 dimension. The function $H(\alpha)$ can now be plotted vs. this free parameter (solid black line in figure 3.3). The constraint condition is satisfied, if $H(\alpha) = 0$. If the measured point α_0 lies above the x−axis, the missing mass is larger than the nominal π^0 mass. The linearization of the problem, like it is done in the refit, delivers the blue tangent to the curve and a new value α_1. This new parameter goes hand in hand with a missing mass, which is to low. Going on with this linearization procedure will produce values $(\alpha_2, \alpha_3 \ldots \alpha_n)$, which approach the constraint $(H(\alpha) = 0)$, but the missing mass will always be below the nominal one. This is also the case, if the initial measured value is lower than the nominal π^0 mass, as can be seen easily.

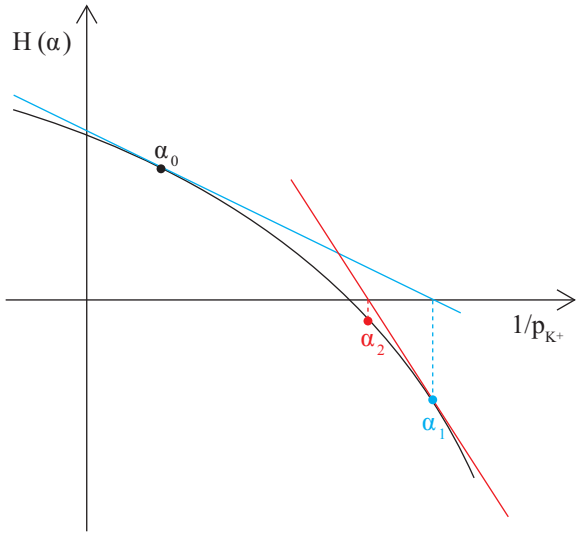

Figure 3.3: Visualization of the iterative refitting procedure.

In order to reconstruct the intermediate Σ^+, the missing mass of p_1, K^+ and π^- has been built ($MM(p_1,K^+,\pi^-)$). The resulting distributions are plotted in figure 3.4. The black histogram shows the simulated data with the finite resolution. Visible in the red histogram is the Σ^+, obtained after applying the one constraint refit on the missing π^0. The resonance is remarkably reduced in width. The relevance of this effect is discussed in chapter 4, where real data are investigated. The two constraint refit fixes the missing mass of the three particles to the Σ^+ mass of 1198 MeV/c^2 (figure 3.4, blue histogram), like it is expected.

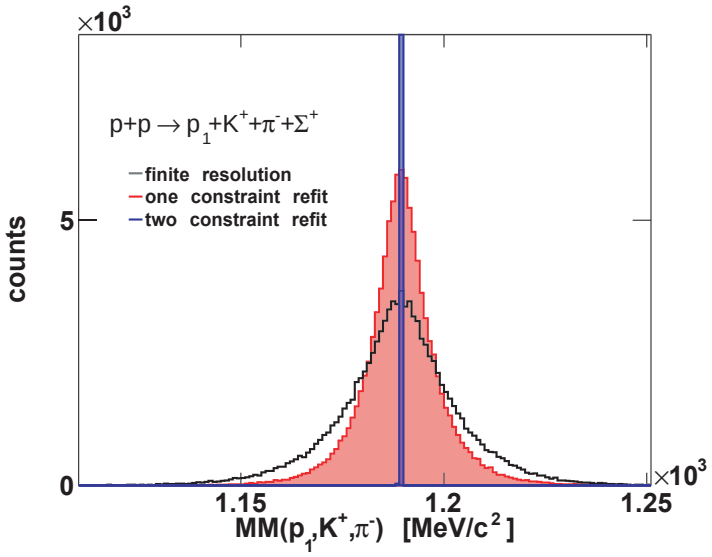

Figure 3.4: Missing mass of p_1,K^+ and π^-, showing the Σ^+ before and after the kinematic refit with one or two constraint conditions.

Finally figure 3.5 shows the missing mass of the proton and the K^+ ($MM(p_1,K^+)$), which is used to reconstruct the $\Lambda(1405)$. The green plots are the data, like they are directly generated in the simulation. Thus it corresponds to a perfect measurement with an ideal

resolution. Comparing the black histogram to these data, it is again clear that the finite resolution increases the width of the reconstructed resonance. The effect of the kinematic refit is visible in the red and blue plots. It is remarkably that in both cases the original line shape of the $\Lambda(1405)$ is reconstructed quite well. Requiring the $MM(p_1,K^+,\pi^-)$ having sharply the Σ^+ mass, leads to a better description of the initial physical process, and thus the refit with two constraints is even an improvement compared to the refit with one constraint.
Especially for the investigation of the forward wall data (see chapter 6) the refit will be essential, because here the momentum resolution is very poor.
The next part of this chapter will concentrate on the quality criteria of the refit, and will discuss their meaning on the simulated data set.

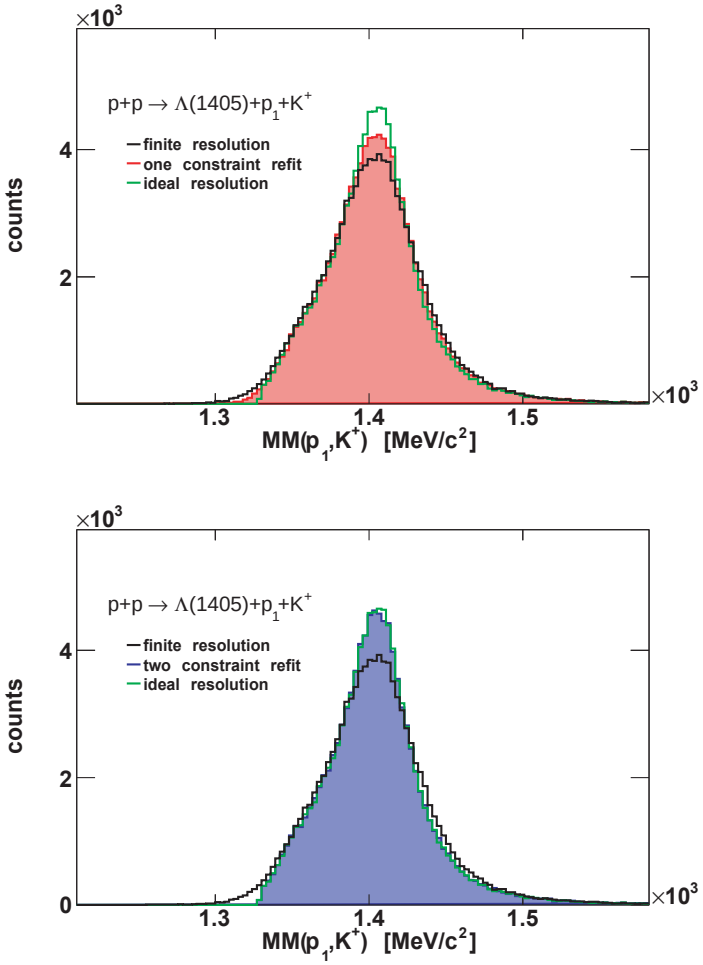

Figure 3.5: Missing mass of p_1 and K^+, showing the $\Lambda(1405)$, before and after the kinematic refit with one constraint condition (top) or two constraint conditions (bottom).

3.3 Quality criteria of the kinematic refit

Since the uncertainties of the track parameters in the simulated data set are created artificially, the correct input for $\mathbf{V}_{\vec{\alpha}_0}$ is known. This is in general not the case for experimental

data, where the errors have to be estimated. But even if the estimations are not correct, the refit will force the parameters $\vec{\alpha}$ to satisfy the constraints. The result is that some of the refitted parameters in $\vec{\alpha}$ are not shifted inside the correct error band. Consequently they are too far away or unnecessary close to $\vec{\alpha}_0$. Since physics should be described more realistic by the refit, this is undesirable.
Therefore the kinematic refit procedure in section 3.1 provides some quality criteria, which can indicate, whether the errors were estimated correctly or not.

3.3.1 χ^2-distribution and $p-$value

As was already mentioned, the first summand in equation (3.2) is a χ^2-value. If the constraints are sharply satisfied ($\vec{H}(\vec{\alpha}) = \vec{0}$), only this first summand remains.

$$L = \chi^2 = (\vec{\alpha} - \vec{\alpha}_0)^T \mathbf{V}_{\vec{\alpha}_0}^{-1} (\vec{\alpha} - \vec{\alpha}_0) \quad \text{for } \vec{H}(\vec{\alpha}) = \vec{0} \tag{3.17}$$

After applying the kinematic refit, the χ^2-value can be calculated and is always positive. Furthermore, if the input in $\mathbf{V}_{\vec{\alpha}_0}$ is correct, the χ^2-values of all refitted events should obey the following probability density function (p.d.f) [Frü00].

$$f_r(\chi^2) = \frac{1}{2^{r/2}\Gamma(r/2)} (\chi^2)^{r/2-1} e^{-\chi^2/2} \tag{3.18}$$

r is the number of degrees of freedom (ndf) and Γ is the well known Gamma$-$function. The number of degrees of freedom r is exactly the number of constraints, which are used in the kinematic refit procedure. It is intuitively clear that by applying a refit with two constraints, the parameters $\vec{\alpha}$ have to be shifted further away from $\vec{\alpha}_0$ as by applying the refit with only one constraint. Therefore the χ^2-values will always be larger.

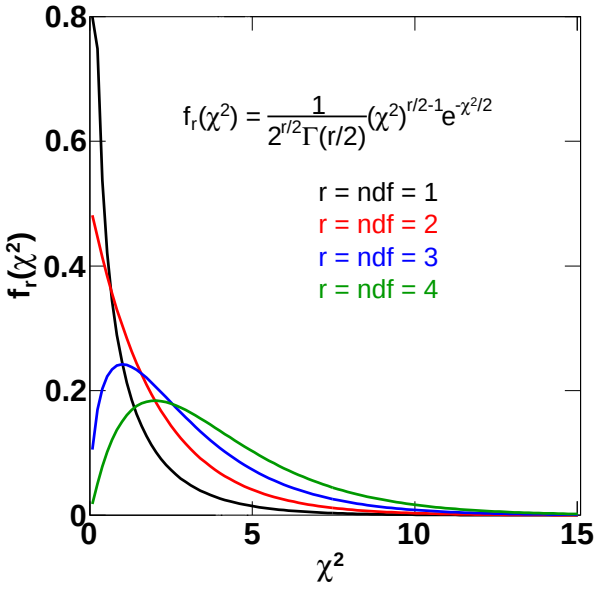

Figure 3.6: Normalized χ^2-distributions for different ndf.

The functions $f_r(\chi^2)$ are shown in figure 3.6. Their mean value, $\langle f_r(\chi^2) \rangle$, is equal to r [Frü00].
It is also possible to quantify the level of agreement between the obtained χ^2-value and a hypothesis by calculating the so called $p-$value [Frü00][Gro08]. The hypothesis in this case is that the χ^2-distribution for the refitted data should obey equation (3.18). The $p-$value is then defined as:

$$p - \text{value} = \int_{\chi^2_{re}}^{\infty} f_r(\chi^2) d\chi^2 \tag{3.19}$$

where χ^2_{re} is the calculated χ^2-value after the application of the refit. A high χ^2_{re} means that the parameters $\vec{\alpha}$ were shifted far away from $\vec{\alpha}_0$, which is undesirable, and this goes hand in hand with a low $p-$value. Altogether the $p-$value is the probability of obtaining other χ^2-values, which are at least as incompatible with the assumed hypothesis as the calculated χ^2_{re} [Gro08]. If the assumed hypothesis, and thus also the estimation of the errors in $\mathbf{V}_{\vec{\alpha}_0}$, is correct, the $p-$value should be equally distributed between 0 and 1.
These quality criteria are tested on the simulated data set, introduced in section 3.2.

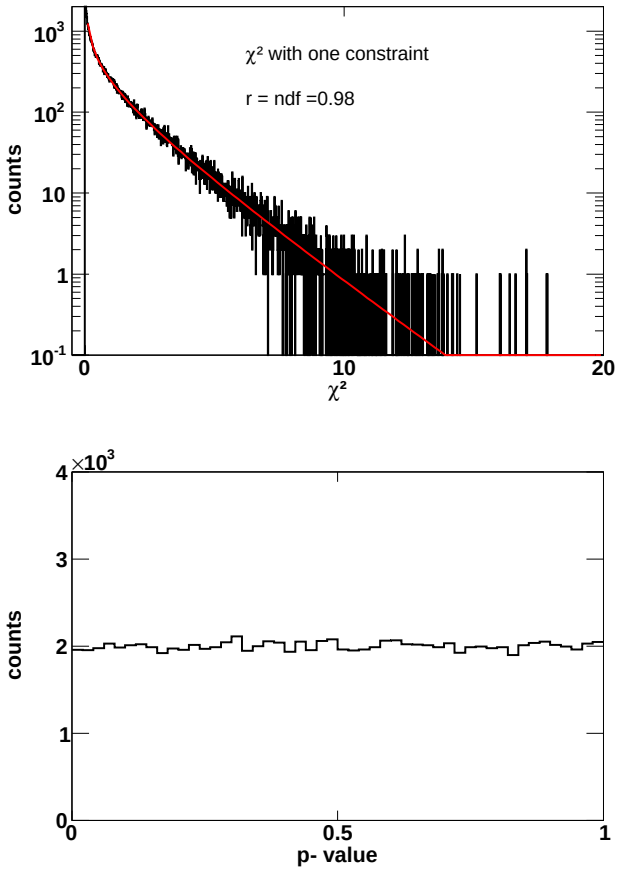

Figure 3.7: χ^2-distribution (top) and appropriate $p-$value distribution (bottom) for the kinematic refit with one constraint. The red line is the obtained fit result by using the function (3.18) with the free fit parameter $r = ndf$.

Figure 3.7 (top panel) shows the χ^2 results for the refit with one constraint. The fit value $r = ndf$ is compatible with one. This is the expected value, since the errors in $\mathbf{V}_{\vec{\alpha}_0}$ are not estimated but known. One should mention that the shown distribution is not normalized in contrast to equation (3.18). This, however, has no further consequences. Furthermore, the $p-$value distribution is flat (figure 3.7, bottom panel).
The same is valid for the refit with two constraints, only the fit value $r = ndf$ must be compatible with two.

3.3.2 Pull−distributions

A further possibility to check the estimated errors are the so called Pull−values [Rus06] [Frü00]. They are defined for each parameter in $\vec{\alpha}$ separately and are calculated in the following way:

$$\text{Pull-value}_i = \frac{\alpha_{0,i} - \alpha_i}{\sqrt{\sigma^2_{\alpha_{0,i}} - \sigma^2_{\alpha_i}}}, \tag{3.20}$$

where α_i and $\alpha_{0,i}$ are the $i-$th parameters in $\vec{\alpha}$ and $\vec{\alpha}_0$. $\sigma^2_{\alpha_i}$ and $\sigma^2_{\alpha_{i,0}}$ are the $i-$th diagonal elements in $\mathbf{V}_{\vec{\alpha}}$ and $\mathbf{V}_{\vec{\alpha}_0}$. As it was mentioned in section 3.1, the diagonal elements in $\mathbf{V}_{\vec{\alpha}}$ are always lower than the ones in $\mathbf{V}_{\vec{\alpha}_0}$. Therefore the Pull−values are real. If the covariance matrix for $\vec{\alpha}_0$ was estimated correctly, the Pull−value for each of the $3n$ parameters should be distributed Gaussian with a width of $\sigma \equiv 1$ and should be centered at 0. The results for the simulated data set is shown in figure 3.8, where only four of the total 12 parameters are plotted and the refit with one constraint was used.

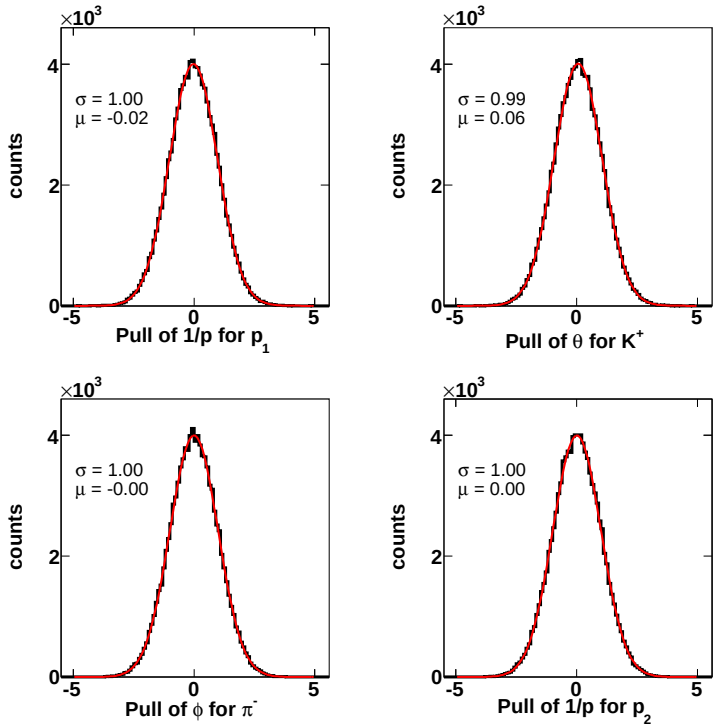

Figure 3.8: Pull−distributions for four of totally 12 parameters from the simulations of reaction (3.14). Only the case of the one constraint refit is shown.

As expected, the width (σ) and the mean value (μ) are compatible with the required values. The same is valid for the refit with two constraints, which is not explicitly shown here.

3.3.3 Wrong estimation of the covariance matrix

In an experiment the uncertainties are often unknown. One can then use the $p-$value distribution or equivalently the χ^2-distribution and also the Pull$-$distributions to optimize the estimated errors. Figure 3.9 (top panel) shows the result for the $p-$values for the one constraint refit, when the error of $1/p$ is estimated as 3% compared to the true value of 2.5%.

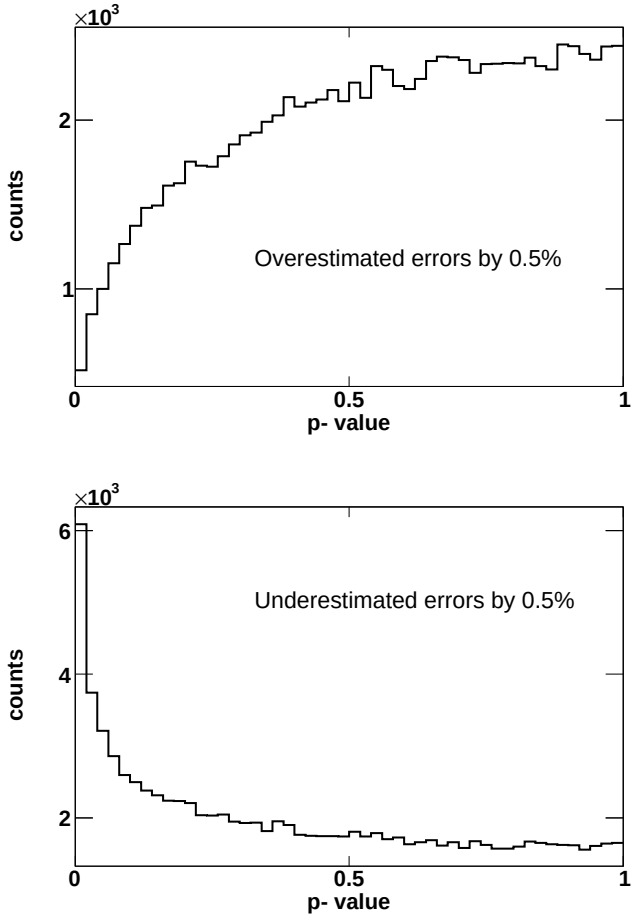

Figure 3.9: p$-$values for the kinematic refit with one constraint. Top: overestimation of errors ($\sigma(1/p) = 3\%$). Bottom: underestimation of errors ($\sigma(1/p) = 2\%$).

As a consequence of this overestimation, the χ^2-values get obviously to low. This results in high $p-$values. One can say that the refit works 'too well', because the assumed error band allows the parameters $\vec{\alpha}$ to be shifted further away from $\vec{\alpha}_0$ than it is necessary. The effect for the Pull$-$distributions is a reduction in the width, so that $\sigma < 1.0$. This is also valid for the Pull$-$distributions of ϑ and φ, although only $\sigma(1/p)$ is wrong. Figure 3.10 illustrates the consequence of the overestimation for the $MM(p_1,K^+,\pi^-)$ and $MM(p_1,K^+)$. A change in the line shapes is not visible, so that a slightly wrong matrix $\mathbf{V}_{\vec{\alpha}_0}$ does not effect the mass resolution at all. The mentioned effects are very similar for the refit with

two constraints, thus this is again not explicitly shown here.
Underestimating the errors (2% error for $1/p$) results in the $p-$value distribution in figure 3.9 (bottom panel). In this case the χ^2-values are too large, and thus the $p-$values are shifted to low values. The Pull$-$distribution will therefore be broadened ($\sigma > 1.0$). The effect on the lineshapes of Σ^+ and $\Lambda(1405)$ is again negligible. If the true uncertainties of $\vec{\alpha}_0$ are not Gaussian but include also systematics, the Pull$-$distributions will be shifted systematically to lower or higher $\mu-$values. Furthermore they will not be totally Gaussian anymore, but deformed.
Optimizing the matrix $\mathbf{V}_{\vec{\alpha}_0}$ for experimental data is anyway very difficult. The outer-diagonal elements, which might be different to 0 in the experiment, were not taken into account at all by now. If they are ignored, the Pull$-$distributions and also the $p-$value distribution will never have the totally correct form. But as was shown before, the effect on the line shapes of reconstructed particles is low, if the errors are slightly wrong. This is crucial for the analysis of the $\Lambda(1405)$ with HADES. Although the errors have to be estimated, one can be sure that the refit reproduces the line shape correctly.
Nevertheless one should try to optimize at least the diagonal elements.

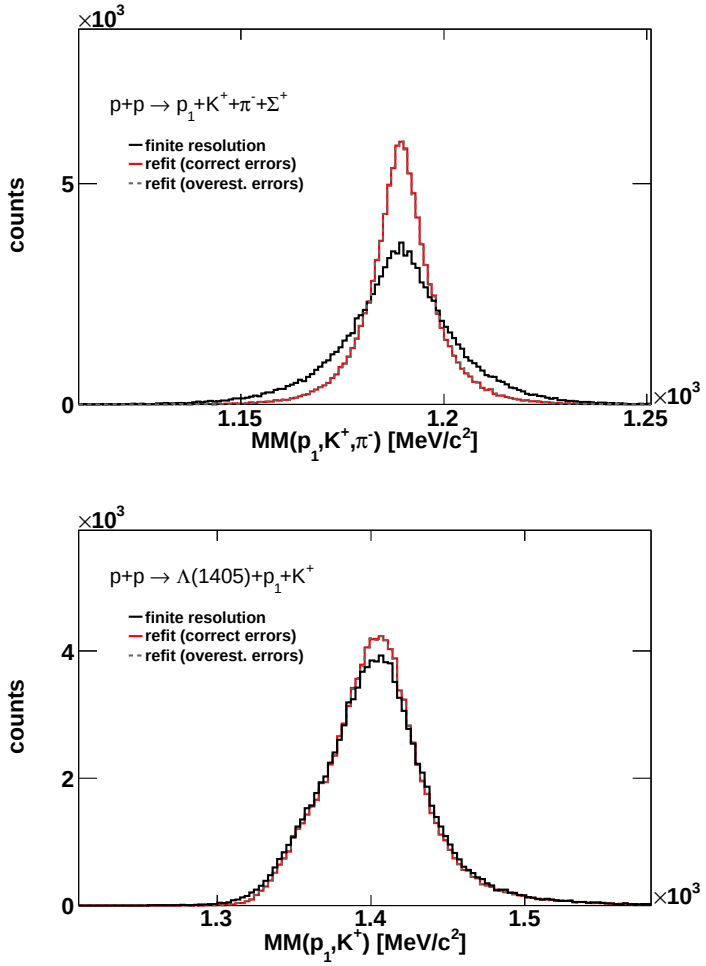

Figure 3.10: Consequences of overestimated errors ($\sigma(1/p) = 3\%$) for the mass resolution of Σ^+ (top) and $\Lambda(1405)$ (bottom).

3.3.4 Consequences of background

By now it was assumed that all investigated events initially satisfied the constraint conditions, as it is valid in the simulations. In an experiment this is never the case. There will always be a certain fraction of background, which can for example be due to misidentification of particles. Even if one estimates the matrix $\mathbf{V}_{\vec{\alpha}_0}$ perfectly, which is hardly possible, the quality quantities do not exactly behave as required. Concerning again the simulated reaction (3.14), one can imagine that there might be background below the π^0 peak in figure 3.2. This background will in general not peak at 134.9 MeV/c^2, but will be more or less distributed flat over a broad area. It is unavoidable to refit this background as well. The refitted background produces an increased amount of large χ^2 values. Thus the $p-$value distribution will peak at low values, similar to the distribution in figure 3.9 (bottom panel). The Pull−distributions, however, will be exaggerated at the left and right tail, and therefore will not be totally Gaussian anymore.
By cutting on $p-$values larger than a minimum value (e.g. $p-$value > 0.05), one can reduce the background. Therefore it is important that the covariance matrix $\mathbf{V}_{\vec{\alpha}_0}$ is determined as precise as possible. If one overestimates the errors, also the background events will in general be shifted to larger $p-$values, and the efficiency of the cut is reduced. If on the other hand the errors are underestimated, also the true π^0 events will be shifted to low $p-$values, and the cut will exclude a lot of signal.

3.4 Application of the kinematic refit to experimental data - the η and ω resonances

Finally the kinematic refit is tested on experimental data. Therefore a well known reaction is investigated [Rus06][Tei09]:

$$\begin{aligned} p + p &\rightarrow \eta/\omega + p_1 + p_2 \\ &\hookrightarrow \pi^- + \pi^+ + \pi^0 \end{aligned} \tag{3.21}$$

Events with four charged particles in the HADES acceptance were selected. The protons and pions are identified only via their energy loss in the MDCs and their momentum information.
Reaction (3.21) includes one undetectable neutral particle, the π^0. Therefore it is possible to make use of the kinematic refit. The appropriate constraint condition in this case is:

$$H_1 = MM(p_1,p_2,\pi^+,\pi^-) - M(\pi^0) = 0 \tag{3.22}$$

The missing mass of the four charged particles for the collected data sample is shown in figure 3.11. Before applying the kinematic refit, one obtains the black histogram. It shows a clear peak around 134.9 MeV/c^2. Furthermore there is obviously a large amount of background below this peak. To increase the signal to background ratio, only events in the mass region between 75 MeV/c^2 and 250 MeV/c^2 were chosen for the further analysis (two red dashed vertical lines in figure 3.11).

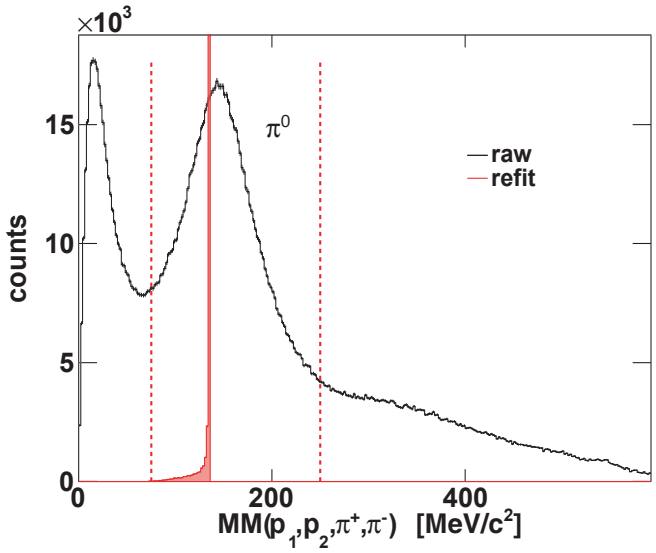

Figure 3.11: Missing mass of all charged particles before and after the kinematic refit. The horizontal vertical lines indicate the chosen mass area for the further analysis.

The kinematic refit is also only applied on these events and the following input is used:

- $(1/p,\vartheta,\varphi)$ is chosen as the parameter set for each particle.
- with help of the Pull−distributions the errors were estimated to be 2.3% for the momentum p, and 0.046° for ϑ and φ. A correlations between the three parameters was not taken into account, therefore $\mathbf{V}_{\vec{\alpha}_0}$ is diagonal.

This results in the red histogram in figure 3.11, where a very similar behavior to the one in the simulations is observed. Again a tail appears only on the left side of the peak.
The η and ω resonances can be reconstructed via the missing mass of the two protons.

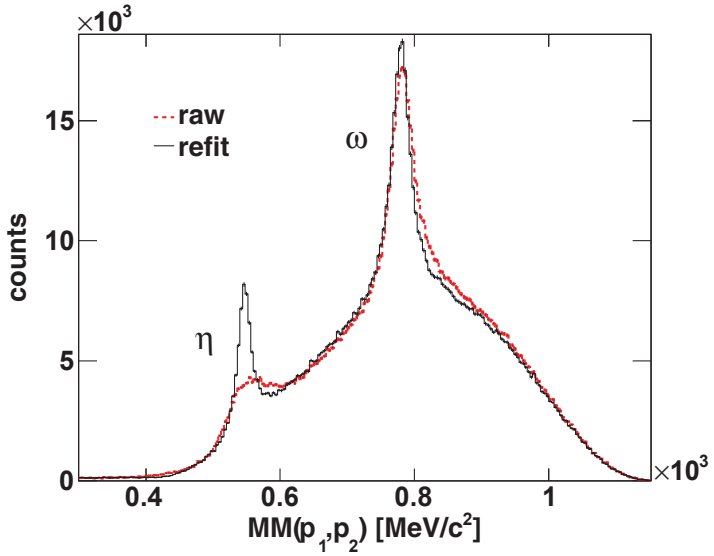

Figure 3.12: Missing mass of the two protons before and after the application of the kinematic refit.

The result is shown in figure 3.14. By plotting the missing mass (p_1,p_2) for the raw data set (without refit), one obtains the red dashed distribution. Here a clear ω signal on top of a wide spread background is visible. The η, however, is only indicated by a shoulder on the left tail of the distribution. The finite resolution broadens this signal in a way that it has nearly no significance. This changes remarkably, if the refitted parameters are used for the missing mass calculation. As it is shown in the black histogram, a clear η peak appears. The improvement for the ω is less impressive but also obvious. The differences in the effect of the refit for η and ω is due to the different $Q-$values of these reactions.
It is essential to notice that the shape of the background below the two resonances is quite similar for the red and black distributions. The refit does not shift this background and does not create any artificial peaks. It only improves the mass resolution, and therefore the resonances stick out of the broad background.
The next step is to focus on the $p-$value distribution in figure 3.13 (top panel).

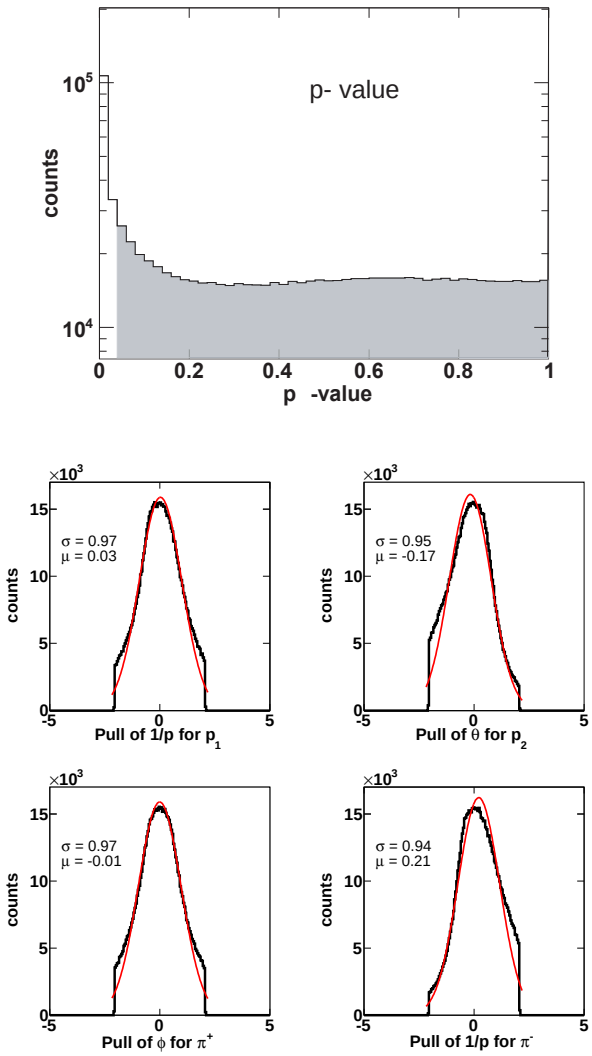

Figure 3.13: Top: $p-$value distribution of the refitted events. The gray shaded area is chosen for the further analysis. Bottom: Pull−distribution for four of totally 12 parameters. The red fits were applied between -2.0 and 2.0

The large amount of background, visible in figure 3.11, results in the peak structure at low $p-$values, like it was described in the last section. To partially get rid of that background, a cut on $p-$values larger than 0.04 is used (gray shaded area in figure 3.13, top panel). Furthermore, there is a small slope in the remaining distribution, which could be a hint that the errors in $\mathbf{V}_{\vec{\alpha}_0}$ are still slightly overestimated. This assumption is confirmed in the Pull−distributions in figure 3.13 (bottom panel). Again only four of the total 12 parameters are shown. The cut-off on the left and right tails is a consequence of the cut on the $p-$values. The remaining distributions are slightly too narrow. Altogether some of them do not look Gaussian at all, but are asymmetric. The reason for that could be on the one hand that the uncertainties of the measurement are not Gaussian, but include systematics. As was already mentioned, systematic errors lead to a shift in the mean value (μ) and also to an asymmetric behavior. On the other hand, there is still this large amount of background, which can not be totally excluded by the $p-$value cut. Since this background distribution below the π^0 peak in figure 3.11 has a slope, the refit has to shift more events to high values of $MM(p_1,p_2,\pi^+,\pi^-)$ as to low values. This asymmetry could create the asymmetry in the Pull−distributions.
Finally figure 3.14 (top panels) illustrate the $MM(p_1,p_2)$ after the cut on the $p-$value.

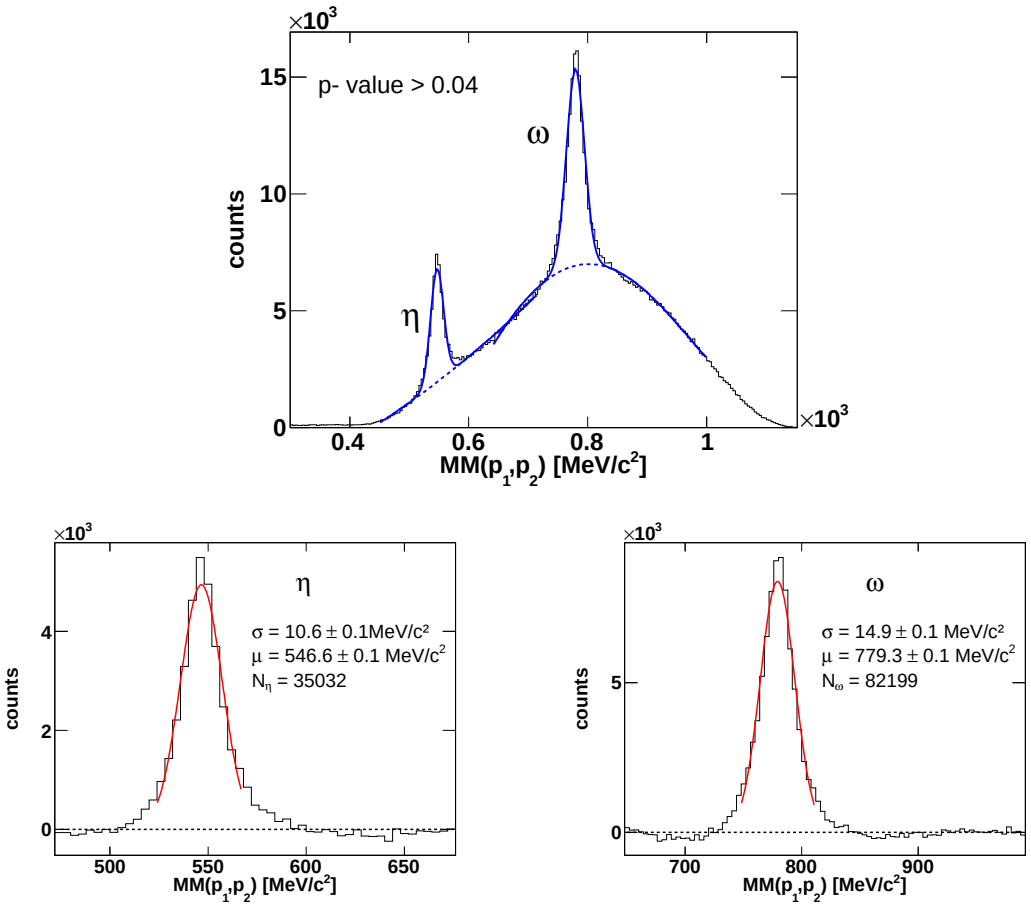

Figure 3.14: Top: $MM(p_1,p_2)$ for a cut on the $p-$value > 0.04. A Gaussian plus a polynomial is fitted to both resonances separately (solid blue lines). Bottom: The pure η and ω signals are fitted with a Gaussian from from 524.0 MeV/c^2 to 567.0 MeV/c^2 and from 748.0 MeV/c^2 to 811.0 MeV/c^2, respectively.

The resonances are fitted with a Gaussian plus a polynomial function. In order to obtain a pure ω or η (figure 3.14, bottom panel), the polynomials were subtracted. The resulting pole masses are in both cases slightly lower than the nominal ones ($M_\omega = 782.65$ MeV/c^2 and $M_\eta = 547.85$ MeV/c^2). The overall effect of the $p-$value cut is an improvement in the signal to background ratio (table 3.1). The listed results are obtained by integrating inside a 3.5σ area around the ω or η resonance, respectively.

Resonances	ω	η
Signal ($p-$value >0.00)[counts]	89588	38277
Signal ($p-$value >0.04)[counts]	82199	35032
Background ($p-$value >0.00)[counts]	213500	44796
Background ($p-$value >0.04)[counts]	177095	34296
S/B ($p-$value >0.00)	0.42	0.85
S/B ($p-$value >0.04)	0.46	1.02

Table 3.1: Statistics of the ω and η reconstruction. Compared are the results for no $p-$value cut ($p-$value >0.00) and a cut on $p-$value > 0.04. The results are obtained by an integration in the 3.5σ area around the pole masses.

Of course the applied cut reduces also some of the signal, but the reduction of background is much higher.
Altogether the kinematic refit is crucial for the analysis of η and ω. Without its ability to improve the mass resolution, the η could be hardly separated from the background. Furthermore the $p-$value provides another powerful alternative to identify and reduce background.

4 Analysis of the $\Lambda(1405)$

This chapter describes in detail the analysis of the $\Lambda(1405)$ resonance in the charged ($\Sigma\pi$) decay channels. The first part introduces some general aspects, concerning the $\Lambda(1405)$ event characteristics. Afterwards the different steps in the analysis of the experimental data are presented and the results are compared to the simulations. The third part focuses on the modeling and understanding of the background, which in the end has to be subtracted to get a pure $\Lambda(1405)$ signal. The chapter is completed with a discussion about the obtained results.

4.1 The $\Lambda(1405)$ in proton-proton reactions

4.1.1 General considerations

The $\Lambda(1405)$ can be produced in proton-proton reactions (with a threshold of 2.41 GeV kinetic beam energy) and decays into two charged ($\Sigma^{\pm}\pi^{\mp}$), and one neutral channel ($\Sigma^0\pi^0$). In principal, the $\Lambda(1405)$ can be produced in different ways, e.g. together with a K^0 or a K^+ and the appropriate amount of other particles in order to conserve charge neutrality and baryon number. The reaction with the highest cross section for a kinetic beam energy of 3.5 GeV and the only one of interest in this work reads as follows:

$$p + p \xrightarrow{3.5GeV} \Lambda(1405) + K^+ + p \tag{4.1}$$

$$\Lambda(1405) \rightarrow \Sigma^- + \pi^+$$

$$\Sigma^- + \pi^+ \rightarrow n + \pi^- \quad 33.33\% \tag{4.2}$$

$$\Lambda(1405) \rightarrow \Sigma^+ + \pi^-$$

$$\Sigma^+ + \pi^- \rightarrow p + \pi^0 \quad 17.19\% \tag{4.3}$$

$$\Sigma^+ + \pi^- \rightarrow n + \pi^+ \quad 16.11\% \tag{4.4}$$

$$\Lambda(1405) \rightarrow \Sigma^0 + \pi^0$$

$$\Sigma^0 + \pi^0 \rightarrow \Lambda + \gamma$$

$$\Lambda + \gamma \rightarrow p + \pi^- \quad 21.35\% \tag{4.5}$$

$$\Lambda + \gamma \rightarrow n + \pi^0 \quad 12.02\% \tag{4.6}$$

The resonance can be reconstructed via the missing mass of the primary proton and the K^+ ($MM(p,K^+)$). In addition, all channels except channel (4.6) provide the possibility to detect further charged particles and thus to do an exclusive analysis. This work attends only to the investigation of the two charged decay channels (4.2) and (4.4), which have both the same final state products (p,K^+,π^-,π^+,n). The reaction (4.3) has two protons in the final state, which makes the analysis difficult, as the HADES acceptance reduces the

statistics of this channel remarkably compared to the reactions (4.2) and (4.4). Due to the kinematics it is very probable that a least one of the two protons is boosted in the forward direction, where it can at best be detected with the Forward Wall (see outlook) [Sch09]. The investigation of the neutral channel (4.5) is extensively discussed in [Epp09].
One characteristic feature in the analysis of the $\Lambda(1405)$ is that this resonance is not isolated in its mass region, since the resonance $\Sigma(1385)^0$ with a width of $\Gamma \approx 36$ MeV/c^2 [Gro08] lies nearby. As can be seen in the reaction below, the production mechanism is the same as for the $\Lambda(1405)$.

$$
\begin{array}{lll}
p + p \xrightarrow{3.5GeV} \Sigma(1385)^0 + K^+ + p & & \\
\quad \hookrightarrow \Sigma^- + \pi^+ & & \\
\quad\quad \hookrightarrow n + \pi^- & 5.85\% & (4.7) \\
\quad \hookrightarrow \Sigma^+ + \pi^- & & \\
\quad\quad \hookrightarrow p + \pi^0 & 3.02\% & (4.8) \\
\quad\quad \hookrightarrow n + \pi^+ & 2.83\% & (4.9) \\
\quad \hookrightarrow \Lambda + \gamma & & \\
\quad\quad \hookrightarrow p + \pi^- & 0.83\% & (4.10) \\
\quad\quad \hookrightarrow n + \pi^0 & 0.47\% & (4.11) \\
\quad \hookrightarrow \Lambda + \pi^0 & & \\
\quad\quad \hookrightarrow p + \pi^- & 55.59\% & (4.12) \\
\quad\quad \hookrightarrow n + \pi^0 & 31.15\% & (4.13)
\end{array}
$$

A difference in the decay channels appears only for the neutral channels. Here the $\Sigma(1385)^0$ can not decay into a $(\Sigma^0\pi^0)$ state, due to isospin conservation. Hence this is the only channel, where the $\Lambda(1405)$ and the $\Sigma(1385)^0$ can be separated explicitly [Epp09] [Zyc08]. Unfortunately the charged decay channels behave identically and can therefore not be distinguished. However the branching ratio in the charged channels is much lower for the $\Sigma(1385)^0$ as for the $\Lambda(1405)$, and this minimizes the contamination of $\Sigma(1385)^0$ in the overlapping missing mass spectrum. As a pure $\Lambda(1405)$ signal can only be obtained by subtracting the $\Sigma(1385)^0$ spectrum, the low contamination is crucial in order to keep the systematic errors as small as possible.
The principle steps of the exclusive charged channel analysis are the following and are explained in detail in the following sections:

1. Four charged particles (p,K^+,π^+ and π^-) have to be detected and identified.

2. The neutron can not be measured directly with the HADES spectrometer, but it can be reconstructed via the missing mass of the four detected particles. By applying a mass cut around the nominal neutron mass, events with a neutron in the final state can be separated, and only these events are used for further investigations.

3. The intermediate Σ^+ and Σ^- resonances are reconstructed via the missing mass (p,K^+,π^-) or (p,K^+,π^+), respectively. In order to extract both resonances, again

a cut on these missing masses is used. The obtained data set should include the $\Lambda(1405)$ and also the $\Sigma(1385)^0$ events.

4. Finally the missing mass (p,K^+) is investigated, where it is expected to see the signal of the $\Lambda(1405)$, which is extracted by a subsequent subtraction of the remaining background.

Additionally, all other reactions, containing a K^+ in the final state, should be taken into account within this analysis. They are listed in table 4.1.

Nr.	*Production reaction p+p →*	*cross section in mb*
1.	$K^+ + p + \Lambda$	0.04845
2.	$K^+ + p + \Lambda(1405)$	0.021
3.	$K^+ + n + \Sigma^+$	0.04196
4.	$K^+ + n + \Lambda + \pi^+$	0.0239446
5.	$K^+ + p + \Sigma^0$	0.020175
6.	$K^+ + p + \Lambda + \pi^0$	0.018915
7.	$K^+ + p + \Sigma^- + \pi^+$	0.0113212
8.	$K^+ + p + \Sigma^+ + \pi^-$	0.00927646
9.	$K^+ + n + \Sigma^+ + \pi^- + \pi^+$	0.00851732
10.	$K^+ + p + n + K^0_S$	0.00757802
11.	$K^+ + p + \Sigma(1385)^0$	0.0068
12.	$K^+ + p + \Lambda(1520)$	0.004 ??
13.	$K^+ + p + \Sigma^- + \pi^+ + \pi^0$	0.00649418
14.	$K^+ + p + \Sigma^+ + \pi^- + \pi^0$	0.00526669
15.	$K^+ + p + \Sigma^0 + \pi^+ + \pi^-$	0.00524109
16.	$K^+ + p + \Lambda + \pi^+ + \pi^- + \pi^0$	0.00503324
17.	$K^+ + n + \Sigma(1385)^+$	0.0078
18.	$K^+ + n + \Lambda + \pi^+ + \pi^- + \pi^+$	0.00296014
19.	$K^+ + p + \Lambda + \pi^+ + \pi^-$	0.0026386
20.	$K^+ + n + \Sigma^- + \pi^+ + \pi^+$	0.00193032
21.	$K^+ + p + p + K^-$	0.00132
22.	$K^+ + p + p + \pi^- + K^0_S$	0.00176164

Table 4.1: channels with a K^+ in the final state for $p + p$ reactions at 3.5 GeV kinetic beam energy.

Getting the cross sections for these channels is difficult, since measurements for $p + p$ reactions in our energy range (3.5 GeV) are rather limited. However, one can use measured cross sections from other energy ranges, found in the literature. By fitting these values with a phase space distribution, it is possible to extract the appropriate cross section for 3.5 GeV kinetic energy. This procedure is described in detail in [Epp09]. Only for channel 12 it was not possible to get any cross sections. Therefore the shown value is just a rough estimation by taking into account the cross sections of $\Lambda(1405)$ and $\Sigma(1385)^0$. This is sufficient for the

later analysis, as it will become clear in the next sections. Besides reaction 11, especially reaction 4, 7, 8, 10, 12 and 17 are of high importance for the further analysis, since they provide exactly the same particles in the final state as the $\Lambda(1405)$. The reactions are listed in more detail in the equations (4.14)-(4.20), and only the decay channels of interest are specified.

$$p + p \xrightarrow{3.5GeV} \Lambda + K^+ + n + \pi^+$$
$$\hookrightarrow p + \pi^- \qquad 63.9\% \tag{4.14}$$

$$p + p \xrightarrow{3.5GeV} \Sigma^- + p + K^+ + \pi^+$$
$$\hookrightarrow n + \pi^- \qquad 100\% \tag{4.15}$$

$$p + p \xrightarrow{3.5GeV} \Sigma^+ + p + K^+ + \pi^-$$
$$\hookrightarrow n + \pi^+ \qquad 48.31\% \tag{4.16}$$

$$p + p \xrightarrow{3.5GeV} K^0_S + p + K^+ + n$$
$$\hookrightarrow \pi^+ + \pi^- \qquad 69.2\% \tag{4.17}$$

$$p + p \xrightarrow{3.5GeV} \Lambda(1520) + p + K^+$$
$$\hookrightarrow \Sigma^+ + \pi^-$$
$$\hookrightarrow n + \pi^+ \qquad 6.76\% \tag{4.18}$$
$$\hookrightarrow \Sigma^- + \pi^+$$
$$\hookrightarrow n + \pi^- \qquad 14.00\% \tag{4.19}$$

$$p + p \xrightarrow{3.5GeV} \Sigma(1385)^+ + n + K^+$$
$$\hookrightarrow \Lambda + \pi^+$$
$$\hookrightarrow p + \pi^- \qquad 56.33\% \tag{4.20}$$

4.1.2 Simulations

With the cross sections in table 4.1 it is possible to do simulations besides the analysis of experimental data. Simulations provide an overview, which channels contribute in the analysis and how they influence the final spectra.
The analysis of the real data and of the simulations were done simultaneously, and both analysis are in principle identical. Nevertheless, the investigation of the experimental data provides a couple of challenges, which are not present in the simulations. For instance, in the experimental data the misidentification of protons and pions as kaons is ways stronger than in the simulations. The reason for this is that only channels with a K^+ in the final state are simulated, whereas the kaon production in the experiment is suppressed by more than a factor 100 compared to the production of protons and pions. The next section will therefore show both, the results of the experiment and how they are compatible with the simulations.
Before starting the final analysis, all channels of table 4.1 are simulated separately with $20 \cdot 10^6$ events in PLUTO.
PLUTO is a Monte Carlo based event generator, which was in particular developed for HADES [Frö09]. With this tool, the particles of the reactions are generated as straight lines in the position space and energy and momentum conservation is fulfilled for each event. The so obtained track informations serve as an input for the HGeant simulations, where the interaction of the particles with the detector materials as well as the curvature of the particle tracks in the magnetic field is followed. The simulated detector hit points are used to produce simDSTs. For that purpose the answer of each detector to the particle hit is modeled via a digitization procedure, which includes noise, inefficiencies and the finite resolution. These signals are then treated exactly like the experimental data. More detailed information about the simulation procedure can be found in [HGe08][Gea95].
After scaling each channel with the appropriate cross section of table 4.1, the final analysis can be carried out.

4.2 Investigation of the $\Lambda(1405)$

The following section describes all steps in the analysis of the experimental data, which are necessary in order to separate the $\Lambda(1405)$ into the two charged channels. Special efforts were done to optimize the background suppression, which contaminates the $\Lambda(1405)$ signal. This is an essential point, since the remaining background has to be subtracted in order to get a pure $\Lambda(1405)$ and this is only possible if the background contamination is low. At the end of each subsection a comparison to the simulation will help to interpret the experimental results.

4.2.1 K^+ identification

The first step in the analysis of the $\Lambda(1405)$ is the identification of the appropriate set of hadrons (p,K^+,π^+,π^-). In general, this is done by the combined measurement of the time-of-flight and the momentum of the particles. With this the particle mass can be determined, which makes an identification possible. However, as described in chapter 2, a time-of-flight measurement was not possible for the $p+p$ beam time, since the start detector was missing. Therefore the particle identification is primary done via the energy loss of the particles in the detector system of HADES. Figure 4.1 shows the dE/dx vs. momentum distribution of all positive particles for events with at least four detected charged particles. The upper picture illustrates the results for the MDC chambers, the lower one for tracks in the TOFino detector. The adapted Bethe-Bloch curves for protons, K^+ and π^+ are indicated by the solid black lines, and act as an orientation [Sch08]. Clearly visible are maxima in the distributions due to pions and protons around the theoretical curves. Kaons, however, are not visible at all. On the one hand, in this energy range kaons are highly suppressed in the production compared to protons and pions [Epp09]. On the other hand the dE/dx resolution of the MDCs and of the time-of-flight detectors is anyway not good enough to clearly separate the different distributions. Therefore protons and pions overlap to the kaons from both sides. Especially in the high momentum region ($>$ 600 MeV/c) even the distributions of protons and pions are not clearly distinguished anymore, and thus the kaons in this area are hard to extract. Nevertheless, a rough particle identification can be done with help of these dE/dx vs. momentum distributions. For that purpose two dimensional graphical cuts are used. Figure 4.1 (top) shows the cuts, which were applied for the identification of protons (magenta-dashed) and pions (red-dashed). If a detected particle provides a measured point inside one of these cuts, it is identified as a proton or a pion, respectively. Protons and pions are indeed only identified via these MDC dE/dx cuts.

However, finding an appropriate cut for the kaons is more challenging. The used method is optimized for the analysis of the $\Lambda(1405)$ in the charged channels (4.2) and (4.4).

The main idea is to find a data sample with a very high K^+ purity and efficiency. The $dE/dx-$cuts can then be tuned on the dE/dx vs. momentum distribution of the so obtained kaon candidates.

First of all events are selected with exactly four charged particles (p,K^+,π^+,π^-). A particle is in a first step of iteration identified as a K^+, if it corresponds to a measured point (dE/dx vs. momentum) inside the broad blue dashed cut for the MDCs and also inside the one for the TOFino (see figure 4.1). It is necessary that it lies within both cuts, since this increases the purity of the kaon identification.

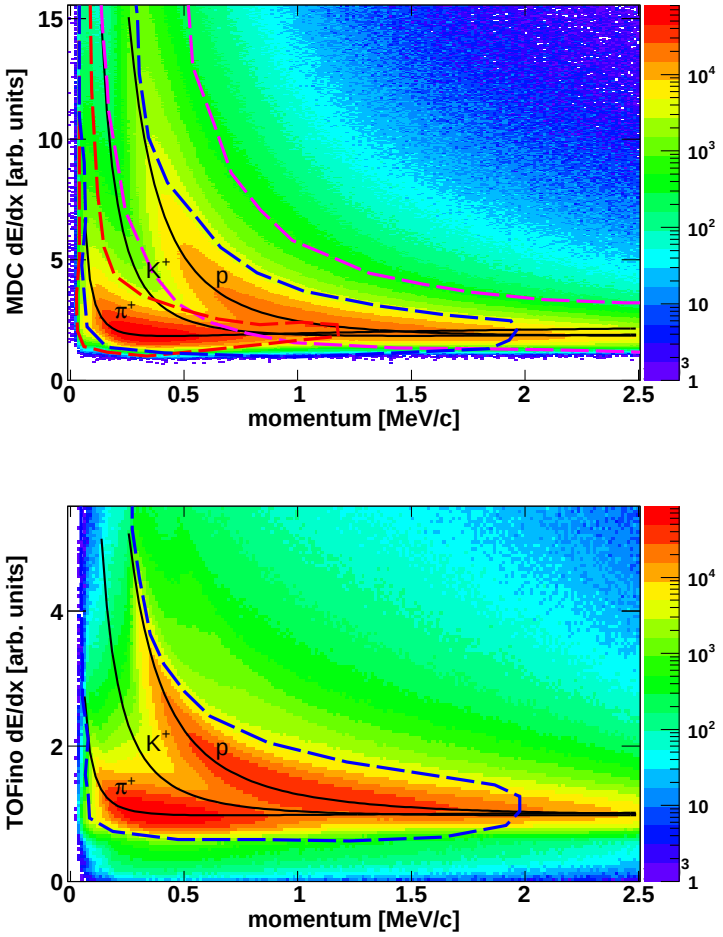

Figure 4.1: dE/dx vs. momentum for all detected particles in MDCs (top) and TOFino (bottom) [Pre09]. Modified Bethe-Bloch curves are indicated by the solid black lines. The MDC cuts for protons and pions are shown in the magenta dashed line and the red dashed line, respectively. The blue dashed lines are the broad kaon cuts for the MDCs and for TOFino.

In principal a kaon could also hit the TOF instead of the TOFino, but due to the kinematics, only a negligible amount of kaons ($\approx 1\%$) reaches such high polar angles. Therefore the kaon cut for the TOF was not tuned for this analysis.
The chosen MDC$-K^+$ and TOFino$-K^+$ cut can not provide a sample of very pure kaons, since the contamination due to pions and protons is rather high. On the other hand, the efficiency of this selection is almost 100% and thus one can expect that most of the real kaons are in the obtained data sample.
The identification of the proton and the two pions allows to calculate the mass of the K^+ candidates, as it is described in chapter 2. By cutting on a certain mass range, the purity of the kaon candidates can be increased. Figure 4.2 shows the obtained mass distribution of all kaon candidates. No kaon signal appears in the nominal mass area around 500 MeV/c^2 due to the large contamination from the pion and proton signals. The missing start detector and the poor time resolution of TOFino result in a poor time-of-flight resolution. Therefore also the mass resolution is not sufficient to clearly separate the different particle species.

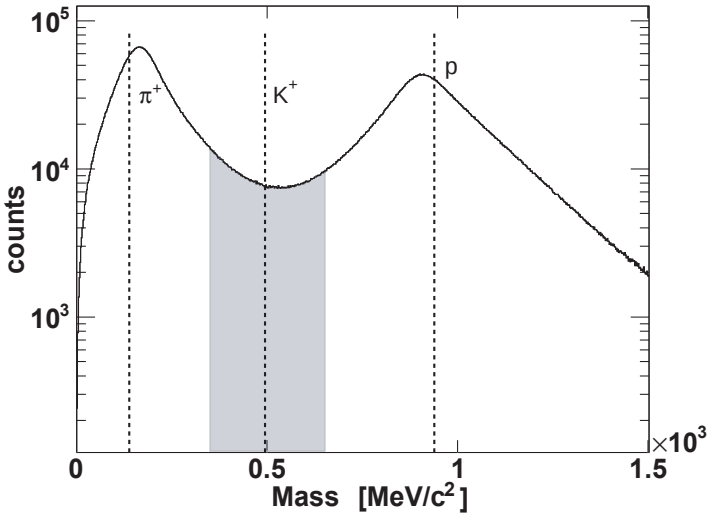

Figure 4.2: Calculated mass of all particles, which were identified as a K^+ by applying the dE/dx cuts in figure 4.1. The vertical dashed lines indicate the nominal masses of π^+, K^+ and protons. Events within the mass range 350 MeV/c^2 – 650 MeV/c^2 are selected for further investigations (gray shaded area).

In order to extract kaons, only the mass range from 350 MeV/c^2 to 650 MeV/c^2 (gray shaded area in figure 4.2), where the kaons are mainly expected, is used for further investigations.

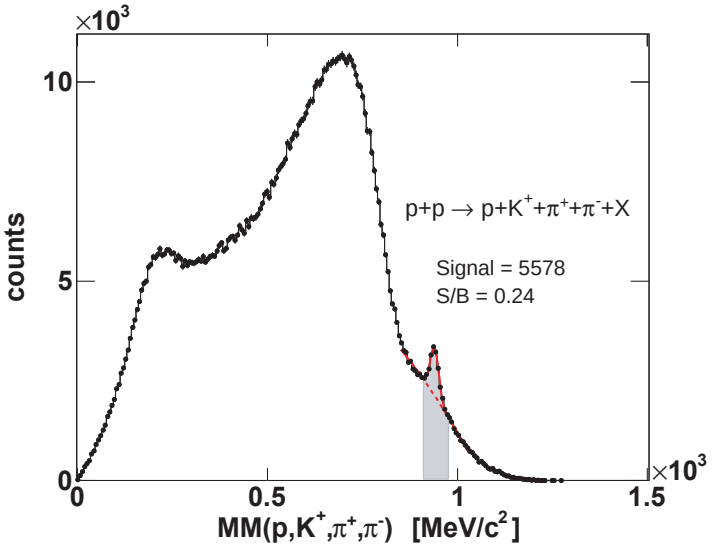

Figure 4.3: Missing mass (p,K^+,π^+,π^-), showing a missing neutron, after the cuts on the dE/dx vs. momentum distribution and on the the kaon mass. The gray shaded area (910 MeV/c^2 – 971 MeV/c^2) selects neutrons. The red line represents a Gaussian fit together with a polynomial fit. The signal to background ratio is determined by integrating inside the gray area.

Considering the charged decay channels of the $\Lambda(1405)$ or the $\Sigma(1385)^0$ and also the channels (4.14)-(4.20) it is expected that most of the selected events with a true K^+ should also have a neutron in the final state. In order to get this neutron, the missing mass (p,K^+,π^+,π^-) is plotted in figure 4.3. A clear neutron peak sticks out of a huge background ($S/B = 0.24$). This background is only due to misidentified pions and protons, as will be explained later. By cutting on the area from 909 MeV/c^2 to 971 MeV/c^2 (gray shaded area) neutron events are extracted and thus the kaon purity of the data sample is further increased. The cross sections in table 4.1 predict, however, that the main part of the filtered neutron events should include an intermediate Λ (see reaction (4.14) or (4.20)). These channels are of course not the ones, which have to be analyzed in order to get the $\Lambda(1405)$ signal. However, their investigation can supply a very pure sample of kaons, which is the goal of this subsection. The invariant mass (p,π^-) is shown in figure 4.4 (top panel).

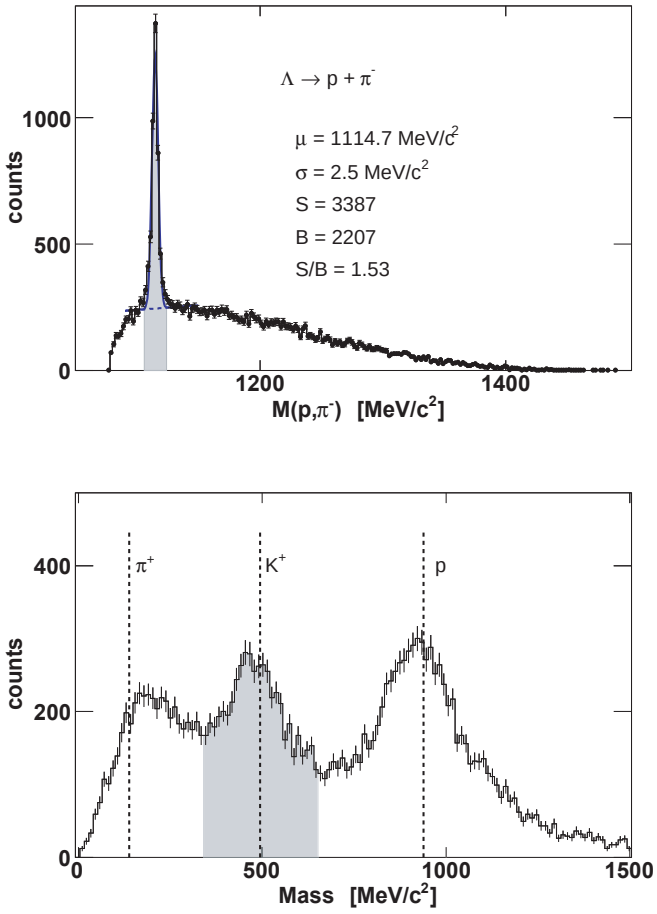

Figure 4.4: Top: Invariant mass (p,π^-), showing a Λ signal. The distribution is fitted with a Gaussian together with a polynomial (blue line). The gray shaded area around the Λ (1107 MeV/c^2−1122 MeV/c^2) is used to filter out K^+ candidates. Bottom: Mass of all K^+ candidates with a hit in TOF or TOFino after the cut on the intermediate Λ. The mass is calculated with the method described in chapter 2.

It provides a clear Λ signal, with a relatively low amount of background ($S/B = 1.53$). The Λ has a strangeness content of -1 and therefore it has to be produced together with a K^+ (or K^0) (strangeness content $+1$). Consequently cutting on the area from 1107 MeV/c^2 to 1122 MeV/c^2 (gray shaded area) supplies a data sample with a high contribution of true kaons. This is confirmed in figure 4.4 (bottom) where the mass of the so selected K^+ candidates is shown (of course without applying the cut on the K^+ mass before). The peak at around 494 MeV/c^2 proofs that a considerable part of the selected events between 350 MeV/c^2 and 650 MeV/c^2 is due to true K^+. The obtained sample can be used to optimize the $dE/dx - K^+$ cuts. For that purpose figure 4.5 shows the dE/dx vs. momentum distribution for the remaining kaon candidates. It is nicely centered around the modified Bethe-Bloch curves.
The goal, however, is not only to find $dE/dx - K^+$ cuts, which provides a high efficiency for the kaon identification, but also a high purity. Therefore figure 4.6 illustrates the dE/dx vs. momentum distribution for a complementary data set to the one in figure 4.5, where kaons were rejected. Thus mainly misidentified protons and pions remain. Table 4.2 summarizes the cuts, which were used to get the appropriate data samples for figure 4.5 and 4.6.

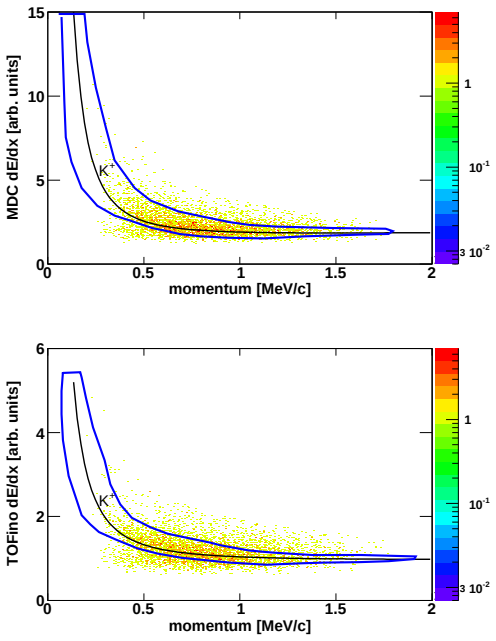

Figure 4.5: dE/dx vs. momentum for all K^+ candidates (top: MDC, bottom TOFino) after the selection cuts in table 4.2 (left column). The solid black lines indicate the modified Bethe-Bloch curve for kaons. The blue graphical cuts include most of the events.

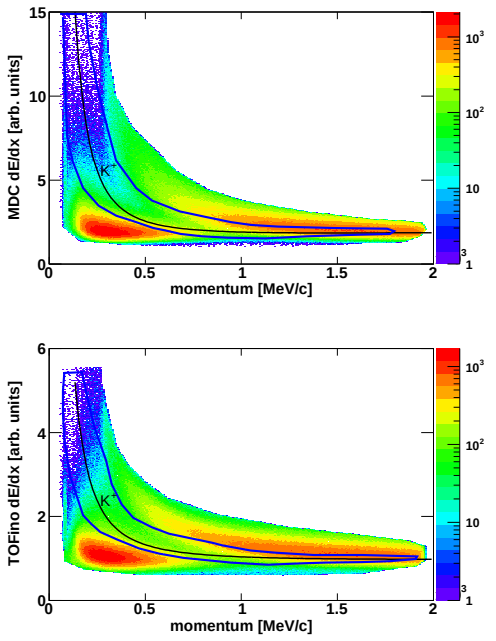

Figure 4.6: dE/dx vs. momentum for all K^+ candidates (top: MDC, bottom TOFino) after the rejection cuts in table 4.2 (right column). The solid black lines indicate the modified Bethe-Bloch curves for kaons. The blue graphical cuts exclude protons and pions.

Cut on:	*Kaon (figure (4.5))*	*Anti kaon (figure (4.6))*
K^+ mass	$350 < m_{K^+} < 650 MeV/c^2$	$m_{K^+} < 180 MeV/c^2$ or $m_{K^+} > 900 MeV/c^2$
neutron ($MM(p,K^+,\pi^+,\pi^-)$)	$910 < MM(p,K^+,\pi^+,\pi^-) < 971 MeV^/c^2$	$MM(p,K^+,\pi^+,\pi^-) < 910 MeV/c^2$ or $MM(p,K^+,\pi^+,\pi^-) > 971 MeV/c^2$
Λ ($M(p,\pi^-)$)	$1107 MeV/c^2 < M(p,\pi^-) < 1122 MeV/c^2$	–

Table 4.2: Cuts used to filter out K^+ (left column) or to reject K^+ (right column).

The blue dE/dx cuts are optimized to select kaons (figure 4.5) and at the same time they exclude the pions and protons effectively (figure 4.6). They are used to create a new data sample (p,K^+,π^+,π^-), which is afterwards filtered by applying the cut on the kaon mass (350 MeV/c^2 – 650 MeV/c^2), like it was done before. The so obtained data set is in the following referred to S_{K^+}. The effect of the optimized kaon cuts is illustrated in figure 4.7, where the missing mass (p,K^+,π^+,π^-) of all events in S_{K^+} is shown.

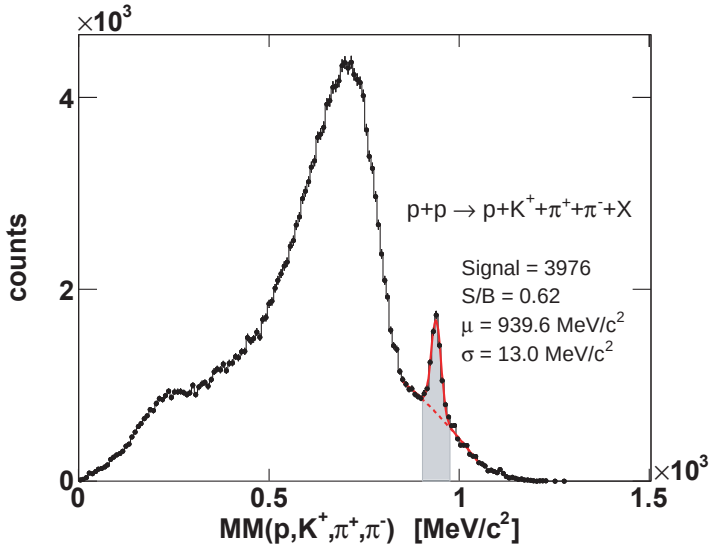

Figure 4.7: Missing mass (p,K^+,π^+,π^-) after the optimized cuts on the dE/dx vs. momentum distribution and on the kaon mass. The red fit is done with a Gaussian together with a polynomial. The signal to background ratio is determined by integrating inside the gray area. The range 909 MeV/c^2 to 971 MeV/c^2 (2.4σ) selects neutrons for the further analysis (gray shaded area).

The neutron signal is much clearer with a signal to background ratio improved by a factor of 2.6 compared to figure 4.3. It is, however, unavoidable that also some signal is lost (29%) due to the narrower cuts. The obtained dE/dx cuts were chosen after a comparison to totally 25 slightly broader and narrower cut combinations.

The ones, which are shown here, had the best signal to background ratio in the neutron peak together with a high efficiency.

It is possible to transform these cuts to appropriate cuts for simulated data [Epp09] and in this way the kaon identification can be applied to the simulations.
The simulated data set is treated in exactly the same way as the experimental data. Thus after selecting the appropriate set of hadrons by the adapted dE/dx cuts and after cutting on the kaon mass range (350 MeV/c^2 – 650 MeV/c^2), the missing mass of the four particles can be investigated. The result is shown in figure 4.8. A clear, almost background free neutron signal is visible. Since only channels were simulated with a K^+ in the final state (see table 4.1), almost no misidentification of pions and protons as kaons appears. This makes the comparison to figure 4.7 difficult. Nevertheless figure 4.8 is a very important result, since it shows that only the reactions of table 4.1, which have the final state (p,K^+,π^+,π^-,n), survive the analysis cuts, applied so far. Thus besides the $\Lambda(1405)$ and the $\Sigma(1385)^0$, the reactions (4.14)-(4.20) remain. As a consequence, the background in figure 4.7 is really only due to misidentification.

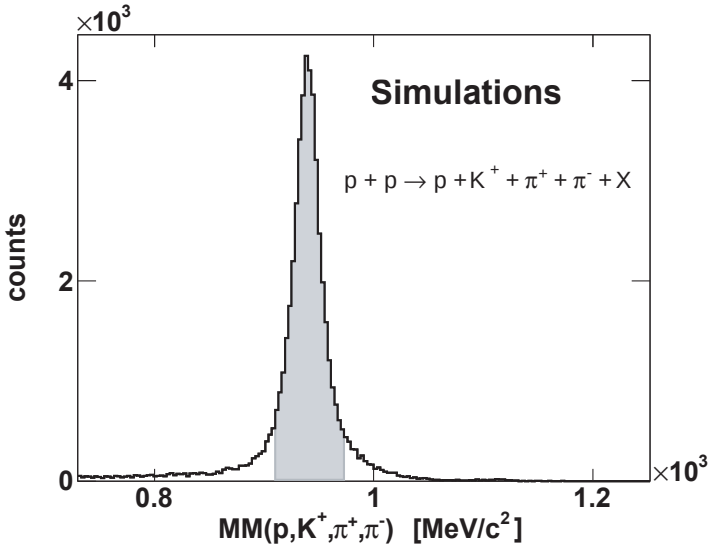

Figure 4.8: Missing mass of the four charged particles. Events in the mass area from 909 MeV/c^2 to 971 MeV/c^2 are chosen for the further analysis (gray shaded area). This cut is adapted to the experimental results.

4.2.2 Kinematic refit and track quality cuts

In order to separate the neutron resonance and thus to extract $\Lambda(1405)$ events, only events in the range 909 MeV/c^2 – 971 MeV/c^2 (gray shaded area of figure 4.7) are selected for the further analysis. They can be kinematically refitted with the constraint that the missing mass (p,K^+,π^+,π^-) is the nominal neutron mass. According to equation (3.2) the constraint H_1 reads as follows:

$$H_1 = MM(p,K^+,\pi^+,\pi^-) - M(n) = 0 \tag{4.21}$$

The covariance matrix $\mathbf{V}_{\vec{\alpha}_0}$ is determined by modifying only the diagonal elements until the Pull−distributions are almost Gaussian with a width of $\sigma \approx 1$ (see section 3.3). The final result is an uncertainty in the momentum of 3.5% and an uncertainty in ϑ and φ of 0.086° for each of the four particles, which is reasonable for HADES [Aga09c] [Mar10].
The next step in the analysis is to investigate the expected intermediate Σ^+ or Σ^- resonances, like they appear in the reactions (4.2) and (4.4). Before doing this, one can exclude two background sources from the remaining data set. The channels (4.14) and (4.20) with the intermediate Λ can be rejected by excluding all events with an invariant mass (p,π^-) within a range from 1107.2 MeV/c^2 to 1122.0 MeV/c^2 (see figure 4.9, top panel). Furthermore channel (4.17) can also be suppressed in the further analysis by cutting outside a mass range from 482.6 MeV/c^2 to 506.8 MeV/c^2 (see figure 4.9, bottom panel), getting rid in this way of the K^0_S contribution.

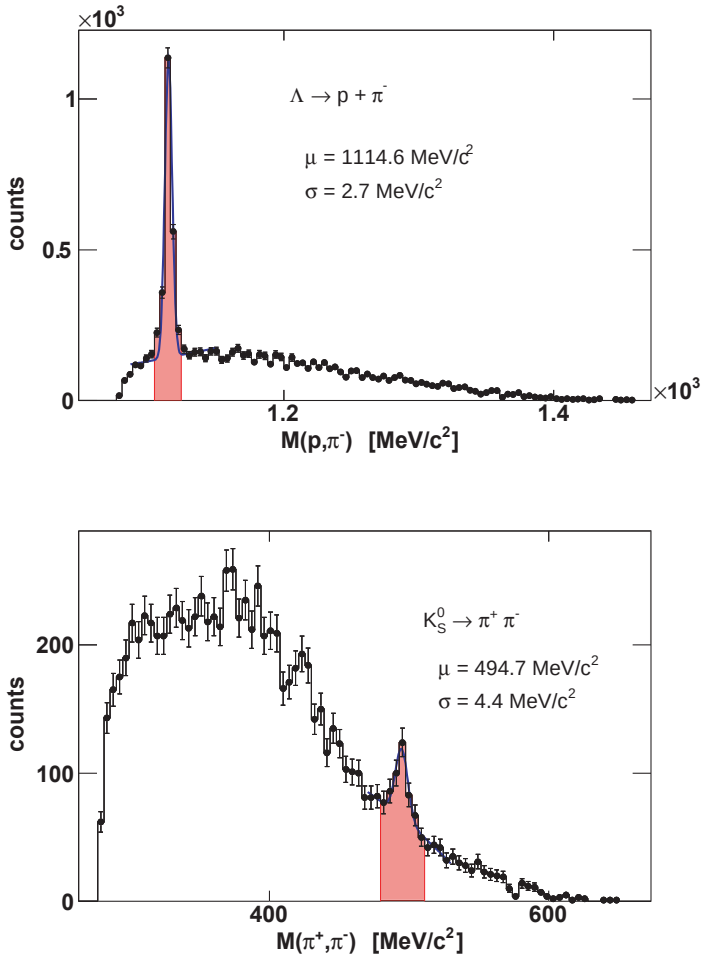

Figure 4.9: Top: Invariant mass of proton and π^-, showing a Λ signal. Bottom: Invariant mass of π^+ and π^-, showing a K^0_S signal. Both resonances are fitted with a Gaussian and a polynomial (blue lines). They are rejected in the analysis by cutting around the 2.75σ (red shaded) area (1107.2 MeV/c^2 − 1122.0 MeV/c^2 (top), 482.6 MeV/c^2 − 506.8 MeV/c^2 (bottom))

Figure 4.10 shows the missing mass (p,K^+,π^-) (top panel), giving the missing Σ^+, and the missing mass (p,K^+,π^+) (bottom panel), giving the missing Σ^-, for the remaining data set. Both pictures provide the comparison between the raw (blue histograms) and the refitted (red histograms) data sample. The expected resonances are clearly visible in all distributions, but below them, there is still misidentification background, as described above. This is expected by considering the signal to background ratio in figure 4.7.

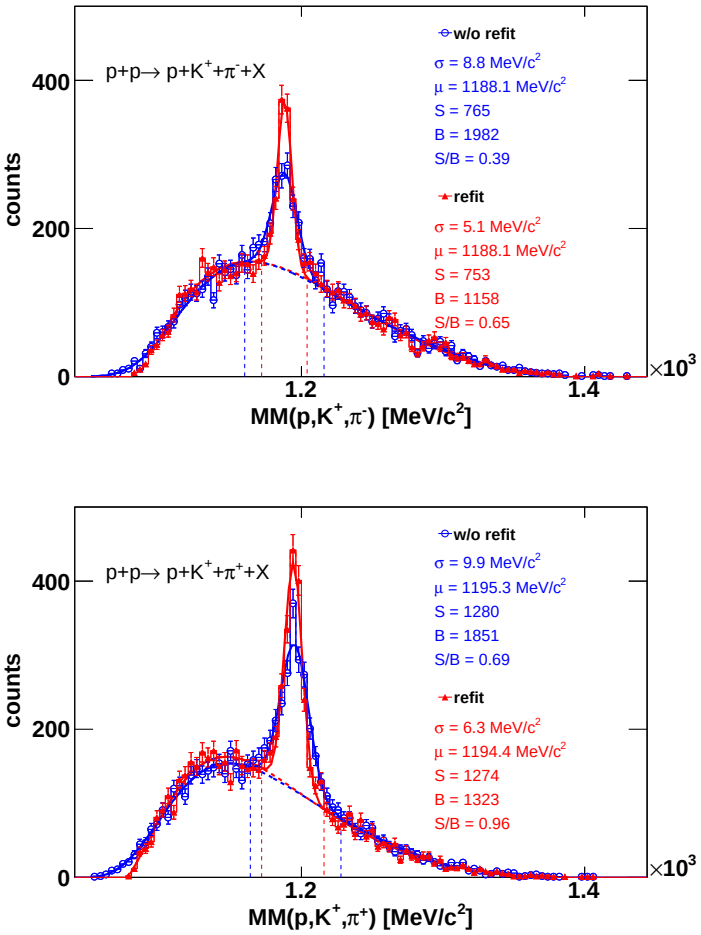

Figure 4.10: Top: Missing mass (p,K^+,π^-), showing a Σ^+. Bottom: Missing mass (p,K^+,π^+), showing a Σ^-. The blue distributions show the pure data set (without kinematic refit), the red distributions are the refitted data. All distributions are fitted with a Gaussian together with a Landau-function an a polynomial (solid lines). The amount of signal and background is determined by integrating within the vertical dashed lines from $(\mu - 3\sigma)$ to $(\mu + 3\sigma)$.

The large amount of background is the reason why the kinematic refit is so important for the analysis. Applying the refit results in a remarkably reduction in the width of the Σ^+ and the Σ^- resonance. It is furthermore crucial that the background is nearly unaffected, only the mass resolution is improved, and therefore the peaks get narrower. The solid lines are fits to the data and supply a width of the resonances, which is reduced by more than 30% for the refitted data. Since the channel (4.2) and (4.4) are in principal extracted by cutting around either the Σ^+ or the Σ^- pole masses, the reduction in the width is of high

importance. The vertical dashed lines in figure 4.10 illustrate the different 3σ cut areas, which are used to filter out the Σ^+ or Σ^- events, respectively.
Due to the refit, a narrower cut can be applied without loosing signal. Thus only background (especially misidentification background) is rejected by more than 25%. This is an essential progress in the $\Lambda(1405)$ analysis.

In order to further increase the background suppression, different cuts on the track topology and on the track quality can be applied:
The tracking procedure of HADES delivers track lines in the position space for each particle. The intersection of the trajectories, associated to the different particles, produced in each event, is used to calculate the primary vertex. By assuming that a Σ^+ event took place (like channel (4.4)), the trajectories of the proton, the K^+ and the π^- are used to determine the primary vertex.

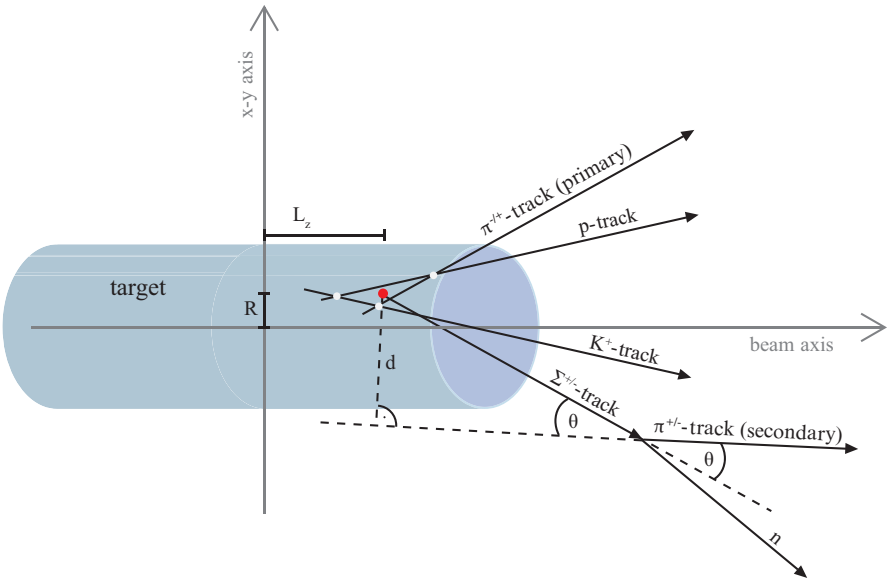

Figure 4.11: The intersection of the trajectories, associated to the three primary particles (p,K^+,$\pi^{-/+}$), are shown by the white points. They are used to calculate a mean primary vertex (red point) with a distance R to the z−axis, and a z−position L_z. The minimum track distance d of the secondary pion to the primary vertex depends on the angle Θ between the pion and the Σ.

In the case of a Σ^- hypothesis (like channel (4.2)) , the π^- is replaced by the π^+ (see figure 4.11). This respects already that the $\Lambda(1405)$ has a very short lifetime and therefore decays immediately inside the primary vertex. Thus the pion, coming out of its decay (primary pion), can be used for the vertex reconstruction. This vertex should be inside the LH_2 target, which has a cylindrical form centered around the z−axis. Its diameter is 25 mm, its length L is 50 mm [Aga09c]. Furthermore it is not centered at $z = 0$, but shifted to lower values [Sch09]. This can be seen in figure 4.12, where the distribution of all reconstructed primary vertices is shown. Of course the pictures do not represent the geometry of the target itself, but the interaction area of the proton beam with the target. The cuts on the primary vertex, which are finally used, are summarized in table 4.3 (first row). At this point one should mention that no vertex detector is available at HADES and hence, the vertex resolution is limited to $0.5 - 1.0$ cm [Sch09].

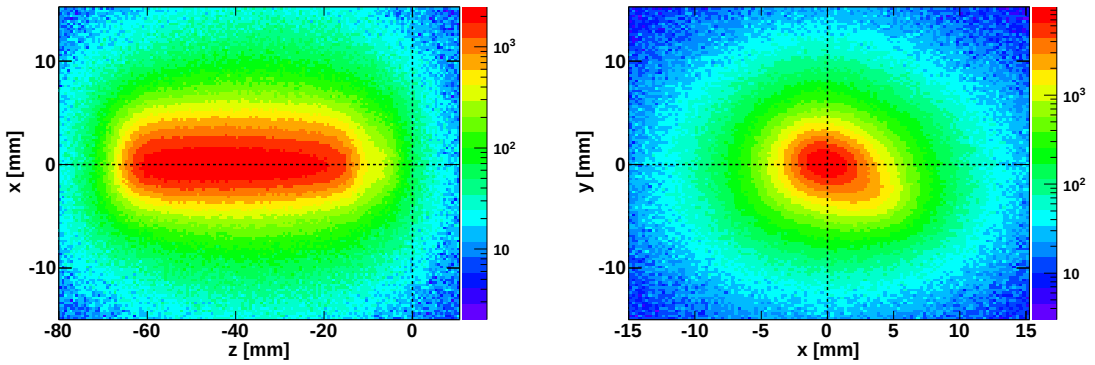

Figure 4.12: (a) x−value vs. z−value of all reconstructed vertices, showing a shift of the target to negative z−values. (b) y−value vs. x−value of the reconstructed vertices. A fluctuation of the proton beam during the experiment results in the oval form of the distribution.

Thus in order to keep a lot of signal, the cuts can not be very strict.
Additionally, the track distance of the secondary pion (coming out of the Σ decay) to the calculated primary vertex can be used for a further quality check. This is also illustrated in figure 4.11. The Σ^+ has a life time of $c\tau = 2.4$ cm, the Σ^- has a life time of $c\tau = 4.43$ cm [Gro08]. Thus the secondary pion should have a certain minimum distance d to the primary vertex, which depends on the angle Θ between the Σ track and the pion track ($d > d_{min} sin(\Theta)$). The assumed Σ track can easily be reconstructed with the track parameters of the proton, the K^+ and the primary pion. The angle dependent cuts, which are finally used, are listed in the second row of table 4.3.
The last quality check, which is applied to the data sample, concerns the kinematic refit. As was shown in chapter 3.4, the refitting of background events tend to low p−values. Thus background can be reduced by cutting on p−values larger than a minimum value. These cuts are shown in the third row of table 4.3.

Cut on:	Σ^+ *assumption*	Σ^- *assumption*
primary vertex	$0 < R < 10mm$ $-77 < L_z < 1.6mm$	$0 < R < 20mm$ $-77 < L_z < 1.6mm$
pion track distance to primary vertex	$d > 1mm + 1mm \cdot \sin(\Theta)$	$d > 1mm + 1mm \cdot \sin(\Theta)$
p−value	p−value > 0.04	p−value > 0.04

Table 4.3: Used cuts to reduce background. Left column: cuts for the missing Σ^+ . Right column: cuts for the missing Σ^-.

Figure 4.13 shows the missing mass (p,K^+,$\pi^{-/+}$) for the refitted tracks. The red histograms are the results without any track quality cuts, and are therefore the same as shown in figure 4.10. The black Σ^+ distribution (top panel) includes additionally the requirements, shown in the first column of table 4.3, whereas the black Σ^- distribution (bottom panel) is plotted, if the tracks fulfill the requirements in the second column. Of course it is unavoidable that some signal is rejected, but basically the cuts suppress background, which is obvious

in both pictures. Altogether, the signal to background ratio could be further increased by more than 20% with the application of these track quality criteria.
The chosen cuts were optimized to provide a good signal to background ratio by simultaneously not reducing the Σ^+ or the Σ^- signal too much.

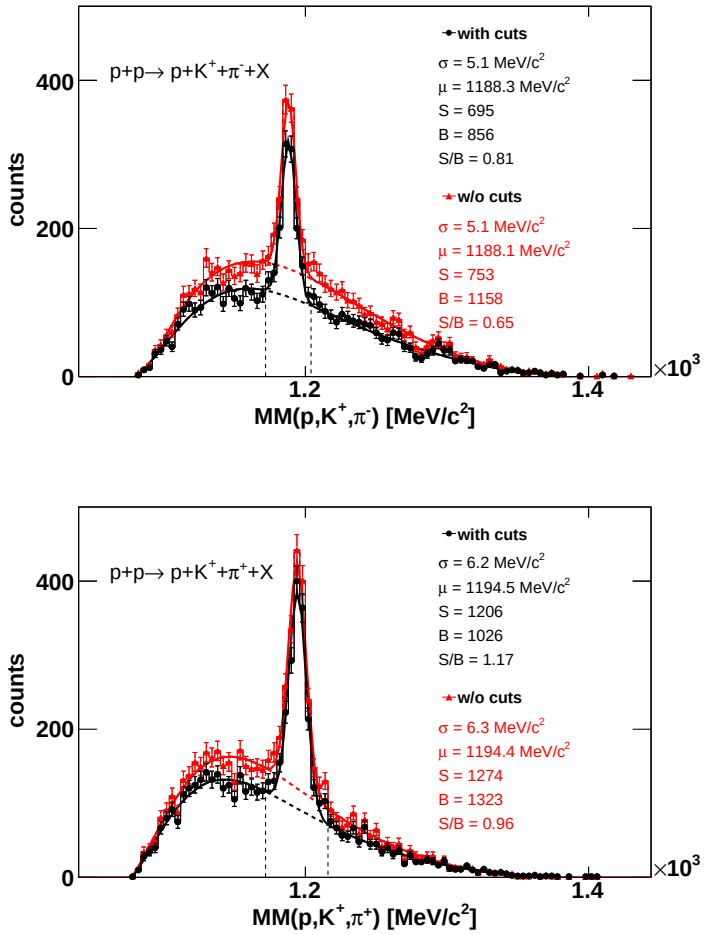

Figure 4.13: Top: Missing mass (p,K^+,π^-), showing a Σ^+. Bottom: Missing mass (p,K^+,π^+), showing a Σ^-. The refitted data without any further cuts (red) are compared to the refitted data after the cuts shown in table 4.3 (black). All distributions are fitted with a Gaussian together with a Landau-function and a polynomial (solid lines). The amount of signal and background is determined by integrating within the vertical dashed lines from $(\mu - 3\sigma)$ to $(\mu + 3\sigma)$.

Applying these procedures (kinematic refit, Λ and K^0_S rejection and track quality cuts) to the simulations produces the black Σ^+ and Σ^- distributions, shown in figure 4.14. The widths of the resonances in the simulation is in very good agreement with the widths in the experiment. Therefore the momentum resolution seems to be reproduced correctely. Included in both pictures are the different contributions to the obtained signal:

- The solid blue histogram is due to the production of $\Lambda(1405)$, which delivers a peak in both histograms.
- The $\Sigma(1385)^0$ contribution is indicated by the gray distribution, which also generates

a narrow peak in both channels but with limited strength.

- The same is valid for the $\Lambda(1520)$ contribution, presented in the dark green distributions.
- The red and the magenta histograms are due to reaction (4.15) and (4.16), respectively. They are the non resonant channels, since the Σ^+ or Σ^- is produced directly, without an intermediate resonance like the $\Lambda(1405)$. Channel (4.15) produces background below the Σ^+ peak, visible in the upper panel of figure 4.14. In the lower panel the roles are reversed. The reason for this is that by plotting the missing mass (p,K^+,π^+) for events, which contain an intermediate Σ^+ in their decay chain, an homogeneous distribution corresponding to the phase space of the decay channel is obtained.

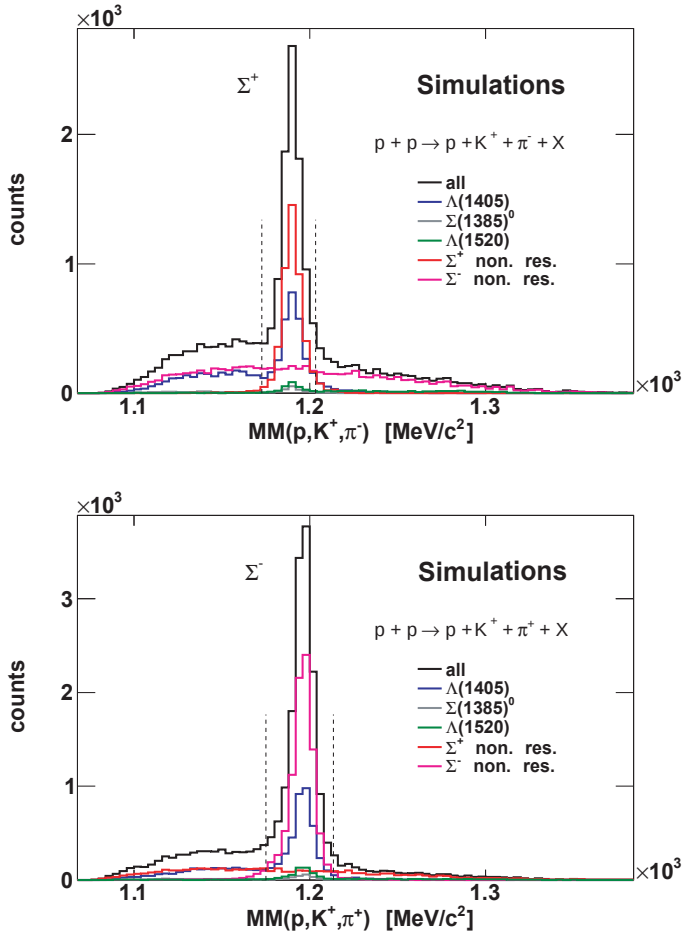

Figure 4.14: Missing mass (p,K^+,π^-) (top) and (p,K^+,π^+) (bottom) for the refitted tracks. The different contributions to the signal are indicated by the colored histograms.

Since the misidentificatin background is negligible, the total amount of background below both resonances is much lower in the simulations than in the comparable experimental results (figure 4.13, black histograms). However, the differential analysis of the simulations allow to disentangle all the different sources, contributing to the total signal, and to estimate the corresponding strengths.

4.2.3 Separation of the $\Lambda(1405)$ into the two charged decay channels

The reduction of misidentification background is optimized by applying the methods, presented in the last subsections. The final step is to investigate the missing mass (p,K^+), where one expects to see the $\Lambda(1405)$ signal. The goal, however, is to separate the $\Lambda(1405)$ into its two charged decay channels. This can be reached by using the following method [Nii08].
All events, belonging to the data sample S_{K^+} within the neutron mass range (see figure 4.7), are further refitted with two different constraints (besides the refit, which was already presented).
The first refit assumes that each selected event contains an intermediate Σ^+ resonance, like channel (4.4), and uses this assumption for a second constraint H_2:

Refit **A**:

$$H_1 = \quad MM(p,K^+,\pi^+,\pi^-) - M(n) = 0 \tag{4.22}$$

$$H_2 = \quad MM(p,K^+,\pi^-) - M(\Sigma^+) = 0 \tag{4.23}$$

The second refit is similar, but here the hypothesis is, that a Σ^- was produced. The events within the neutron mass range are thus refitted with the following constraints:

Refit **B**:

$$H_1 = \quad MM(p,K^+,\pi^+,\pi^-) - M(n) = 0 \tag{4.24}$$

$$H_2 = \quad MM(p,K^+,\pi^+) - M(\Sigma^-) = 0 \tag{4.25}$$

The idea is, that if really a Σ^+ event took place, the refit **A** should provide a better result than refit **B**. As a consequence the $p-$value of refit **A** should be larger than the $p-$value of refit **B** (see section 3.3) and vice versa for a Σ^- event. Each event of the data set S_{K^+} can thus be selected to belong either to the ($\Sigma^+\pi^-$) sub sample or to the ($\Sigma^-\pi^+$) sub sample, if the left or right column in table 4.4 is fulfilled, respectively.

Conditions:	$\Sigma^+\pi^-$ *sub sample*	$\Sigma^-\pi^+$ *sub sample*
inside neutron mass range (figure 4.7)	910 MeV/c^2 $< MM(p,K^+,\pi^+,\pi^-) <$ 971 MeV/c^2	910 MeV/c^2 $< MM(p,K^+,\pi^+,\pi^-) <$ 971 MeV/c^2
not rejected by Λ cut (figure 4.9, top panel)	$M(p,\pi^-) > 1122$ MeV/c^2 or $M(p,\pi^-) < 1107$ MeV/c^2	$M(p,\pi^-) > 1122$ MeV/c^2 or $M(p,\pi^-) < 1107$ MeV/c^2
not rejected by K^0_S cut (figure 4.9, bottom panel)	$M(\pi^+,\pi^-) > 503$ MeV/c^2 or $M(\pi^+,\pi^-) < 480$ MeV/c^2	$M(\pi^+,\pi^-) > 503$ MeV/c^2 or $M(\pi^+,\pi^-) < 480$ MeV/c^2
track quality cuts	left column in table 4.3 fulfilled	right column in table 4.3 fulfilled
inside appropriate Σ mass range (figure 4.13)	1172.8 MeV/c^2 $< MM(p,K^+,\pi^-) <$ 1203.4 MeV/c^2	1175.1 MeV/c^2 $< MM(p,K^+,\pi^+) <$ 1213.5 MeV/c^2
quality of refit **A** and **B**	$p-$value **A** $<$ $p-$value **B**	$p-$value **B** $<$ $p-$value **A**

Table 4.4: Required conditions to classify an event as a ($\Sigma^+\pi^-$) event (left column) or as a ($\Sigma^-\pi^+$) event (right column).

This procedure is unambiguous, meaning that an event belongs either to the $(\Sigma^+\pi^-)$ sub sample or to the $(\Sigma^-\pi^+)$ sub sample, but not to both. In this way a clear separation of the $\Lambda(1405)$ is possible.
It was checked with simulations that more than 89% of the events, which are identified as a $(\Sigma^+\pi^-)$ event with this method, are identified correctly. The remaing 11% are actually $(\Sigma^-\pi^+)$ events. The $(\Sigma^-\pi^+)$ classification works even better. More than 97% of the events are identified correctly. Thus the purity of the separation is quite good.
Figure 4.15 shows the missing mass (p,K^+) for the Σ^+ channel (top panel) and the Σ^- channel (bottom panel).

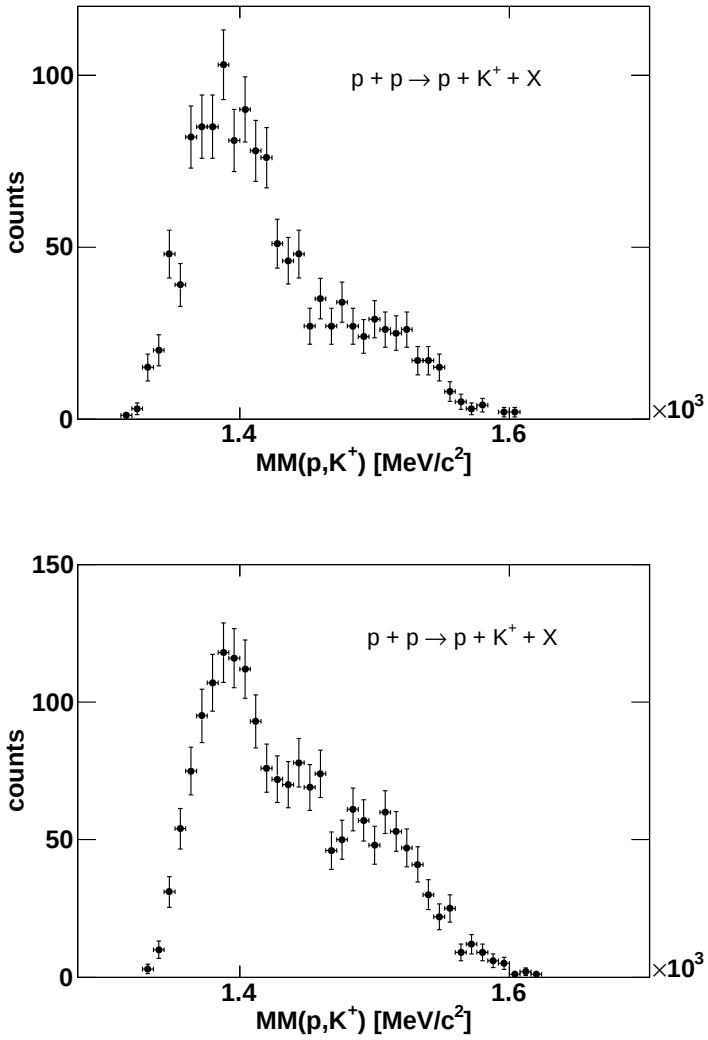

Figure 4.15: Top: Missing mass (p,K^+) for the Σ^+ channel. Bottom: Missing mass (p,K^+) for the Σ^- channel. The refitted proton and K^+ track (refit with only one constraint) are used for the missing mass calculation.

The mass is calculated with the proton and the K^+ tracks, obtained after the refit with the one constraint condition (4.21). In both cases a clear peak appears around 1400 MeV/c^2. That we associate to the contribution by $\Lambda(1405)$. However, the broad background dis-

tribution, which overlays the signal, creates a kind of shoulders on the right sides of the spectra.
It is instructive to compare the spectra in figure 4.15 to the appropriate results in the simulations. This is shown in figure 4.16, where all simulated events are classified in the same way as it is done in the experimental data (table 4.4).

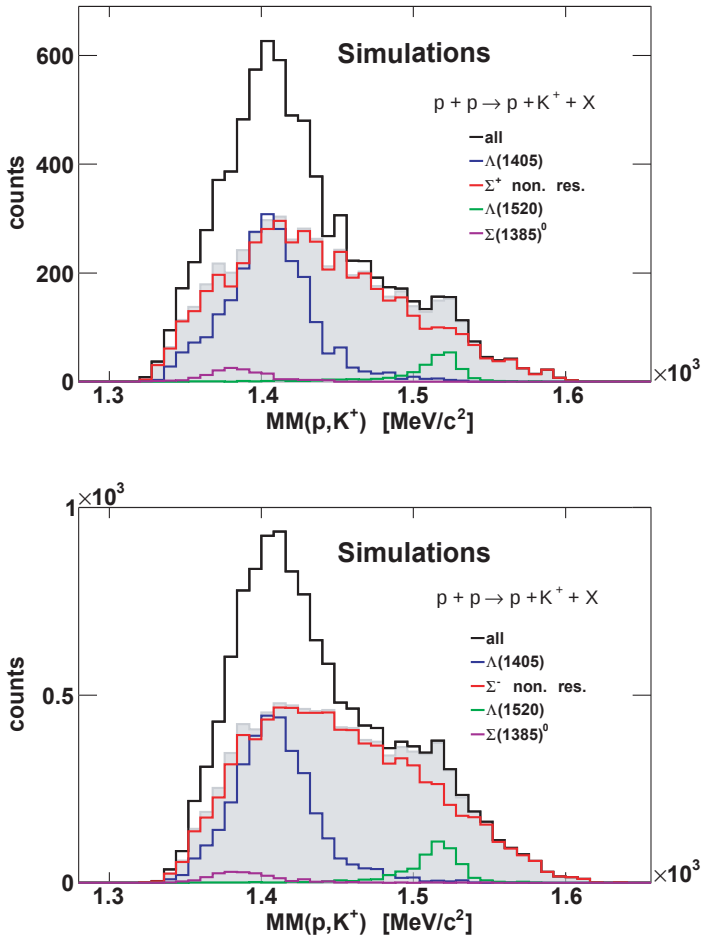

Figure 4.16: Missing mass (p,K^+) for the Σ^+ channel (top) or the Σ^- channel (bottom). The different contributions to the total signal are shown in the colored distributions. All these contributions except for the one of the $\Lambda(1405)$ are added up to the gray histogram.

In black are the summed spectra of the remaining channels. They look quite similar to the experimental results. The broadening on the right sides of the spectra is mainly due to the non resonant channels (4.15) and (4.16) (red histograms). They deliver broad phase space distributions, which overlap totally with the $\Lambda(1405)$ (blue histograms). The small contribution of $\Lambda(1520)$ is visible in dark green. As was already predicted, the $\Sigma(1385)^0$ resonance (violet) overlaps totally with the $\Lambda(1405)$.

Although the results in the experiment and in the simulations are already comparable, a complete understanding of the experimental spectra is only possible, if the misidentification background is taken into account. This is discussed in the next section.

4.3 Modeling the background and the pure $\Lambda(1405)$

The main goal of the following section is to obtain a pure $\Lambda(1405)$ signal by subtracting all other contributions from the spectra in figure 4.15. As it was shown, the non resonant channels (4.15) and (4.16), as well as the $\Sigma(1385)^0$ and the $\Lambda(1520)$ can be described with simulations. Only the misidentification background remains to be investigated. One can try to do this with simulations, too, but not all effects and channels, which lead to the misidentification, are known here. Furthermore, a huge amount of simulations would be necessary to get enough statistics. A second possibility is to describe it with experimental data. For that purpose a new method was developed, which is mainly based on a sideband analysis on the K^+ mass distribution. The following part concentrates first on the modeling and understanding of the background below the neutron signal (figure 4.7). As was seen in the last section, this background is indeed only due to misidentification of a pion or a proton as a K^+. Finally the contributions to the spectra in figure 4.13 and 4.15 are investigated.

4.3.1 Sideband analysis on the K^+ mass

The data set for figure 4.7 (S_{K^+}) is obtained after a mass cut on the kaon mass (350 MeV/c^2 – 650 MeV/c^2), as described before. Besides the few events with true kaons, which lead to the neutron peak in figure 4.7, this sample contains mainly misidentified pions and protons. The principal idea of the sideband analysis is to create a new data sample by selecting kaon candidates outside the kaon mass area. The so obtained sample includes almost no true kaons but mainly pions and protons, which are then 'misidentified' as kaons. The strategy is to analyze this sample in order to describe the misidentification background visible in figure 4.7.
In order to obtain high statistics for the sideband analysis, a completely new set of events is created with a proton, a K^+, a π^+ and a π^-. The kaons are not selected by applying any dE/dx cuts, but all positive particles, which are then mainly protons and pions, are identified as a K^+. Figure 4.17 shows the squared mass of all the obtained kaon candidates. The squared mass area from -300000 (MeV/c^2)^2 to 0 (MeV/c^2)^2 (red shaded area) is chosen to select pions, misidentified as a K^+, the area from 615000 (MeV/c^2)^2 to 4000000 (MeV/c^2)^2 (blue shaded area) is chosen to select protons, misidentified as a K^+. These two data samples (S_{π^+} and S_p) are used to describe the background below the neutron signal in figure 4.7 by plotting the missing mass (p,K^+,π^+,π^-). Unfortunately this fails due to several reasons:

1. Although the sideband areas are quite distant to the nominal kaon mass, they still contain a non negligible amount of true kaons, which is a consequence of the poor mass resolution. This is problematic, since these events will supply a neutron signal in the missing mass (p,K^+,π^+,π^-) spectrum. The goal, however, is to describe everything, but not the neutron signal in figure 4.7. Therefore these true kaon events have to be suppressed in the sideband sample.

2. The kinematics of the kaon candidates in the blue and the red shaded areas differ from the kinematics of the kaon candidates inside the kaon mass area (350 MeV/c^2 –

650 MeV/c^2) and consequently also the $MM(p,K^+,\pi^+,\pi^-)$ spectrum is distributed differently. In order to get a complete description of the background in figure 4.7, the sideband sample must be adapted in such a way to reflect the momentum distribution of the kaon candidates in S_{K^+}.

3. The different contributions of pions and protons to the misidentification background is not known. However the chosen red and blue areas fix their amount to arbitrary values, which are surely not correct.

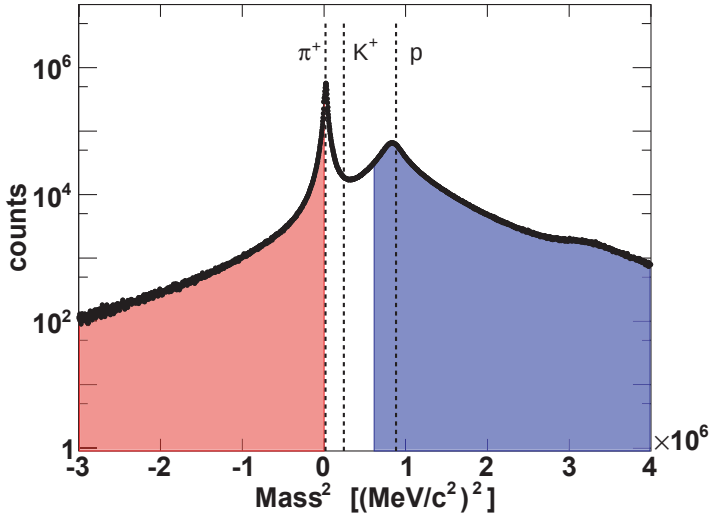

Figure 4.17: Squared mass of all K^+ candidates. The red shaded area selects mainly π^+ for the sideband analysis, the blue shaded area filters out mainly protons. The vertical dashed lines indicate the nominal squared mass of π^+, K^+ and protons.

The first problem is approached in the following way.
Simulations have shown that a large contribution to the misidentification background directly below the neutron peak is due to the reaction:

$$\begin{aligned} p + p \xrightarrow{3.5GeV} & \Delta^{++} + p + \pi^+ + \pi^- + \pi^- \\ & \hookrightarrow \; p + \pi^+ \qquad\qquad 100\% \end{aligned} \tag{4.26}$$

A proton, a π^+ and a π^- are identified correctly in the analysis. Preferably the remaining π^+ can be misidentified as a K^+ and in this way misidentification background is produced. The remaining, undetected particles fly in the forward direction. Since reaction (4.26) provides altogether six particles in the final state, the missing mass spectrum (p,K^+,π^+,π^-) is pure phase space and has no physical meaning. Therefore exchanging the magnitude of the momenta (not the direction of the momenta) of the identified π^+ and the identified π^- in these events should almost not change the missing mass distribution. This exchange is similar to the mixed event procedure, which is a well known tool in the analysis of heavy ion physics [Sch09].
The idea is that if the momentum exchange is applied to an event of the sideband sample

with a true K^+, the correlation of the particles in this event is lost. Consequently also the neutron signal, which these events would produce, is rejected.
However, it is not possible to exchange the momenta of all events in the sideband samples. The reason is that there are further background channels (identified again with simulations), which are partially responsible for the large yield on the left side of the neutron peak (figure 4.7). These channels have all the same final state products:

$$p + p \xrightarrow{3.5GeV} p + n + \pi^+ + \pi^+ + \pi^- \tag{4.27}$$

In this reaction one of the two π^+ could be misidentified as a K^+, the other particles are identified correctly. The exchange of the magnitude of the momenta between the identified π^+ and the π^- is not recommended, since there is only one missing particle, the neutron, and an exchange would thus influence the line shape of the missing mass (p,K^+,π^+,π^-) distribution. In order to exclude these events from the momentum exchange, all K^+ candidates of the sideband data sample in the red shaded area are reset to the nominal mass of the π^+ ($K^+ \rightarrow \pi^+$). If then the missing mass (p,π^+,π^+,π^-) is inside the neutron mass range (844 MeV/c^2 – 1036 MeV/c^2), the event is classified as being of reaction (4.27) and thus no momenta exchange is applied.
One could wonder why these events are not excluded completely from the analysis by applying this neutron mass cut. The answer is that this would first of all not reduce the background below the neutron peak in figure 4.7 at all, but only partially suppress the yield on the left side. The second point is that this yield is very useful in order to scale the sideband data, as will be shown later.
Altogether, the sideband data set in the red shaded area is divided into two sub samples:

- One with exchanged pion momenta (tagged by $S_{\pi_1^+}$), in order to suppress true kaon events.
- And one without this exchange (tagged by $S_{\pi_2^+}$).

It is by now not clear how much these both sub samples contribute to the final misidentification background.
The sideband data set in the blue shaded area (S_p) is not modified at all, meaning that no pion momenta are exchanged.
The second mentioned issue is illustrated in figure 4.18 (panel (a)). The black histogram shows the momentum distribution ($f_{K^+}(|\vec{p}|)$) of all kaon candidates in the data sample S_{K^+}. Compared to it are the momentum distributions of the kaon candidates in the sideband samples. The distribution of sub sample $S_{\pi_1^+}$, tagged as $f_{\pi_1^+}(|\vec{p}|)$, and the distribution of sub sample $S_{\pi_2^+}$, tagged as $f_{\pi_2^+}(|\vec{p}|)$, are added up to the red histogram. However $f_{\pi_1^+}(|\vec{p}|)$ was before scaled with a factor $b_{\pi^+} = 1.2$. The reason for this scaling factor will become clear later. The blue momentum distribution ($f_p(|\vec{p}|)$) is due to the kaon candidates in the data set S_p. In order to allow a comparison between all spectra, the blue and the red histograms are scaled down by a factor of 0.2. It is obvious that the three distributions are quite different. The goal is, however, to describe the data set S_{K^+} as good as possible and therefore it is crucial that the kinematics of the sideband data set are comparable to the ones in S_{K^+}. This is reached by adapting the momentum distribution of the sideband sample to the one of S_{K^+} with the following method [Sch09].

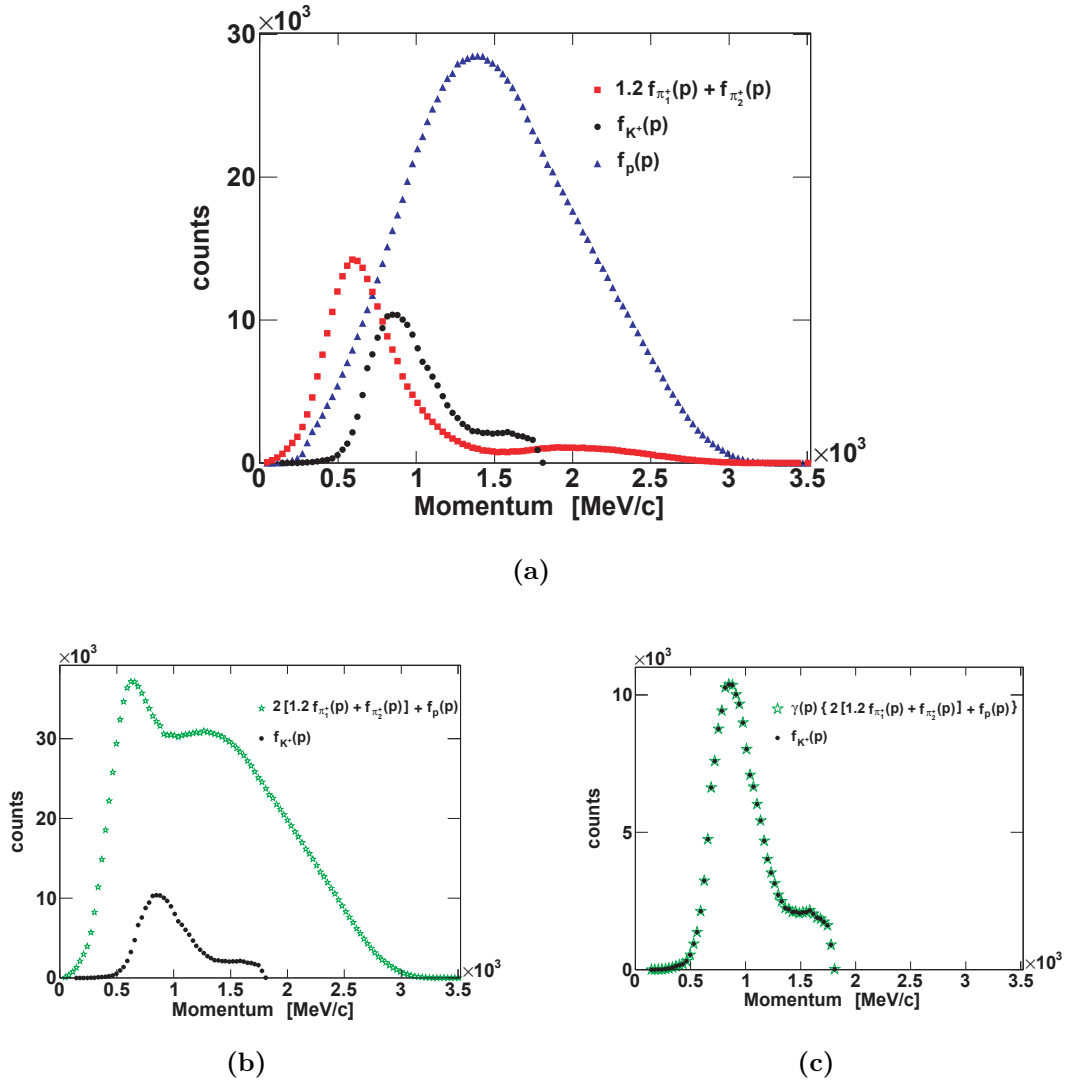

Figure 4.18: (a) Momentum distributions of the kaon candidates in the different data samples S_{K^+}, $S_{\pi_1^+}/S_{\pi_2^+}$ and S_p. (b) the momentum distributions of the sideband data samples are added up to the green histogram. The distribution $[1.2 f_{\pi_1^+}(|\vec{p}|) + f_{\pi_2^+}(|\vec{p}|)]$ is before scaled with an arbitrary factor $a_{\pi^+} = 2$. (c) by multiplying the combined momentum distribution of the sideband samples with the momentum dependent scaling factor $\gamma(|\vec{p}|)$, the momentum distribution of the kaon candidates in S_{K^+} is reconstructed.

The distribution $(b_{\pi^+} f_{\pi_1^+}(|\vec{p}|) + f_{\pi_2^+}(|\vec{p}|))$ is scaled with a value a_{π^+}, the distribution $f_p(|\vec{p}|)$ is not scaled. The two distributions are then added up to a combined momentum distribution $(a_{\pi^+}[b_{\pi^+} f_{\pi_1^+}(|\vec{p}|) + f_{\pi_2^+}(|\vec{p}|)] + f_p(|\vec{p}|))$. This is exemplified in the green histogram in figure 4.18 (panel (b)). As the relative contributions of pions and protons to the misidentification background is not known by now, the implementation of a_{π^+} is reasonable, but its correct value has to be determined (see below). The obtained combined momentum distribution is afterwards scaled to the momentum distribution $f_{K^+}(|\vec{p}|)$.

This delivers a momentum dependent scaling factor $\gamma(|\vec{p}|)$:

$$\gamma(|\vec{p}|) = \frac{f_{K^+}(|\vec{p}|)}{a_{\pi^+}[b_{\pi^+} f_{\pi_1^+}(|\vec{p}|) + f_{\pi_2^+}(|\vec{p}|)] + f_p(|\vec{p}|)} \tag{4.28}$$

By multiplying the sideband data with the factor $\gamma(|\vec{p}|)$, the momentum distribution ($f_{K^+}(|\vec{p}|)$) of the K^+ candidates in S_{K^+} can be reproduced (see figure 4.18, panel (c)). The correct values for the scale factors b_{π^+} and a_{π^+} are still unknown. They can be determined in the following way:
a_{π^+} is varied within a total of 200 different values ($a_{\pi^+} = 0.2n + 90$, $n = 0..199$), b_{π^+} is set to couple of values between 1.0 and 2.0.

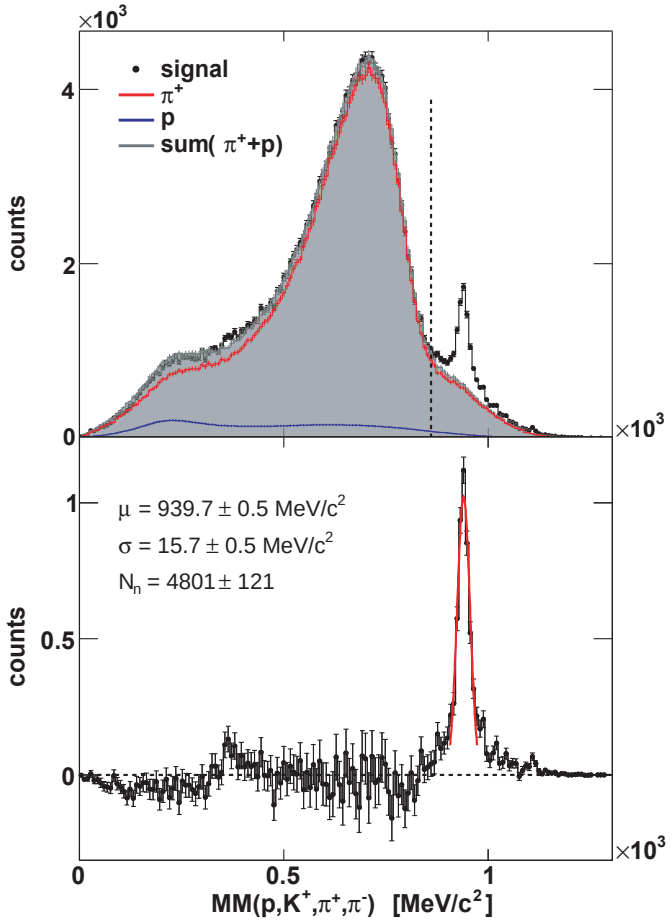

Figure 4.19: Top: Missing mass (p,K^+,π^+,π^-) for the data set S_{K^+} (black distribution) and for the sideband data set (gray distribution). The shown sideband histogram with the scale factor set ($a_{\pi^+} = 0.2 \cdot 44 + 90$, $b_{\pi^+} = 1.2$) fits best to the black histogram. The χ^2 value for that fit is calculated inside the range $0 < MM(p,K^+,\pi^+,\pi^-) < 860$ MeV/c^2 (vertical dashed line). Bottom: Pure neutron signal after the background subtraction. The peak is fitted with a Gaussian (red line).

For each scale factor set (a_{π^+},b_{π^+}) the function $\gamma(|\vec{p}|)$ is determined as described above. Then the missing mass (p,K^+,π^+,π^-) is plotted for the full sideband data set, but now in order to respect the kinematics of S_{K^+}, each event in the red shaded area, which belongs to sub sample $S_{\pi_1^+}$, is before scaled with the appropriate values a_{π^+}, b_{π^+} and $\gamma(|\vec{p}|)$. The events of sub sample $S_{\pi_2^+}$ are scaled with a_{π^+} and $\gamma(|\vec{p}|)$. The events in the blue shaded area have to be scaled with $\gamma(|\vec{p}|)$ (see equation (4.28)). The correct set (a_{π^+},b_{π^+}) should deliver a missing mass (p,K^+,π^+,π^-) distribution, which, except for the neutron peak, fits to the spectrum in figure 4.7. Quantitatively this can be evaluated by calculating a χ^2 value for the mass range from $0 < MM(p,K^+,\pi^+,\pi^-) < 860$ MeV/c^2. The minimum χ^2 value and thus the best fit is obtained for the scale factor set ($a_{\pi^+} = 0.2 \cdot 44 + 90$,$b_{\pi^+} = 1.2$). The result for this set is shown in figure 4.19 (top). The sideband data (gray histogram) describe the background perfectly. Also the background directly below the neutron peak seems to be correct. Furthermore the exchange of the pion momenta in the data set $S_{\pi_1^+}$ results in a total suppression of events with true kaons and thus no neutron peak appears in the sideband distribution.
The presented method has the further advantage that the different contributions of pions (red histogram) and protons (blue histogram) to the total misidentification background are resolved. Thus also the third mentioned issue of the sideband analysis is solved. The lower picture of figure 4.19 shows the result after subtracting the reconstructed background. It provides a very pure neutron signal.

4.3.2 Σ^+, Σ^- and the $\Lambda(1405)$

Understanding the misidentification background below the neutron peak and being able to model it with a sideband analysis is an essential progress in the analysis. As a next step, it is desirable to understand, how the line shapes in figure 4.13 are build up and finally to understand the different contributions to the missing mass (p,K^+) spectra in figure 4.15. For that purpose the sideband data has to be analyzed in exactly the same way as the data sample S_{K^+} (see subsection 4.2.2-4.2.3). However the events in the different sideband data samples ($S_{\pi_1^+}$,$S_{\pi_2^+}$ and S_p) must additionally be scaled with the appropriate factors (a_{π^+}, b_{π^+} and $\gamma(|\vec{p}|)$). In this way the misidentification background below the Σ^+, the Σ^- and in the missing mass spectra (p,K^+) can be described.
Figure 4.20 shows the missing mass (p,K^+,π^-) (top panel) and missing mass (p,K^+,π^+) (bottom panel). Simultaneously the missing mass (p,K^+) for the two different charged channels is investigated in figure 4.21. The black data points are obtained from the analysis of data set S_{K^+} and are thus the same spectra as shown in figure 4.13 and 4.15, respectively.
Considering first figure 4.20. Besides the experimental data points, all contributions to the spectra are shown. First of all there is the misidentification background in dark blue, obtained with the sideband analysis. All other contributions are extracted from the simulations (see figure 4.14). The non resonant channels (4.15) and (4.16) are shown in light blue and magenta. The contributions of $\Lambda(1520)$ are represented by the dark green histograms. Finally the spectra associated to $\Lambda(1405)$ and $\Sigma(1385)^0$ are added up to the black distributions. However, the $\Lambda(1405)$ is simulated as having a pole mass of 1405 MeV/c^2 (see figure 4.16). As will be seen later, the experimental results deliver a lower pole mass. The consequences of this lower mass for the black distributions in figure 4.14 remain to be investigated.

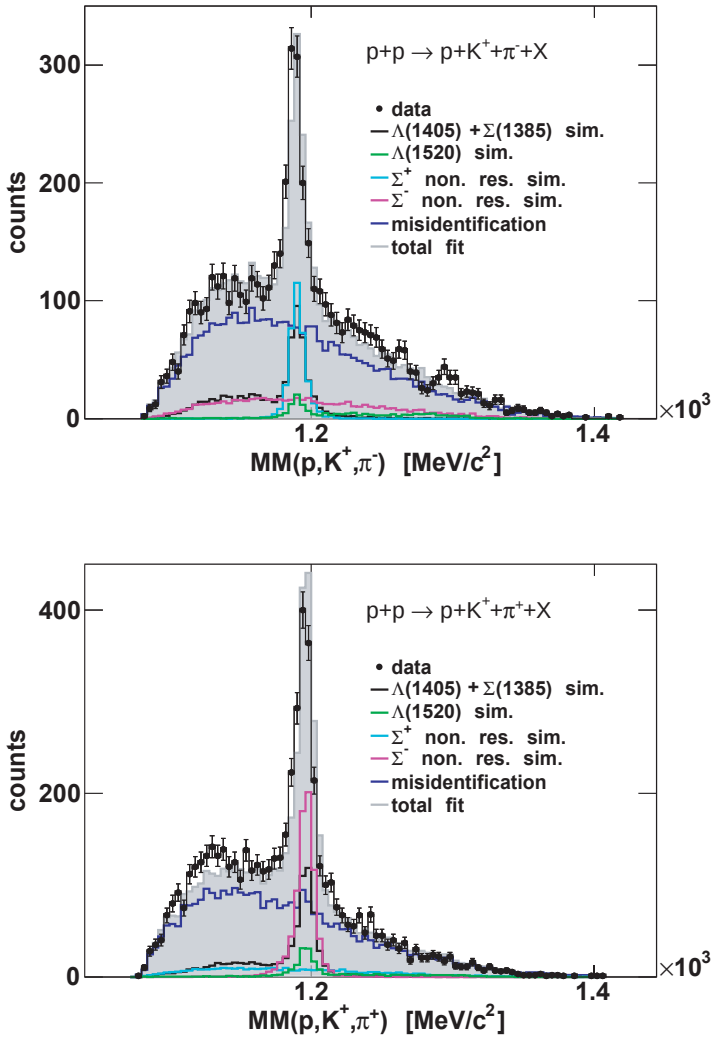

Figure 4.20: Top: Missing mass (p,K^+,π^-), showing the Σ^+. Bottom: Missing mass (p,K^+,π^-), showing the Σ^-. The colored histograms are the different contributions to the experimental spectra and are scaled with the appropriate fit values. The fit was performed for the full mass range

The experimental missing mass (p,K^+) spectra in figure 4.21 are also composed of different contributions. Again the dark blue distributions are the misidentification background, obtained with the sideband analysis. The red histograms respect the non resonant channels, where in the upper picture the main contribution is due to channel (4.16), and in the lower picture mainly channel (4.15) is the dominant one. The $\Lambda(1520)$ and the $\Sigma(1385)^0$ are shown in dark green and violet. The only contribution, which is not shown, is the $\Lambda(1405)$ itself, since its line shape is unknown. The different contributions in figure 4.20 (panel (a) and panel (b)) and in figure 4.21 (panel (a) and panel (b)) are fitted simultaneously to the four experimental spectra (black data points). For that purpose only the scaling factor of each contribution is taken as a fit parameter, the line shapes are fixed by the analysis itself. This leads altogether to five different fit parameters (misidentification, Σ^+ non resonant, Σ^- non resonant, $\Lambda(1405) + \Sigma(1385)^0$ and $\Lambda(1520)$) for four different spectra.

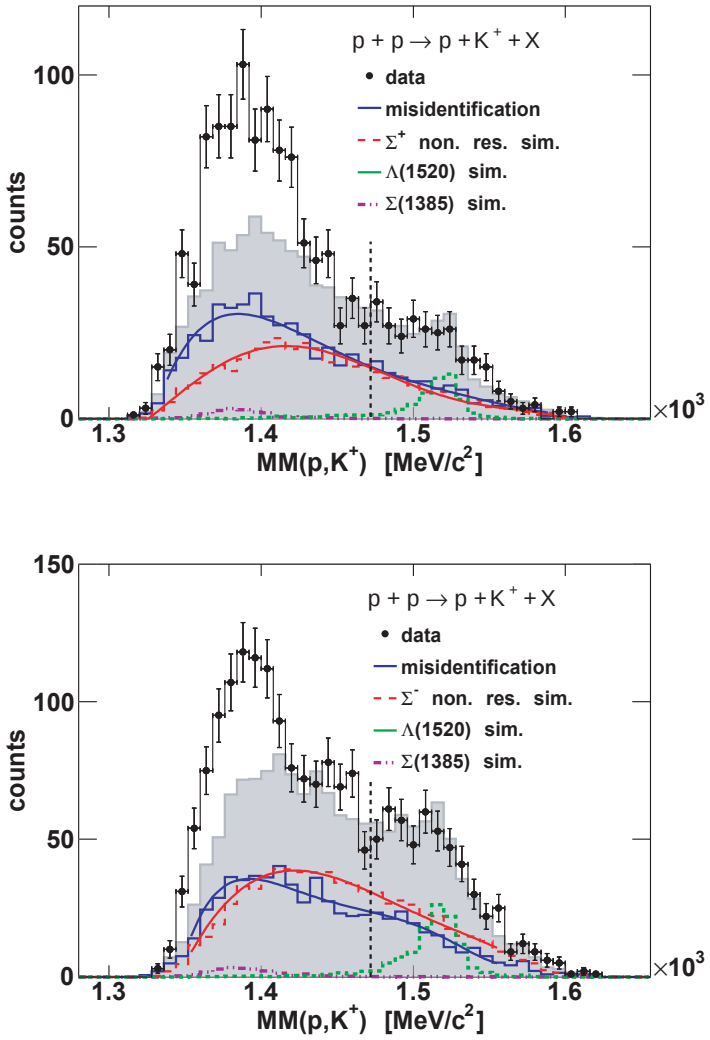

Figure 4.21: Top: Missing mass (p,K^+) for the ($\Sigma^+\pi^-$) decay channel. Bottom: Missing mass (p,K^+) for the ($\Sigma^-\pi^+$) decay channel. The colored histograms represent the different contributions to the total yield. The shape of each contribution is extracted from simulations or from the sideband analysis and the yields are scaled with the appropriate fit values. The vertical dashed lines (1470 MeV/c^2) indicate the lower limit for the adaption of the background. The red and the dark blue line shapes are fitted with polynomial functions, which are later subtracted from the experimental data.

The calculation of this scale factors is done via χ^2 minimization. The spectra in figure 4.20 are fitted in the full mass range, whereas the spectra in figure 4.21 are only fitted for missing masses above the vertical dashed lines. In this way, the mass range of the $\Lambda(1405)$ is excluded from the fitting procedure, which is reasonable.
The spectra from the sideband analysis and from the simulations, which are shown in figure 4.20 and 4.21, are already scaled with the fit parameters of the χ^2 minimization. They are furthermore added up to the gray distributions, which can be compared to the experiment. As one can see, the experimental results in figure 4.20 can be reconstructed

almost perfectly. Also the right sides of the spectra in 4.21 are described quite well. This is confirmed in the normalized χ^2 value for the total fit ($\chi^2/ndf = 1.29$). Thus the different contributions to the signals are understood and well controlled, which is the most essential step in order to finally get a pure $\Lambda(1405)$.
The following aspects of the fitting procedure must be considered carefully:

- Although the misidentification background is already scaled by the fit to the missing mass (p,K^+,π^+,π^-) spectra (figure 4.19), it is again included in the fitting procedure, which was just described. The reason is that the fit to figure 4.19 is only done in a mass range of $0 < MM(p,K^+,\pi^+,\pi^-) < 860$ MeV/c^2. Thus especially the strengths of the background exactly below the neutron peak, which is the important one for further investigations, can not be totally fixed in this way. However the fit to the experimental spectra in figure 4.20 and 4.21 increases the absolute scaling factor of this misidentification background only by 8%.

- The $\Lambda(1405)$ and the $\Sigma(1385)^0$ contributions are first added up, and then they are fitted to the spectra (see black histogram in figure 4.20). It is not possible to scale them independently, since their contributions in figure 4.20 and figure 4.21 overlap completely. Their relative cross sections are thus fixed by the values in table 4.1. Furthermore their common scaling factor is only fixed by the fit to the spectra in figure 4.20.

In order to get the pure $\Lambda(1405)$, the different identified contributions in figure 4.21 have to be subtracted. The blue and the red histograms are therefore fitted with polynomial functions of fifth order (see figure 4.21) and only these fits are subtracted. Since the polynomials are smooth, the final spectra are not biased by the subtraction of any statistical fluctuations, which appear in the blue and red histograms. The results after the subtraction of the misidentification background, of the non resonant phase space distributions and of the $\Sigma(1385)^0$ is shown in figure 4.22. In both channels a very clear $\Lambda(1405)$ signal is visible, each with a yield of about 330 entries. Additionally, the $\Lambda(1520)$, which was not subtracted, is indicated at higher energies, and seems to be in good agreement with the simulations (green histograms).

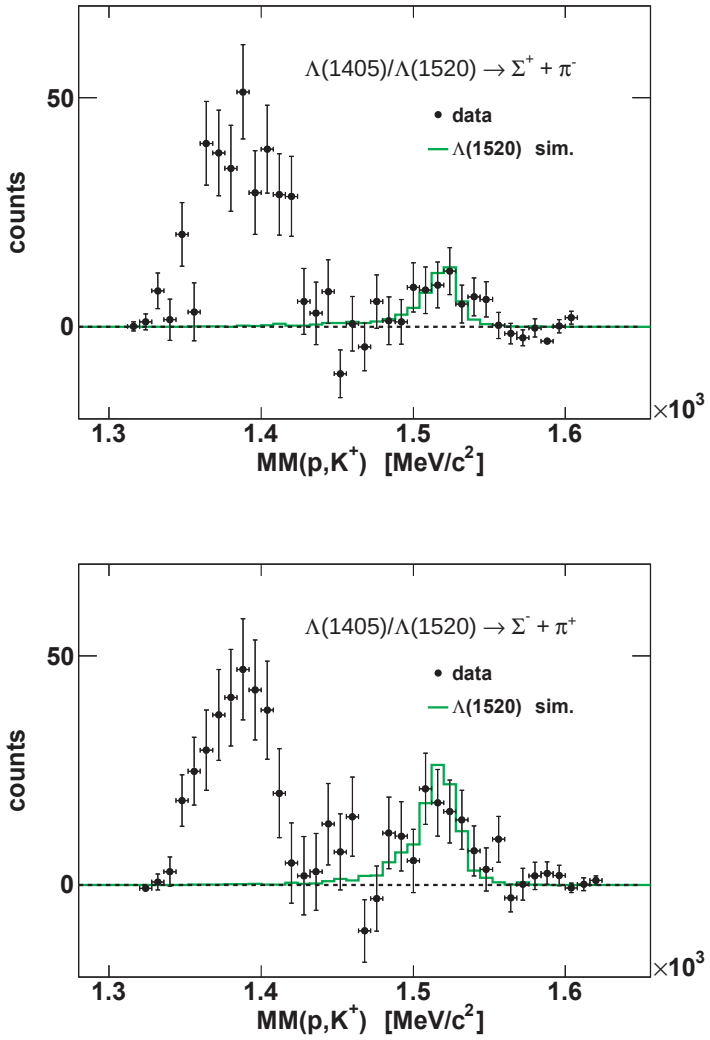

Figure 4.22: Missing mass (p,K^+) after subtraction of the different background contributions. The $\Lambda(1520)$ is compared to the simulations (green histograms).

Thus the main goal of this work, the separation of the $\Lambda(1405)$ into the charged decay channels (4.4) and (4.2), is reached. A critical point in the presented analysis is the subtraction of the $\Sigma(1385)^0$. On the one hand, the relative cross sections of the $\Lambda(1405)$ and the $\Sigma(1385)^0$ are not totally clear. The values in table 4.1, which were used in this work, might be not absolutely correct. On the other hand, the exact line shape of the $\Sigma(1385)^0$ is not known and might be different to a Breit-Wigner-function, which was used in the simulations. These points remain under investigation and have to be clarified. However, with the results of the $\Sigma(1385)^+$ analysis, presented in the next chapter, a reference value for the cross section measurement of the $\Sigma(1385)^0$ can be obtained for future investigations. Finally one should mention that the pictures in figure 4.22 do not include systematic errors by now and are also not corrected for efficiency and acceptance.

The last step is a comparison between the line shapes of the three different decay channels, shown in figure 4.23. The data for the $\Lambda(1405)$, decaying into the neutral ($\Sigma^0\pi^0$) channel, are taken from the recent publication of the ANKE collaboration [Zyc08], and are scaled by an arbitrary factor to have a shape overlap of the different spectra. The measurement was also performed for $p + p$ reactions but at a slightly lower beam energy of 2.85 GeV. Consequently no $\Lambda(1520)$ signal is visible in the blue distribution. For the $\Lambda(1405)$ mass range the spectra are in good agreement and do not provide any shift in the pole mass or differences in the line shapes. However, the large errors in all the spectra make a final statement difficult.

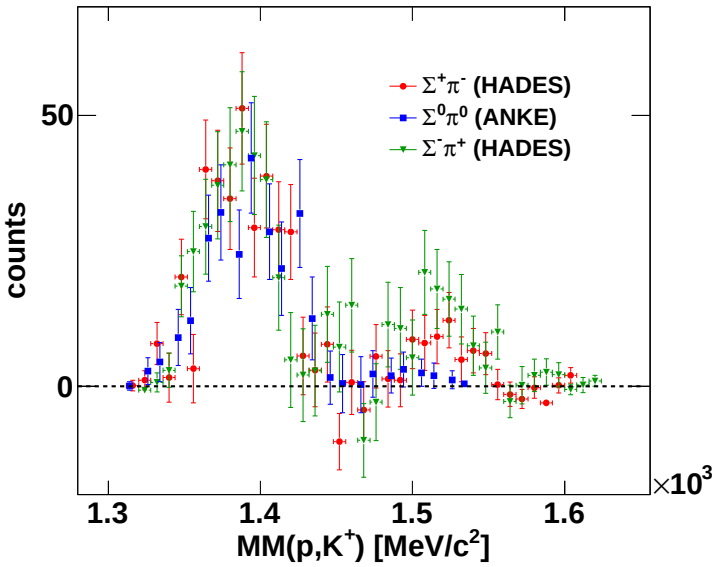

Figure 4.23: Missing mass (p,K^+) of all three decay channels. The $\Lambda(1405)$ in the neutral ($\Sigma^0\pi^0$) channel is taken from [Zyc08].

5 Investigation of the $\Sigma(1385)^+$ resonance

This chapter presents the analysis of the $\Sigma(1385)^+$, which is very similar to the analysis of the $\Lambda(1405)$, described in chapter 4. Although the data base of this resonance is already quite rich, the last high statistic measurement is, to our knowledge, more than 20 years ago. Thus new data, obtained with modern detectors and analysis methods, are required. Furthermore, its investigation can supply some important information concerning the $\Sigma(1385)^0$ resonance, which plays an important role in the $\Lambda(1405)$ analysis. It can for example deliver a reference for the cross section of the $\Sigma(1385)^0$. Also the line shapes of the two resonances should at least be similar, what can serve as a cross check for the $\Sigma(1385)^0$ reconstruction [Epp09].
The first part of this chapter focuses on general aspects, concerning the investigation of this resonance. Afterwards, the analysis itself is described, where finally a pure $\Sigma(1385)^+$ is obtained.

5.1 General aspects

As it was shown in the last chapter, the $\Sigma(1385)^+$ can be produced in proton-proton reactions with a kinetic beam energy of 3.5 GeV. The most dominant production mechanism together with the full decay chain is shown in the reactions (5.1)-(5.7).
The HADES spectrometer allows only to investigate channel (5.2) exclusively, which supplies the same final state products as the charged decay channels of the $\Lambda(1405)$ (p,K^+,π^+,π^-,n). Thus the $\Lambda(1405)$ together with the channels (4.14)-(4.19) are potential background sources for this analysis. Furthermore, the misidentification of protons and pions will again deliver additional background, which has to be handled. The main steps in the analysis of the $\Sigma(1385)^+$ are the following:

1. The appropriate set of hadrons (p,K^+,π^+,π^-) has to be identified.

2. With the obtained data set the intermediate Λ can be reconstructed via the invariant mass of the proton and the π^-, and by cutting on this resonance, the $\Sigma(1385)^+$ events are extracted.

3. The missing neutron is obtained by calculating the missing mass of the four charged particles for all remaining events. The selection of events within an appropriate neutron mass range increases the purity of the sample for further investigations.

4. The $\Sigma(1385)^+$ is finally reconstructed via the invariant mass of the Λ and the π^+.

With the cut on the intermediate Λ, the channels (4.2) and (4.4), as well as the channels (4.15)-(4.19) are highly suppressed. Thus their background contribution can be neglected in the final spectra. However, the non resonant reaction (4.14) has exactly the same decay characteristics and this background source together with the misidentification background will contaminate the $\Sigma(1385)^+$ signal.

$$p + p \xrightarrow{3.5GeV} \Sigma(1385)^+ + K^+ + n \tag{5.1}$$

$$\Sigma(1385)^+ \rightarrow \Lambda + \pi^+$$

$$\Lambda \rightarrow p + \pi^- \quad 56.33\% \tag{5.2}$$

$$\Lambda \rightarrow n + \pi^0 \quad 31.82\% \tag{5.3}$$

$$\Sigma(1385)^+ \rightarrow \Sigma^+ + \pi^0$$

$$\Sigma^+ \rightarrow p + \pi^0 \quad 3.06\% \tag{5.4}$$

$$\Sigma^+ \rightarrow n + \pi^+ \quad 2.87\% \tag{5.5}$$

$$\Sigma(1385)^+ \rightarrow \Sigma^0 + \pi^+$$

$$\Sigma^0 \rightarrow \Lambda + \gamma$$

$$\Lambda \rightarrow p + \pi^- \quad 3.79\% \tag{5.6}$$

$$\Lambda \rightarrow n + \pi^0 \quad 2.14\% \tag{5.7}$$

5.2 Analysis of the $\Sigma(1385)^+$

The first step in the analysis, the identification of one proton, one K^+, one π^+ and one π^-, is the same as in the $\Lambda(1405)$ analysis (see subsection 4.2.1). Thus besides the dE/dx cuts, kaons are additionally purified by a cut on the mass distribution. However, the Λ resonance in channel (5.2) allows the application of less strict cuts. As was shown in subsection 4.2.1, the cut on the Λ produces already a data sample with a rather high kaon purity (see figure 4.4) and consequently the $dE/dx - K^+$ cuts for the $\Sigma(1385)^+$ analysis are chosen to be slightly broader as for the $\Lambda(1405)$ analysis. Also the cut on the K^+ mass is widen up ($270\ \mathrm{MeV/c^2} < M(K^+) < 780\ \mathrm{MeV/c^2}$). In this way the amount of $\Sigma(1385)^+$ events in the obtained data sample is increased.
The Λ sample can be further selected by applying some cuts on the track topology [Sch08] [Epp09]. This is illustrated in figure 5.1.

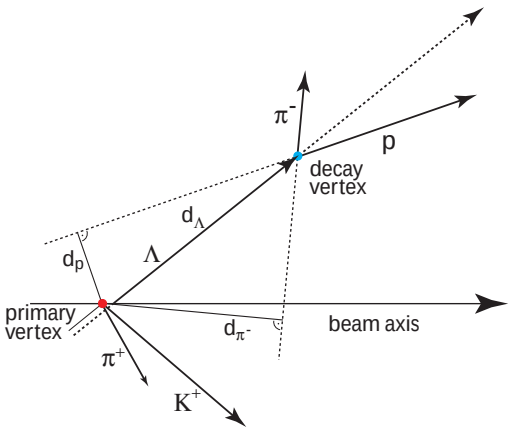

Figure 5.1: Schematic view of the Λ decay. The primary vertex (red point) is determined as the cross point of the π^+ track line and of the K^+ track line. The Λ decay vertex (blue point) is obtained by crossing the track lines of the proton and the π^-.

The Λ has a lifetime of $c\tau \approx 7.89$ cm [Gro08] and thus its decay vertex should have a certain minimum distance d_Λ to the primary vertex. The decay vertex is calculated as the cross point of the detected proton and π^- track, whereas the primary vertex is obtained from the intersection of the π^+ and the K^+ tracks. Since the $\Sigma(1385)^+$ decays almost immediately, the π^+ track can be used for the primary vertex reconstruction.
Additionally, the proton and the π^- track should have a certain minimum distance (d_p and d_{π^-}) from the primary vertex, as is depicted in figure 5.1. However, as the mass of the π^- is lower than the proton mass, momentum conservation requires that d_{π^-} is larger than d_p. The optimized cuts are summarized in table 5.1.

Cut on:	*Values*
Distance of decay vertex to primary vertex	$d_\Lambda > 15$ mm
Distance of proton track to primary vertex	$d_p > 0.0$ mm
Distance of π^- track to primary vertex	$d_{\pi^-} > d_p$

Table 5.1: Used cuts to reduce background for the $\Sigma(1385)^+$ analysis.

Their effect is presented in figure 5.2, where the intermediate Λ is reconstructed via the invariant mass of the proton and the π^-. In red is the result without the mentioned cuts, whereas the black distribution is obtained for all events, which fulfill table 5.1. In both cases a clear Λ signal is on top of a large amount of background. With the application of the track cuts, the background can be reduced by more than a factor of two whereas the signal yield is only decreased by 30%. Extracting events within a mass range from 1110 MeV/c^2 to 1120 MeV/c^2 (gray shaded area) further separates the $\Sigma(1385)^+$ events, and rejects the main part of the background.

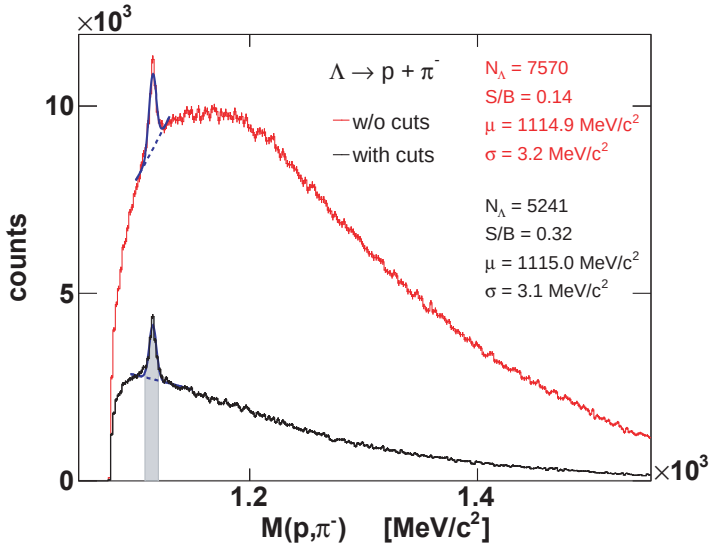

Figure 5.2: Invariant mass (p,π^-), showing a Λ. The distributions are fitted with a Gaussian together with a polynomial and a Landau-function (blue lines). Events in the mass range from 1110 MeV/c^2 – 1120 MeV/c^2 (1.6σ) are chosen for further investigations.

With the so obtained data sample the missing mass of all charged particles is investigated in figure 5.3 (black histogram).

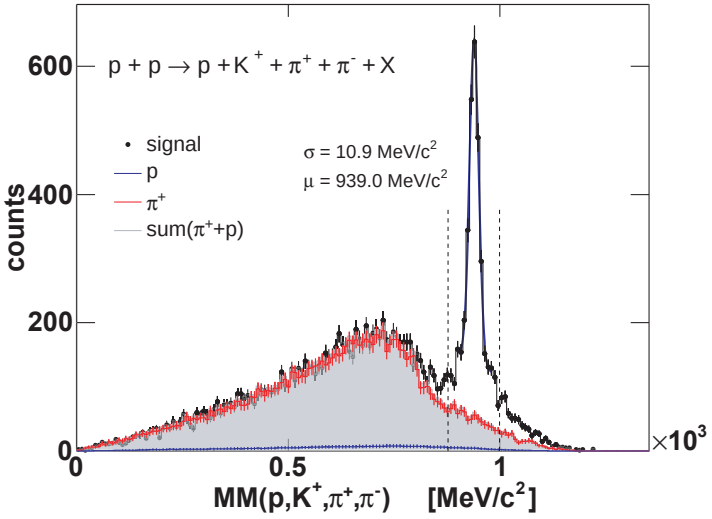

Figure 5.3: Missing mass (p,K^+,π^+,π^-), showing a neutron. The resonance is fitted with a Gaussian (blue line). The total misidentification background (gray distribution) is obtained with the sideband analysis, explained in section 4.3. Events in a 5.5σ mass range from 877 MeV/c^2 to 999 MeV/c^2 (vertical dashed lines) are used for the further analysis.

As the reactions (5.2) and (4.14) predict, a very clear neutron peak sticks out of a low amount of background. In subsection 4.2.1 it was shown that this background can only be due to misidentification of protons and pions as kaons. Therefore it can be described in exactly the same way as in figure 4.19, meaning that the same sideband analysis with the momentum dependent scaling factors is applied. The only difference is that the neutron is investigated after the cut on the invariant Λ.
The result of the sideband analysis is shown in the gray histogram in figure 5.3, which can describe the experimental spectrum quite well. The different contributions of misidentified pions and protons are illustrated in the red and blue distributions, respectively. Like in figure 4.19 the pions are dominating the misidentification background.
For the further investigations, only events within the mass area from 877 MeV/c^2 to 999 MeV/c^2 are used. Additionally, these events are refitted, with the constraint that the missing mass of all charged particles must be the neutron mass, which increases the mass resolution of the $\Sigma(1385)^+$.
The so obtained refitted proton and π^- track are used to calculate the track parameters of the Λ. Together with the refitted π^+ track, the $\Sigma(1385)^+$ can be reconstructed via the invariant mass (Λ,π^+), shown in figure 5.4. The picture provides already a very clear $\Sigma(1385)^+$ with a broad overlaid background distribution. This background is modeled in the gray histogram. It consists of a contribution due to misidentification (blue histogram) and additionally of a contribution due to the non resonant channel (4.14) (red dashed histogram), which is obtained with simulations. The determination of the strengths of these two background sources is done by fitting to the experimental data within a mass range from 1535 MeV/c^2 to 1645 MeV/c^2 (vertical dashed lines).

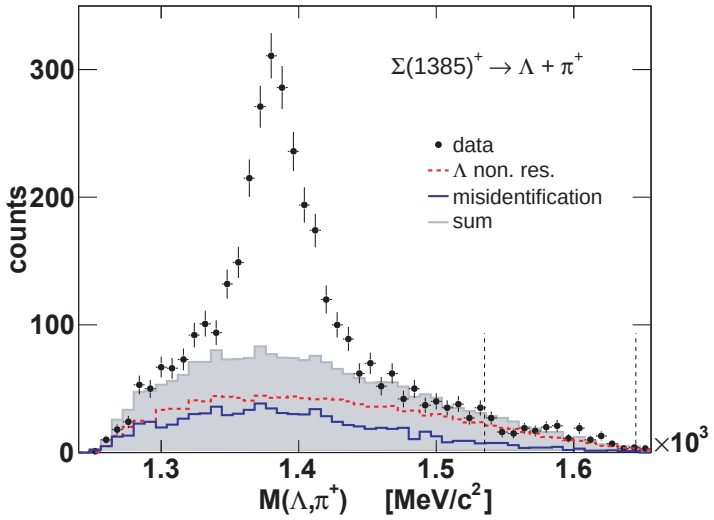

Figure 5.4: Invariant mass (Λ,π^+), showing a $\Sigma(1385)^+$. The different background contributions are scaled with fit factors and are added up to the gray histogram (see text). The scaling of the background is done within a mass range from 1535 MeV/c^2 to 1645 MeV/c^2 (vertical dashed lines).

For that purpose the scaling factor of the misidentification background is taken as fixed by the fit to figure 5.3 and thus only the strength of the non resonant contribution has to be adapted. In order to get the pure $\Sigma(1385)^+$ contribution, the gray histogram is subtracted from the experimental spectrum. The result is shown in figure 5.5, where a total yield of about 1500 $\Sigma(1385)^+$ is obtained.
As the $\Sigma(1385)^+$ is predicted to be a P_{13} state [Gro08], the obtained distribution is fitted with a $p-$wave relativistic Breit-Wigner function, which reads as follows [Agu81]:

$$f(M) = A\left(\frac{q}{q_0}\right)^2 \frac{M_0^2\Gamma_0^2}{\left(M^2 - M_0^2\right)^2 + M_0^2\Gamma^2} \tag{5.8}$$
$$\text{with } \Gamma = \Gamma_0\left(\frac{M_0}{M}\right)\left(\frac{q}{q_0}\right)^{2l+1}$$

A is an arbitrary scaling factor, M_0 is the pole mass and Γ_0 is the width of the resonance. The quantity q is the momentum of the two decay products (Λ and π^+) in the rest frame of a $\Sigma(1385)^+$ with a mass M. q_0 is the appropriate value for the pole mass M_0. The mass dependent width Γ respects the angular momentum of the resonance, thus l must be set equal to one for a $p-$wave.
The result of the fit, where A, M_0 and Γ_0 are the fit parameters, is shown in the top panel of figure 5.5. As a cross check, the resonance is additionally fitted with a $s-$wave relativistic Breit-Wigner (figure 5.5, bottom panel), which has the following form [Agu81]:

$$f(M) = A\frac{M_0^2\Gamma_0^2}{\left(M^2 - M_0^2\right)^2 + M_0^2\Gamma_0^2} \tag{5.9}$$

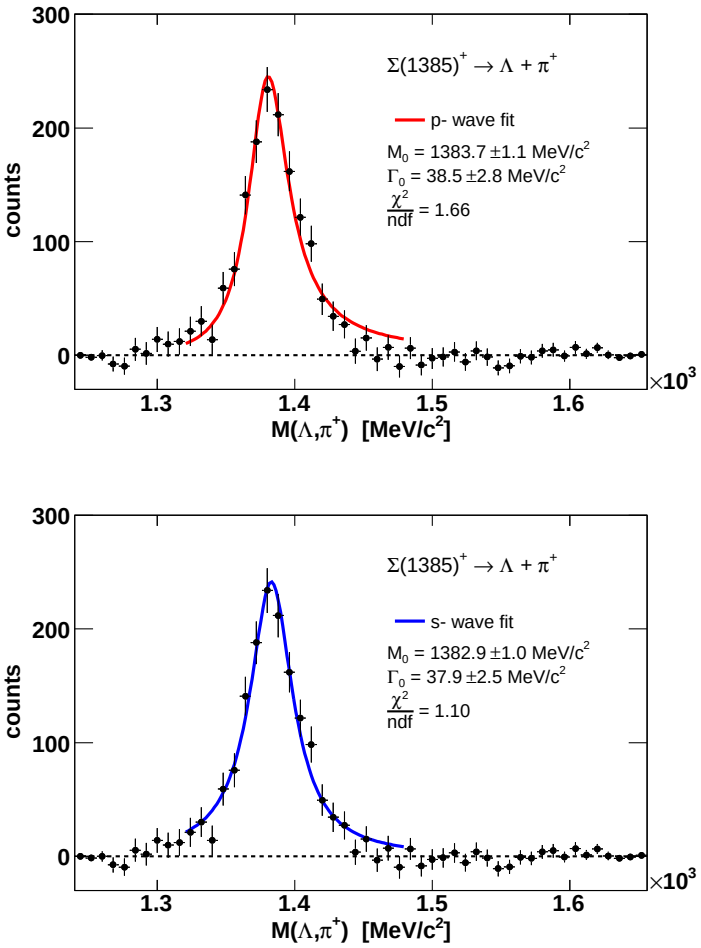

Figure 5.5: Invariant mass (Λ,π^+), showing a $\Sigma(1385)^+$, after the background subtraction. The solid lines illustrate the fit results of a $p-$wave relativistic Breit-Wigner function (top) and a $s-$wave relativistic Breit-Wigner function (bottom).

It is surprising that the $s-$wave fit works even better than the $p-$wave fit, confirmed by the normalized χ^2 values in figure 5.5. However, the differences in our fits are low and thus they are not sensitive enough to allow any quantitative statements.
Furthermore, the obtained values for M_0 and Γ_0 are in both cases compatible with the nominal values of $M_0 = 1282.8 \pm 0.4$ MeV/c^2 and $\Gamma_0 = 35.8 \pm 0.8$ MeV/c^2 [Gro08]. This is confirmed by a comparison to a couple of other experiments, which were evaluated for the determination of the nominal values [Gro08]. Figure 5.6 shows the obtained results of the $\Sigma(1385)^+$ reconstruction together with the spectra of [Bau84] and [Bor74]. All distributions are quite similar.
The good agreement with the other experimental results proofs that the background in figure 5.4 is modeled correctly. For final conclusions the spectrum in figure 5.5 has to be corrected for efficiency and acceptance, which was not done by now.
Finally one has to mention that the nominal values of the $\Sigma(1385)^+$ (see above) are extracted as an average of only a few experiments (see [Gro08]). However, the pole masses, which were obtained in these measurements, range from 1381.0$\pm$1.0 MeV/c^2 to 1384.5$\pm$0.5 MeV/c^2. Interesting is that some of these values were obtained with $s-$wave fits, since they

showed also better results than the $p-$wave fits [Agu81][Bau84]. Since the data base for the $\Sigma(1385)^+$ is not so extended, the new data, obtained with HADES, could at least serve as a cross check and will help to reduce the uncertainties concerning this resonance.

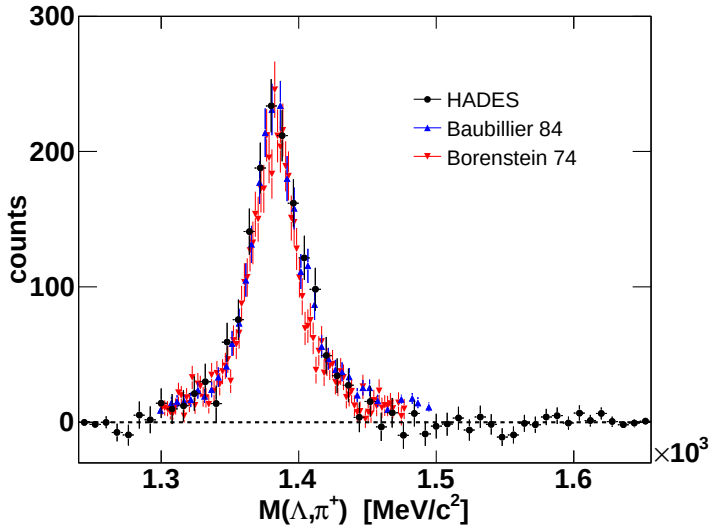

Figure 5.6: $\Sigma(1385)^+$ spectrum in HADES, obtained via the invariant mass (Λ,π^+). Compared to this are spectra from other experiments ([Bau84],[Bor74]).

For the future it is planed to determine the cross section of the $\Sigma(1385)^+$ by a comparison to elastic p+p reactions. This can be used as a reference for the determination of the $\Sigma(1385)^0$ cross section. The knowledge of this value is essential in order to keep the uncertainties in the subtraction of the $\Sigma(1385)^0$ from the $\Lambda(1405)$ resonance low (see chapter 4).

6 Conclusions and outlook

6.1 Conclusion

It was pointed out in the motivation that new data for the $\Lambda(1405)$ are needed. This thesis has shown the first measurement of the $\Lambda(1405)$ in $p+p$ reactions for the charged $\Sigma^{\pm}\pi^{\mp}$ decay channels. It was possible to extract a signal yield of around 330 entries for each channel.
An important step in the complicated analysis was the application of a kinematic refit, which helped to reduce the background essentially. Furthermore, it was shown that the development of a sophisticated sideband analysis is essential for the correct description of the background below the $\Lambda(1405)$ signal. In this way it was possible to subtract all background contributions and a pure $\Lambda(1405)$ signal in both channels could be obtained.
The $\Lambda(1405)$ in the three $(\Sigma\pi)^0$ decay channels shows no significant differences in the pole mass or in the line shape, respectively (see figure 4.23). This is an interesting point. In γ induced reactions, theory expects indeed a clear effect for the different decay channels, like it was shown in the motivation. This expectation was partially confirmed by the observations of the CLAS collaboration.
However, a theoretical prediction for proton-proton reactions is not yet available. These calculations are necessary in order to interpret the obtained results. Maybe the expected effects for the $\Lambda(1405)$ are different as in γ induced reactions. Furthermore, it will be interesting to see, if theory predicts the pole mass to be around 1385 MeV/c^2 instead of 1405 MeV/c^2, like it was observed in this thesis. This could be a hint for the $\Sigma\pi$ resonance being the dominant intermediate state of the $\Lambda(1405)$.
At this point one has to stress out that the obtained statistics for the two charged decay channels are not very high and leave probably room for diverse interpretations.
As was already mentioned, a critical point in the presented analysis is the subtraction of the $\Sigma(1385)^0$ background, since the relative cross section of the $\Lambda(1405)$ and $\Sigma(1385)^0$ is not known precisely. These cross sections can be extracted from the analysis of the neutral decay channels, where the $\Lambda(1405)$ and the $\Sigma(1385)^0$ can be separated exclusively. Channel (4.12) is already under investigation and here a $\Sigma(1385)^0$ yield of about 300 entries could be obtained [Epp10]. By doing simulations, one can estimate the total efficiency for the reconstruction to $1.169 \cdot 10^{-3}$. Consequently, about $300/1.169 \cdot 10^{-3} = 257000$ $\Sigma(1385)^0$ events in the decay chain (4.12) should have been produced. Weighting with the branching ratio for this channel (55.59%), this leads to totally $257000/0.5559 = 462000$ produced $\Sigma(1385)^0$. The obtained value can be used to calculate the expected yield of $\Sigma(1385)^0$ in e.g. the $\Sigma^-\pi^+$ channel, which contaminates the $\Lambda(1405)$ signal. About $462000 \cdot 0.0585 = 27000$ $\Sigma(1385)^0$ should decay into the $\Sigma^-\pi^+$ state (see reaction (4.7)). Simuluations gave a total reconstruction efficiency of $1.035 \cdot 10^{-3}$ for this channel. This should result in $27000 \cdot 1.035 \cdot 10^{-3} = 28$ $\Sigma(1385)^0$ events, contributing to the experimental signal in figure 4.21 (bottom panel). The fitting procedure, described in chapter 4, estimates the $\Sigma(1385)^0$ contribution in the $\Sigma^-\pi^+$ channel to 21 entries (figure 4.21, bottom panel, violet histogram). These rough estimations proof that the obtained $\Lambda(1405)$ signal is really

$\Lambda(1405)$ and that the yield of subtracted $\Sigma(1385)^0$ is more or less correct.
However, in order to be absolutely sure that the $\Sigma(1385)^0$ is subtracted correctly, more systematic studies have to be carried out. Finally the obtained $\Lambda(1405)$ spectra have to be corrected for efficiency and acceptance and systematic errors have to be determined. Although these corrections were not done by now, we know already from simulations that they will not influence the position of the pole mass distinctly.

6.2 Inclusion of the Forward Wall data

The analysis of the $\Lambda(1405)$ with HADES is hampered by low statistics. Due to the kinematics, most of the particles, produced in the reaction (4.1), are boosted in the forward direction with polar angles lower than 15°. However, it was pointed out in chapter 2 that during the $p+p$ beam time the FW was included in HADES. This FW increases the acceptance for polar angles from 0.33° to 7°. Unfortunately the FW does not provide the possibility of particle identification, which makes its inclusion for the analysis rather challenging. As it covers polar angles below the original HADES acceptance, particles in the FW do not pass the MDC detectors and thus their trajectories can not be reconstructed with the tracking algorithm. Consequently it is impossible to determine the momentum of these particles independently. Therefore these data can only be investigated by doing a hypothesis for the particle, hitting the FW.
Considering the reactions (4.2) and (4.4), one can identify the K^+, the π^+ and the π^- in the original HADES acceptance. If additionally a particle hits the FW, one can assume that it is a proton. This choice is reasonable, since the proton has the highest mass of the four final state products and is thus preferably boosted in the forward direction. The feasibility of this hypothesis was tested with the simulation of table 4.1. If the three particles in HADES are identified correctly, 89.2% of the particles in the FW are indeed protons, 8.1% are π^+ and only 2.7% are π^-. Therefore the additional background due to misidentified particles in the FW will be low.
As the FW provides a measured time signal for the incoming particle as well as a hit position, the three momentum $\vec{p}$ of this particle can be determined with help of the mentioned hypothesis. The magnitude of the momentum reads as follows:

$$p = m\frac{\frac{s}{t}}{\sqrt{1-\frac{s^2}{t^2c^2}}} \tag{6.1}$$

m is the nominal mass of the assumed particle (here this is the proton). The time-of-flight t can be calculated with the reconstructed start time (see chapter 2) and the path length s is directly accessible with the known distance of the FW to the target. The momentum resolution depends on the time resolution of the FW via Gaussian error propagation:

$$\Delta p = \left|\frac{\partial p}{\partial t}\right| \Delta t \;\Rightarrow \tag{6.2}$$

$$\Delta p = \left|\frac{-m\frac{s}{t^2}}{\left(1-\frac{s^2}{c^2t^2}\right)^{3/2}}\right| \Delta t \;\Rightarrow \tag{6.3}$$

$$\frac{\Delta p}{p} = \frac{\frac{1}{t}}{1-\frac{s^2}{c^2t^2}}\Delta t \tag{6.4}$$

with the following quantities:

$$\begin{aligned} c &= 3 \cdot 10^8 \frac{m}{s} \\ s &\approx 7m \\ \Delta t &\approx 700ps \\ m_p &= 938.3MeV/c^2 \end{aligned}$$

The resolution depends on the time-of-flight t, which itself depends on the momentum of the particle. For an estimation of the momentum resolution, the momentum is set to 1.77 GeV/c. This is the average value of protons in the FW, produced in $p+p$ reactions at 3.5 GeV [Epp09]. With this the appropriate time-of-flight t is:

$$t = \sqrt{\frac{m^2}{p^2} + \frac{1}{c^2}} s \approx 26.4ns \tag{6.5}$$

The average of the momentum resolution is then 12%. This, however, is calculated under the assumption of a infinite start time resolution. Therefore the momentum resolution of the FW will be even worse, especially as a start detector was missing during the beam time.
An undesired consequence of the poor momentum resolution is that also the mass resolution of the $\Lambda(1405)$ will in general be quite poor. However, it is possible to use the kinematic refit for the reactions (4.2) and (4.4), which can improve the mass resolution, as it is described in chapter 3. In order to test this for the FW, the reaction (4.4) was simulated with PLUTO. The black histogram in figure 6.1 is the missing mass (p,K^+) distribution, showing the $\Lambda(1405)$, for the K^+, the π^+ and the π^- being in HADES (polar angle $\vartheta > 18°$) and the proton hitting the FW ($\vartheta < 7°$).

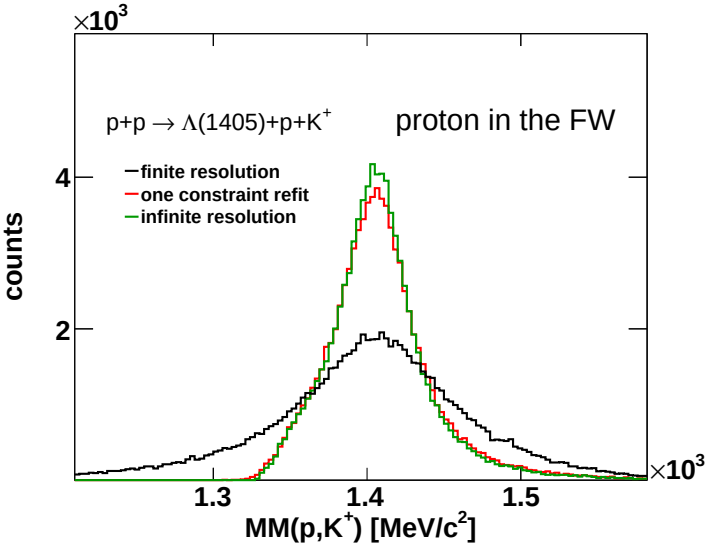

Figure 6.1: Simulated missing mass (p,K^+) distribution, showing the $\Lambda(1405)$. The K^+, the π^+ and the π^- of reaction (4.4) are within the HADES acceptance, the proton is in the FW (see text).

The momentum resolution of the proton was simulated to 12%, whereas the momentum resolution of the other particles was set to 2.5%. The resolution for ϑ and φ was chosen to 0.05° for all particles. It is clear that the line shape of the $\Lambda(1405)$ is totally distorted in the black histogram. As the exact measurement of the line shape is of interest, the analysis of the FW data would thus be useless. Fortunately, applying the refit, with the constraint on the neutron mass, results in the red histogram, which is quite comparable to the original line shape of the $\Lambda(1405)$ (green histogram). Only with this essential improvement in the mass resolution, the $\Lambda(1405)$ line shapes of the FW can finally be added to the line shapes, obtained in chapter 4. In [Epp09] it was shown that in doing this the statistics of the $\Lambda(1405)$ can be increased by another 65% for the two charged channels.
Of course also the signal yield of the $\Sigma(1385)^+$ could be further increased by including the FW data.

6.3 Future strangeness projects with HADES

The HADES experiment is at the moment undergoing a major upgrade:

- In chapter 2 it was already mentioned that since 2009 HADES is equipped with RPCs, replacing the TOFino detector. The much better time resolution of the RPCs will improve the particle identification essentially.
- The data acquisition (DAQ) is upgraded for a $Au + Au$ beam time, planned for autumn 2010. With this, the data taking rate will be increased, which results in better statistics for future analysis.
- It is planned to replace the PreSHOWER detector by a calorimeter for the γ identification. This opens the door for the reconstruction of new particles with HADES, like the π^0, decaying into two γ's.

In the future, pion beams will be employed for measurements with the HADES spectrometer. π^- beams are planned with a kinetic energy varying from 1.2 to 1.64 GeV hitting LH_2 and solid targets. The $\Lambda(1405)$ is then mainly produced together with a K^0 ($\pi^- p \rightarrow \Lambda(1405)K^0$), where the threshold energy of the pion is about 1.32 GeV. Due to the low beam energy, the particles are less boosted in the forward direction, compared to the $p + p$ reactions. This results in a higher acceptance for $\Lambda(1405)$ events. Additionally, the calorimeter will provide the possibility to investigate a new decay channel (see reaction (4.6)) and will allow to reconstruct the $\Lambda(1405)$ via the invariant mass technique (see reactions (4.3) and (4.5)). Altogether the hunt for the $\Lambda(1405)$ will go on and HADES will supply an important contribution to a deeper understanding of this strange resonance.

Bibliography

[Aga07] G. Agakichiev et al.
Dielectron production in C-12 + C-12 collisions at 2-AGeV with HADES.
Phys. Rev. Lett., 98:052302, 2007.

[Aga09a] G. Agakishiev et al.
Deep sub-threshold Ξ^- production in Ar+KCl reactions at 1.76 A GeV.
Phys. Rev. Lett., 103:132301, 2009.

[Aga09b] G. Agakishiev et al.
ϕ decay: a relevant source for K^- production at SIS energies?
Phys. Rev., C80:025209, 2009.

[Aga09c] G. Agakishiev et al.
The High-Acceptance Dielectron Spectrometer HADES.
Eur. Phys. J., A41:243–277, 2009.

[Agn05] M. Agnello et al.
Evidence for a kaon-bound state K^-pp produced in K^- absorption reactions at rest.
Phys. Rev. Lett., 94:212303, 2005.

[Agu81] M. Aguilar-Benitez and J. Salicio.
A new experimental determination of the resonance parameters of the $\Sigma^+(1385)$, $\Sigma^0(1385)$ and $\Sigma^-(1385)$ hyperons.
Anales de Fisica Serie A, 77:144–151, 1981.

[Ahn03] J. K. Ahn.
$\Lambda(1405)$ photoproduction at SPring-8/LEPS.
Nucl. Phys., A721:715–718, 2003.

[Aka02] Y. Akaishi and T. Yamazaki.
Nuclear $\bar{K}$ bound states in light nuclei.
Phys. Rev., C65:044005, 2002.

[Als61] M. H. Alston et al.
Study of resonances of the $\Sigma - \pi$ system.
Phys. Rev. Lett., 6:698–702, 1961.

[Ave98] P. Avery.
http://www.phys.ufl.edu/~avery/fitting.html.
1998.

[Bau84] M. Baubillier et al.
The reactions $K^-p \to \pi^{\mp}\Sigma(1385)^{\pm}$ at 8.25 GeV.
Z. Phys., C23:213, 1984.

[Bet53] H. A. Bethe and J. Ashkin.
Experimental Nuclear Physics, 1:253, 1953.

[Bor74] S. R. Borenstein, G. R. Kalbfleisch, R. C. Strand, V. Vanderburg and J. W. Chapman .
A determination of the mass, width and the ($\Sigma\pi/\Lambda\pi$) branching ratio of the $\Sigma(1381)$ baryon.
Phys. Rev., D9:3006, 1974.

[Bor05] B. Borasoy, R. Nissler and W. Weise.
Chiral dynamics of kaon nucleon interactions, revisited.
Eur. Phys. J., A25:79–96, 2005.

[Car05] M. Cargnelli et al.
Kaonic hydrogen measurement with DEAR at DAPHNE.
Int. J. Mod. Phys., A20:341–348, 2005.

[Dal61] R. H. Dalitz and S. F. Tuan.
The phenomenological representation of $\bar{K}$-nucleon scattering and reaction amplitudes.
Annals Phys., 3:307–351, 1961.

[Des54] S. Deser, M. L. Goldberger, K. Baumann and W. Thirring.
Energy level displacements in π mesonic atoms.
Phys. Rev., 96:774–776, 1954.

[Ebe59] P. Eberhard, A. H. Rosenfeld, F. T. Solmitz, , R. D. Tripp and M. B. Watson.
K^--hydrogen charge-exchange scattering.
Phys. Rev. Lett., 2:312–313, 1959.

[Epp09] E. Epple.
The $\Lambda(1405)$- resonance measured via its decay into $\Sigma^0\pi^0$ in proton proton collisions with the HADES spectrometer.
Master's thesis, Technische Universität München, 2009.

[Epp10] E. Epple.
Private communication.
2010.

[Eva83] D. Evans et al.
Charge exchange scattering in K^-p interactions below 300 MeV/c.
J. Phys., G9:885–894, 1983.

[Fab03] L. Fabbietti.
Study of e^+e^- pair acceptance in the dilepton spectrometer HADES.
PhD thesis, Technische Universität München, 2003.

[Frü00] R. Frühwirth, M. Regler, R. K. Bock, H. Grote, D. Notz.
Data Analysis Techniques for High-Energy Physics.
Cambridge University Press, 2000.

[Frö09] I. Fröhlich et al.
Design of the Pluto Event Generator.
arXiv:nucl-ex/0905.2568, 2009.

[Gea95] Geant.
http://www.asdoc.web.cern.ch/wwwasdoc/geant_html3/geantall.html.
1995.

[Gil07] A. Gil et al.
Front-end electronics development for the new resistive plate chamber detector of HADES.
JINST 2:T11001, 2007.

[Gro08] Particle Data Group.
Particle Physics Booklet.
Elsevier, 2008.

[Hem85] R. J. Hemingway.
Production of $\Lambda(1405)$ in K^- p reactions at 4.2 GeV/c.
Nucl. Phys., B253:742, 1985.

[HGe08] HGeant.
http://www-hades.gsi.de.
2008.

[Hum62] W. E. Humphrey and R. R. Ross Ronald.
Low-energy interactions of K^- mesons in hydrogen.
Phys. Rev., 127:1305–1323, 1962.

[Hyo03] T. Hyodo, A. Hosaka, E. Oset, A. Ramos and M. J. Vicente Vacas.
$\Lambda(1405)$ production in the $\pi^- p \to K^0 \pi \Sigma$ reaction.
Phys. Rev., C68:065203, 2003.

[Hyo08] T. Hyodo and W. Weise.
Effective $\bar{K}N$ interaction based on chiral SU(3) dynamics.
Phys. Rev., C77:035204, 2008.

[Jid03] D. Jido, J. A. Oller, E. Oset, A. Ramos and U. G. Meissner.
Chiral dynamics of the two $\Lambda(1405)$ states.
Nucl. Phys., A725:181–200, 2003.

[Kit66] W. Kittel, G. Otter and I. Wacek.
The $K^- p$ charge exchange interactions at low energies and scattering lengths determination.
Phys. Lett., 21:349, 1966.

[Lap09] K. Lapidus et al.
Dielectron production in pp and dp collisions at 1.25 GeV/u with HADES.
arXiv:nucl-ex/0904.1128, 2009.

[Lut92] M. Lutz, S. Klimt and W. Weise.
Meson properties at finite temperature and baryon density.
Nucl. Phys., A542:521–558, 1992.

[Lut05] M. F. M. Lutz and M. Soyeur .
The associated photoproduction of positive kaons and $\pi^0 \Lambda$ or $\pi \Sigma$ pairs in the region of the $\Sigma(1385)$ and $\Lambda(1405)$ resonances.
Nucl. Phys., A748:499–512, 2005.

[Mag05] V. K. Magas, E. Oset and A. Ramos.
Evidence for the two pole structure of the $\Lambda(1405)$ resonance.
Phys. Rev. Lett., 95:052301, 2005.

[Mag09] M. Maggiora et al.
DISTO data on Kpp.

arXiv:hep-ex/0912.5116, 2009.

[Mar05] J. Markert.
Untersuchung zum Ansprechverhalten der Vieldraht-Driftkammern niedriger Massenbelegung des HADES Experiments.
PhD thesis, Johann Wolfgang Goethe Universität, 2005.

[Mar10] J. Markert.
Private communication.
2010.

[Mor10] K. Moriya and R. Schumacher.
Properties of the $\Lambda(1405)$ measured at CLAS.
Nucl. Phys., A835:325–328, 2010.

[Nac99] J. C. Nacher, E. Oset, H. Toki and A. Ramos.
Photoproduction of the $\Lambda(1405)$ on the proton and nuclei.
Phys. Lett., B455:55–61, 1999.

[Nii08] M. Niiyama et al.
Photoproduction of $\Lambda(1405)$ and $\Sigma^0(1385)$ on the proton at $E_\gamma = 1.5 - 2.4$ GeV.
Phys. Rev., C78:035202, 2008.

[Oll01] J. A. Oller and U. G. Meissner .
Chiral dynamics in the presence of bound states: Kaon nucleon interactions revisited.
Phys. Lett., B500:263–272, 2001.

[Ose98] E. Oset and A. Ramos.
Non perturbative chiral approach to s-wave $\bar{K}N$ interactions.
Nucl. Phys., A635:99–120, 1998.

[Ose07] E. Oset, L. S. Geng and M. Döring.
The nature of the $\Lambda(1405)$.
arXiv:nucl-th/0710.5925, 2007.

[Pra04] S. Prakhov et al.
$K^- p \to \pi^0\pi^0\Sigma^0$ at $p(K^-) = 514$ MeV/c to 750 MeV/c and comparison with other $\pi^0\pi^0$ production.
Phys. Rev., C70:034605, 2004.

[Pre09] A. Prehn.
http://www.hades-wiki.gsi.de/cgi-bin/view/simana/energylosscalibration.
2009.

[Rus06] A. Rustamov.
Exclusive η meson reconstruction in proton-proton collisions at 2.2 *GeV with the HADES spectrometer and high resolution tracking.*
PhD thesis, Technische Universität Darmstadt, 2006.

[Sch08] A. Schmah.
Produktion von Seltsamkeit in Ar+KCl Reaktionen bei 1.756 *AGeV mit HADES.*
PhD thesis, Technische Universität Darmstadt, 2008.

[Sch09] A. Schmah.
Private communication.
2009.

[Sha94] C. M. Shakin and W.-D. Sun.
Properties of the rho meson in nuclear matter.
Phys. Rev., C49:1185–1189, 1994.

[Tei09] K. Teilab.
Private communication.
2009.

[Tho73] D. W. Thomas, A. Engler, H. E. Fisk and R. W. Kraemer.
Strange particle production from π^- p interactions at 1.69 GeV/c.
Nucl. Phys., B56:15–45, 1973.

[Yam07] T. Yamazaki and Y. Akaishi.
The basic $\bar{K}$ nuclear cluster K^-pp and its enhanced formation in the $p + p \to K^+ + X$ reaction.
Phys. Rev., C76:045201, 2007.

[Zyc08] I. Zychor et al.
Shape of the $\Lambda(1405)$ hyperon measured through its $\Sigma^0\pi^0$ decay.
Phys. Lett., B660:167–171, 2008.

Danke

Zunächst möchte ich mich bei der ganzen Gruppe für die entspannte und freundschaftliche Atmosphäre bedanken. Dafür, dass sie mir immer mit Rat und Tat zur Seite standen, egal ob es um physikalische Probleme oder unendlich nervige Computerprobleme ging, bedanke ich mich bei Eliane Epple, Martin Berger, Robert Münzer, Matthias Danner und Michael Weber.
Besonderer Dank gilt Dr. Alexander Schmah. Bei Dir habe ich endlich gelernt, wie man sich angemessen über die alltäglichen Probleme beschwert, obwohl ich das wohl noch üben muss, damit ich Dir gerecht werde. Du warst aber auch immer bereit Dir Zeit für mich zu nehmen, über Probleme nachzudenken und Lösungen auszuarbeiten. Dabei habe ich wirklich eine ganze Menge gelernt. Man muss als Diplomand schon sehr viel Glück haben, einen so tollen Betreuer zu haben. Vielen Dank!
Ganz besonders möchte ich mich bei Prof. Dr. Laura Fabbietti bedanken. Du hast mich in diese tolle Gruppe geholt. Deinen unermüdlicher Ehrgeiz, jeden von uns zu fördern und zu fordern, weiß ich sehr zu schätzen. Das ist zwar manchmal auch sehr anstrengend und mit viel Arbeit verbunden, doch bin ich mir sicher, dass es sich für mich lohnen wird und meinem weiteren physikalischen Werdegang sehr zu Gute kommt. Vielen Dank für diese tolle Unterstützung! Ich habe sehr viel bei Dir gelernt!
Mein größter Dank gilt meinen Eltern, Michael und Christiane, meiner Schwester, Juliane und meiner Freundin, Andrea. Ihr habt mich mein ganzes Leben lang in allen meinen Interessen, ob sie sinnvoll waren oder nicht, voll unterstützt und alles dafür getan, dass ich sie ausüben konnte. Schon als ich noch ein kleines Kind war haben wir uns oft über das Universum und seinen Ursprung unterhalten. Das hat sich so bei mir festgesetzt, dass ich letztendlich Physik studiert habe, was bestimmt die beste Entscheidung war. Ich weiß auch, dass ohne Euch diese Diplomarbeit nicht möglich gewesen wäre. Obwohl ich Euch das sicher nicht sehr oft zeige, bin ich dafür wirklich sehr dankbar und bin froh, eine so tolle Familie zu haben (damit meine ich natürlich auch Dich, Andrea).